Title
Synthesizing Smart Polymeric and Composite Materials

Permalink
https://escholarship.org/uc/item/2qj0h0wx

Author
GONG, CHAOKUN

Publication Date
2013

Peer reviewed|Thesis/dissertation

UNIVERSITY OF CALIFORNIA

Los Angeles

Synthesizing Smart Polymeric and Composite Materials

A dissertation submitted in partial satisfaction

of the requirements for the degree Doctor of Philosophy

in Materials Science and Engineering

by

Chaokun Gong

2013

ABSTRACT OF THE DISSERTATION

Synthesizing Smart Polymeric and Composite Materials

By

Chaokun Gong

Doctor of Philosophy in Materials Science and Engineering

University of California, Los Angeles, 2013

Professor Qibing Pei, Chair

Smart materials have been widely investigated to explore new functionalities unavailable to traditional materials or to mimic the multifunctionality of biological systems. Synthetic polymers are particularly attractive as they already possess some of the attributes required for smart materials, and there are vast room to further enhance the existing properties or impart new properties by polymer synthesis or composite formulation. In this work, three types of smart polymer and composites have been investigated with important new applications: (1) healable polymer composites for structural application and healable composite conductor for electronic device application; (2) conducting polymer polypyrrole actuator for implantable medical device application; and (3) ferroelectric

polymer and ceramic nanoparticles composites for electrocaloric effect based solid state refrigeration application. These application entail highly challenging materials innovation, and my work has led to significant progress in all three areas.

For the healable polymer composites, well known intrinsically healable polymer 2MEP4F (a diels-alder crosslinked polymer formed from a monomer with four furan groups and another monomer with two maleimide groups) was first chosen as the matrix reinforced with fiber. Glass fibers were successfully functionalized with maleimide functional groups on their surface. Composites from functionalized glass fibers and 2MEP4F healable polymer were made to compare with composites made from commercial carbon fibers and 2MEP4F polymer. Dramatically improved short beam shear strength was obtained from composite of functionalized glass fibers and 2MEP4F polymer.

The high cost of 2MEP4F polymer can potentially limit the large-scale application of the developed healable composite, we further developed a new healable polymer with much lower cost. This new polymer was formed through the Diels-Alder crosslinking of poly(furfuryl alcohol) (PFA) and 1,1'-(Methylenedi-4,1-phenylene)bismaleimide (MDPB). It showed the same healing ability as 2MEP4F while all starting materials are cheaper and commercially available. To further improve the mechanical strength of the PFA-MDPB healable polymer, epoxy as a strengthening component was mixed with PFA-MDPB healable polymer. The PFA, MDPB and epoxy composite polymers were further reinforced by carbon fiber as done with 2MEP4F matrix and the final composites were proved to have higher short beam shear strength than 2MEP4F while exhibiting a similar healing efficiency.

Healable polymer MDPB (a two maleimide groups monomer) – FGEEDR (a four furan groups monomer) was also designed and synthesized for transparent healable polymer. The MDPB-FGEEDR healable polymer was composited with silver nanowires (AgNWs) to afford healable transparent composite conductor. Razer blade cuts in the composite conductor could heal upon heating to recover the mechanical strength and electrical conductivity of the composite. The healing could be repeated for multiple times on the same cut location. The healing process was as fast as 3 minutes for conductivity to recover 97% of the original value.

For electroactive polymer polypyrrole, the fast volume change upon electrical field change due to electrochemical oxidization or reduction was studied for actuation targeting toward a robotic application. The flexibility of polypyrrole was improved via copolymerization with pyrrole derivatives. Actuator devices are fabricated that more suitable for implantable medical device application than pyrrole homopolymer.

The change of dipole re-orientation and thus dielectric constant of ferroelectric polymers and ceramics upon electrical field may be exploited for electrocaloric effect (ECE) and solid state refrigeration. For ferroelectric ceramics, we synthesized a series of $Ba_{1-x}Sr_xTiO_3$ nanoparticles with diameter ranging from 8-12 nm and characterized their dielectric and ferroelectric properties through hysteresis measurement. It was found that 8 nm $BaTiO_3$ nanocrystals are stable at cubic crystal structure without ferroelectric character. $Ba_{1-x}Sr_xTiO_3$ nanoparticles with larger crystalline size (40nm) provide near room temperature transition temperature which could be the Curie temperature. We carefully studied the electrocaloric effect of ferroelectric polymers P(VDF-TrFE) and P(VDF-TrFE-CFE). The nanocomposite of $Ba_{1-x}Sr_xTiO_3$ nanoparticles dispersed in

P(VDF-TrFE-CFE) was fabricated and studied by hysteresis measurement to estimate the electrocaloric effect of the composite. The interdigitated electrode samples were successfully infiltrated with terpolymer and the multilayers ECE device showed 0.01 C/m^2 displacement at 70MV/m. Free-standing monolayer ECE devices made from the terpolymer gave 3.4^{0}C temperature change measured via an infrared camera.

The dissertation of Chaokun Gong is approved.

_____

Yang Yang

_____

Yunfeng Lu

_____

Yu Huang

_____

Qibing Pei, Committee Chair

University of California, Los Angeles

2013

Table of Contents

CHAPTER ONE

CHAPTER TWO

Development of healable polymer / functionalized glass fiber composite material as aerospace structural materials

CHAPTER THREE

Development of Healable Composite Formulated Using Commercially Available Poly Furfuryl Alcohol and Bismaleimide

CHAPTER FOUR

A Healable, Semi-transparent Silver Nanowire-Polymer Composite Conductor

List of Figures

Acknowledgements

First of all, I would like to thank my advisor Prof. Qibing Pei for the support and guidance provided throughout my PhD study at UCLA. You have advised me on not just the technical developments and approaches, but also the methodology, presentation, and insight needed to do research. And of course, the financial support too.

Also, I would like to thank the other members of my committee, Professor Yu Huang, Professor Yang Yang and Professor Yufeng Lu for their help. I have taken classes under all of you and I learned much, especially on looking at the area of materials science at a wider angle than what I would originally do.

I would also thank Professor Thomas Hahn from Mechanical Engineering Department, UCLA. Thank you for providing collaboration project "carbon fiber self-healing polymer composite development" to me and also for the financial support from you. Thank you for opening the field of healable materials to me.

I would also thank Professor Y. Sungtaek Ju from Mechanical Engineering Department, UCLA. Thank you for providing collaboration project "ferroelectric materials in electrocaloric effect based solid state refrigeration application" to me. I enjoyed this project very much.

Beyond the academic field, I would like to thank Pavad Medical Inc. who provided me an internship opportunity during my PhD study. The internship gave me different experience compared to life in school and helped me broaden my views too.

Next, I would like to thank my labmates who helped me a lot throughout my PhD study. They are Dr. Dongjuan Xi, Dr. Wei Yuan, Dr. Zhibin Yu, Dr. Jun Liu, Dr. Matthew Franzman, Dr. Jiajie Liang, Dr. Qi Chen, Dr. Xinguo Yang, Han Zhang, Tuling Lam, Xiaofan Niu, Wei Hu, Zhi Ren and Chao Liu. All the discussions we have are thought-provoking. All the friendships we have are my biggest wealth. Then, I would also like to thank all other students and visitors in our group. Thank you for all the helps!

Last and the mostly importantly, I would also like to thank to my loving Family:

I would love to thank my parents Naibin Gong and Zhenrong Liu for their selfless support over the past years. As a mom now, I deeply understand them and deeply appreciate all their love to me since I was a baby. Without you, I won't insist on this path and won't be able to have such an exciting and happy moment. I would like to thank my elder brother Dr. Guanyu Gong for all the support you give to me as well.

I would love to thank my parents-in-Law, Dr. Jiazhen Pan and Liudi Shen, without your help of taking care my 5 months baby, I have no chance to return back to school and claim my PhD today.

I would love to thank to my husband Dr. Guoqiang Pan for all the supporting and love you gave to me. Without you, I may quit my PhD during the way.

My dear Rosie, Mom Thank You for the most beautiful life you bring to me! Mom is so brave because I love you!

Deep thanks and love are little present on a paper, but always numerous born in mind!

Vita

2002-2006	B.S, Polymer Science
	B.S, English Language
	Qingdao University of Science and Technology
2006-2008	Masters, Materials Science and Engineering
	University of California, Los Angeles

Publications and Presentations

Chaokun Gong, Jiajie Liang, Wei Hu, Xiaofan Niu, Sungwon Ma, H. Thomas Hahn and Qibing Pei, "A Healable, Semi-transparent Silver Nanowire-Polymer Composite Conductor", Advanced Materials, Accepted, manuscript adma.201301069

Sungwon Ma, **Chaokun Gong**, Brian. Hanos, Thomas Darlington, Qibing. Pei, and Thomas. Hahn, "Development of A Thermally-Remendable Composite Using Poly Furfuryl Alcohol and Bismaleimide", Composites Science and Technology, Manuscript under review

Jun Liu, Lu Li, **Chaokun Gong**, Zhibin Yu and Qibing Pei, "An ambipolar poly (meta phenylene) copolymer with high triplet energy to host blue and green electrophosphorescence", J. Mater. Chem., 2011, 21, 9772-9777

Chaokun Gong, Qibing Pei, Hongpeng Wang, Nikhil D. Bhat, "Pyrrole copolymer with improved actuation performance", Presentation, SPIE–EAPAD conference, Sping 2009, San Diego

CHAPTER ONE

Introduction

1.1 Introduction to Smart Materials

Smart materials generally are designed materials that can change their properties or performance according to the environment stimulus.[1-3] Such materials can be sensitive to several environmental factors, such as temperature, pressure, pH, the intensity of exposure light or an electrical and magnetic field. Up to the external stimulus, the smart materials will have various response way, like altering color, changing conductivity, increasing dielectric constant and self-healing.[4, 5] Usually for smarting materials, slight changes in the environment are sufficient to induce great change in the materials' properties. Because smart materials usually can provide unique properties which won't be see in traditional materials and also usually can have multifunctionality as biological system, they have attracts great investigation for various advanced applications which is our focus in this dissertation.

For smart materials, there are various examples which can be classified by their properties. Piezoelectric materials are polymers or ceramics which can produce a voltage when external stress applied. They nowadays are widely used for sensor applications.[6-9] Oppositely, electroactive polymers which have large volume change or deformation upon the applied electrical field change are very promising for actuator applications. [10-22] Shape memory alloys or shape memory polymers can have large deformation induced by temperature change but then recovered back to the original shape when the temperature

change removed.[23-26] While for healable polymers, they can repaired their damage back to normal usage and then expand the material's lifetime upon heating or even atomically.[27-30] Lastly, dielectric or ferroelectric polymers and ceramics which have obvious dipole movements upon electrical field changes can provide dielectric constant change to fulfill various applications requirements.[31-32] From the materials classification point of view, all materials metal, ceramic, polymers and composite can be smart materials. In real word, most amount of smart materials are polymers and composites with more structure tuning ability will be reviewed in details next.

1.2 Development of Smart Polymers

Polymer as a high-molecular-weight organic compound is composed by repeated small unit called as monomer. It has attracted people for development and usage for several centuries. Initially, people found natural polymers which are derived from plants and animals and have been used for many centuries. These materials include wood, wool, leather, cotton, rubber and silk. Those natural materials were widely used all the time along with the civilization history and technology revolution till now. However, the inherent structure and corresponding property limits their wide applications in modern industry. Since the 19th century, people began to use chemistry method to modify natural polymers. The milestone examples for natural polymers modification include the synthesis of nitrocellulose through reaction of nitric acid and cellulose and the formation of vulcanized rubber by heating natural rubber under sulfur environment. Those modified natural polymers are still commercially widely used even in nowadays. However, the small groups of modified natural polymers still are insufficient comparing to the demands. With the development of scientific research from 20 century, people began to try to

synthesis numerous polymers from small organic molecules, with desired molecular structure to overcome the drawbacks in those natural polymers. Since then, the field of materials science has encountered a virtual revolution by the advent of synthetic polymers. Most of our useful plastics, rubbers and fiber materials now are synthetic polymers. The synthetics can be produced inexpensively, and their properties can be tuned as we wished to overcome the drawbacks of natural polymers. In some applications metal and wood parts have been replaced by plastics, which have satisfactory properties and may be produced at a lower cost. Plastics has been regarded as the most important invention in 20 century by Time magazine and polymers changed the whole world of materials science. Furthermore, since late 20 century, with the bloom of the polymer industry and research, functional polymers and smart polymer materials have been explored and developed for various new applications beyond the traditional polymers. Smart polymers, as the hottest and most promising branch in polymer science, have attracted tons of research scientists to devote their lifetime effort and promise a more colorful and charming future. The most commonly used examples of smart polymers: re-mendable polymers, electroactive polymers (EAPs) and ferroelectric polymers, are reviewed in the following paragraphs.

Re-mendable polymers or healable polymers are smart polymers which can recovery their damage upon external stimulus. The stimulus can be heating or even automatically for self-healing polymers. There are three main types of healable polymers based on the mechanism of healing agent stored and healing effect triggered. They are capsule based healable polymers, vascular based healable polymers and intrinsic healable polymers.[27-30] Details of the healable polymers are reviewed in Chapter 2.

Electroactive polymers (EAPs) are a group of smarting polymers which change shape and/or size under the stimulus of an electric field.[10,11] Based on the mechanism of actuation, EAPs are classified into two categories: electronic EAPs which are driven by electric field or columbic forces; and ionic EAPs which are driven by the motion and diffusion of ions in materials.[19-22] A sample of electronic EAPs is dielectric elastomers actuator. The structure of the actuators is an elastomeric film coated with electrodes on both sides. The two sides with electrodes are connected to an external power source. When a voltage is applied to the actuator device, the electrostatic attraction force acts. Due to the mechanical compression, the elastomer film contracts in the thickness direction and expands in the film plane directions.[12-18] The ionic EAPs as our topic in Chapter 5 are carefully explained and studied.

Ferroelectric polymers, maintain a permanent electric polarization that can be reversed or switched upon an external electric field, such as polyvinylidene fluoride (PVDF), are widely used in acoustic transducers and electromechanical actuators because of their inherent piezoelectric response, and as heat sensors because of their inherent pyroelectric response. Beyond those, solid state refrigerator based on the electrocaloric effect of ferroelectric polymers has attracted our great attention and investigation as in Chapter 6.

1.3 Importance of Composite Materials

Meanwhile, composite as materials made from two or more constituent materials with significantly different physical or chemical properties, they can provide superior and unique characteristics different from their individual components.[33] Similar to the long history of polymers, people made and used composite for many centuries. The earliest

uses of composites can date back to the 1500s B.C. when early Egyptians and Mesopotamian settlers used a mixture of mud and straw to create strong and durable buildings. This is a good example for fiber reinforced composites which is the most common configuration for composite system. Again, with the development of synthetic polymers, particularly plastics, the modern era of composites begins. In the early 1900s, plastics such as vinyl, polystyrene, phenolic and polyester were developed. On one hand, because those plastics alone could not provide enough strength for structural applications, reinforcement was needed to provide the strength, and rigidity. On the other hand, the easy processing character provide the great potential as composite matrix materials for those polymers. In 1935, Owens Corning introduced the first glass fiber and later the glass fiber was used to reinforce plastic polymers as the pioneer work of the Fiber Reinforced Polymers (FRP) industry as we know it today. When combined with a plastic polymer, it creates an incredibly strong structure and also lightweight materials. Many of the greatest advancements in composites were incubated by war. Because the requirements in lightweight applications in military aircraft during the World War II, the FRP industry was brought into real production from laboratory and developed extremely fast. Also engineers realized other benefits of composites beyond being lightweight and strong at the same time. It was discovered that fiberglass composites were transparent to radio frequencies, and then the material was utilized in sheltering electronic radar equipment. With time elapsed into the peaceful times, people began to try to fit composite into other markets to overcome the lower demand for military products. In the 1970s the composites industry began to mature. Better plastic resins and improved reinforcing fibers were developed. DuPont developed an aramid fiber known as Kevlar

and also Carbon fiber was developed around this time. Those new fibers with improved properties brings more choice for the fiber reinforced composites.[33] Beyond the traditional composites developed for structural applications, nowadays, the composite industry still rapidly growths with focusing on composites with various functions for renewable energy and other new applications and products. Corrosion chemical resistant composites are highly resistant to chemicals and will never rust or corrode. Boats made with fiberglass can stay in the highly corrosive salt water without rusting. Composites with conductive particles dispersed in polymers can provide tunable conductivity and are widely used in industry as a type of conducting polymers. In the newest scientific studies, composites utilize even better fibers and resins and many of which incorporate nano-materials to provide nanocomposites. [34-36]

Overall, based on the potential benefits comes from composite and the fast development of smart polymers, we focused on synthesizing different types of smarting polymers and composites and then explored their corresponding applications in this dissertation.

Reference:

[1]   M.V. Gandhi, "Smart Materials and Structures," Chapman & Hall, Boundary Row, London, 2002

[2]   R.C. Smith, "Smart Material System: Model Development," the society for Industrial and Applied Mathematics, Philadelphia, PA,2008

[3]   V. Giurgiutiu, "Review of Smart-Materials Actuation Solutions for Aeroelastic and Vibration Control," Journal of Intelligent Material Systems and Structures, vol. 11, no. 7, pp. 525–544, Jul. 2000.

[4]   C. G. Granqvist, A. Azens, J. Isidorsson, M. Kharrazi, L. Kullman, G. A. Niklasson, D. Risnnow, and M. Veszelei, "Towards the smart window: progress in electrochromics," vol. 218, pp. 273–279, 1997.

[5]   a. Michaelis, H. Berneth, D. Haarer, S. Kostromine, R. Neigl, and R. Schmidt, "Electrochromic Dye System for Smart Window Applications," Advanced Materials, vol. 13, no. 23, pp. 1825–1828, Dec. 2001.

[6]   H. a. Sodano, D. J. Inman, and G. Park, "A Review of Power Harvesting from Vibration Using Piezoelectric Materials," The Shock and Vibration Digest, vol. 36, no. 3, pp. 197–205, May 2004.

[7]   S. R. Anton and H. A. Sodano, "A review of power harvesting using piezoelectric materials (2003 – 2006)," vol. 1, 2007.

[8]   J. F. Alder and J. J. McCallum, "Piezoelectric crystals for mass and chemical measurements. A review," The Analyst, vol. 108, no. 1291, p. 1169, 1983.

[9]   S. B. Lang and S. Muensit, "Review of some lesser-known applications of piezoelectric and pyroelectric polymers," Applied Physics A, vol. 85, no. 2, pp. 125–134, Sep. 2006.

[10]   Y. Bar-Cohen, "Electroactive Polymer (EAP) Actuators as Artificial Muscles: Reality, Potential, and Challenges," Second Edition, SPIE Press, 2004

[11]   P. Brochu and Q. Pei, "Advances in dielectric elastomers for actuators and artificial muscles.," Macromolecular rapid communications, vol. 31, no. 1, pp. 10–36, Jan. 2010.

[12]   S. Yun, X. Niu, Z. Yu, W. Hu, P. Brochu, and Q. Pei, "Compliant silver nanowire-polymer composite electrodes for bistable large strain actuation," Advanced materials (Deerfield Beach, Fla.), vol. 24, no. 10, pp. 1321–7, Mar. 2012.

[13]   R. Pelrine, R. Kornbluh, J. Joseph, R. Heydt, Q. Pei, and S. Chiba, "High-field deformation of elastomeric dielectrics for actuators," Materials Science and Engineering: C, vol. 11, no. 2, pp. 89–100, Nov. 2000.

[14]   R. Pelrine, "High-Speed Electrically Actuated Elastomers with Strain Greater Than 100%," Science, vol. 287, no. 5454, pp. 836–839, Feb. 2000.

[15]   S. M. Ha, W. Yuan, Q. Pei, R. Pelrine, and S. Stanford, "Interpenetrating Polymer Networks for High-Performance Electroelastomer Artificial Muscles," Advanced Materials, vol. 18, no. 7, pp. 887–891, Apr. 2006.

[16]   Q. Pei, M. Rosenthal, S. Stanford, H. Prahlad, and R. Pelrine, "Multiple-degrees-of-freedom electroelastomer roll actuators," Smart Materials and Structures, vol. 13, no. 5, pp. N86–N92, Oct. 2004.

[17]   Z. Yu, W. Yuan, P. Brochu, B. Chen, Z. Liu, and Q. Pei, "Large-strain, rigid-to-rigid deformation of bistable electroactive polymers," Applied Physics Letters, vol. 95, no. 19, p. 192904, 2009.

[18]   W. Yuan, L. B. Hu, Z. B. Yu, T. Lam, J. Biggs, S. M. Ha, D. J. Xi, B. Chen, M. K. Senesky, G. Grüner, and Q. Pei, "Fault-Tolerant Dielectric Elastomer Actuators using Single-Walled Carbon Nanotube Electrodes," Advanced Materials, vol. 20, no. 3, pp. 621–625, Feb. 2008.

[19]   J. D. W. Madden, B. Schmid, M. Hechinger, S. R. Lafontaine, G. A. Peter, F. S. Hover, R. Kimball, and I. W. Hunter, "Application of Polypyrrole Actuators : Feasibility of Variable Camber Foils," 2003.

[20]   S. Ramakrishna, J. Mayer, E. Wintermantel, and K. W. Leong, "Biomedical applications of polymer-composite materials: a review," Composites Science and Technology, vol. 61, no. 9, pp. 1189–1224, Jul. 2001.

[21]   Z. Yu, D. Xi, T. Lam, and Q. Pei, "Nanoporous carbon nanotube electrode for stable polypyrrole actuator," SPIE processding, vol. 6524, pp. 652420–652420–9, Apr. 2007.

[22]   M. Pyo, C. C. Bohn, E. Smela, J. R. Reynolds, and A. B. Brennan, "Direct Strain Measurement of Polypyrrole Actuators Controlled by the Polymer / Gold Interface," no. 27, pp. 916–922, 2003.

[23]   Q. Meng and J. Hu, "A review of shape memory polymer composites and blends," Composites Part A: Applied Science and Manufacturing, vol. 40, no. 11, pp. 1661–1672, Nov. 2009.

[24]   K. Otsuka and C. M. Wayman, "Shape Memory Materials", Cambridge University Press, 1998

[25]   Y. Liu, H. Lv, X. Lan, J. Leng, and S. Du, "Review of electro-active shape-memory polymer composite," Composites Science and Technology, vol. 69, no. 13, pp. 2064–2068, Oct. 2009.

[26]   C. Liu, H. Qin, and P. T. Mather, "Review of progress in shape-memory polymers," Journal of Materials Chemistry, vol. 17, no. 16, p. 1543, 2007.

[27]   R. P. Wool, "Self-healing materials: a review," Soft Matter, vol. 4, no. 3, p. 400, 2008.

[28]   D. Y. Wu, S. Meure, and D. Solomon, "Self-healing polymeric materials: A review of recent developments," Progress in Polymer Science, vol. 33, no. 5, pp. 479–522, May 2008.

[29]   B. J. Blaiszik, S. L. B. Kramer, S. C. Olugebefola, J. S. Moore, N. R. Sottos, and S. R. White, "Self-Healing Polymers and Composites," Annual Review of Materials Research, vol. 40, no. 1, pp. 179–211, Jun. 2010.

[30]   E. B. Murphy and F. Wudl, "The world of smart healable materials," Progress in Polymer Science, vol. 35, no. 1–2, pp. 223–251, Jan. 2010.

[31]   Andrew J. Lovinger, "Ferroelectric Polymers", Science, Vol. 220 no. 4602 pp. 1115-1121, 1983

[32]   Hari S. Nalwa, "Ferroelectric Polymers: Chemistry, Physics, and Applications", Marcel Dekker. Inc, New York, 1995

[33]   D. Hull and T.W.Clyne, "An Introduction to Composite Materials", Cambridge University Press, 1996

[34]   P. M. Ajayan, O. Stephan, C. Colliex, D. Trauth, "Aligned Carbon Nanotube Arrays Formed by Cutting a Polymer Resin—Nanotube Composite", Science, Vol.265 no 5176 pp 1212-1214, 1994

[35]   Z.-M. Huang, Y.-Z. Zhang, M. Kotaki, and S. Ramakrishna, "A review on polymer nanofibers by electrospinning and their applications in nanocomposites", Composites Science and Technology, vol. 63, no. 15, pp. 2223–2253, 2003.

[36]   G. Wei and P. X. Ma, "Structure and properties of nano-hydroxyapatite/polymer composite scaffolds for bone tissue engineering," Biomaterials, vol. 25, no. 19, pp. 4749–57, 2004.

CHAPTER TWO

Development of healable polymer / functionalized glass fiber composite material as aerospace structural materials

2.1 Introduction

The application of high strength polymers reinforced with fibers as composite in certain aerospace application is commonly used thanks to the low weight and high strength property of the composite. On the other hand, one of the most disadvantages of polymeric composite materials is failure due to growth of subcritical damage during use. These damages usually occur in the matrix polymer materials in the form of delamination and matrix cracking. This damage is caused by impact or overloading and if the impact prorogates, it will lead to completely failure.[1] In current composite systems, subcritical damage is difficult to be detected and also takes a long time to check. Additionally, repairing detected damage is expensive, and for the case of satellite/space vehicles, may not be possible. Therefore, if polymer matrix can have the ability to heal damages in-situ or even self-healable, it will increased the reliability as well as the life time of the composite very much. Various methods and improvements have been addressed to making healable polymers over the past years. [2-4]

Generally, there are three main groups of healable polymers based on their different mechanism used to store the healing functionality until triggered by damage. The way of the functionality units stored in the polymers determines the damage volume that can be healed, the repeatability of healing and the recovery rate for each approach. Basically, the three groups of healable polymers are capsule based healable polymers, vascular based

healable polymers and intrinsic healable polymers.[5] An illustration for each type of healable polymers are shown in Figure 2.1.[5]
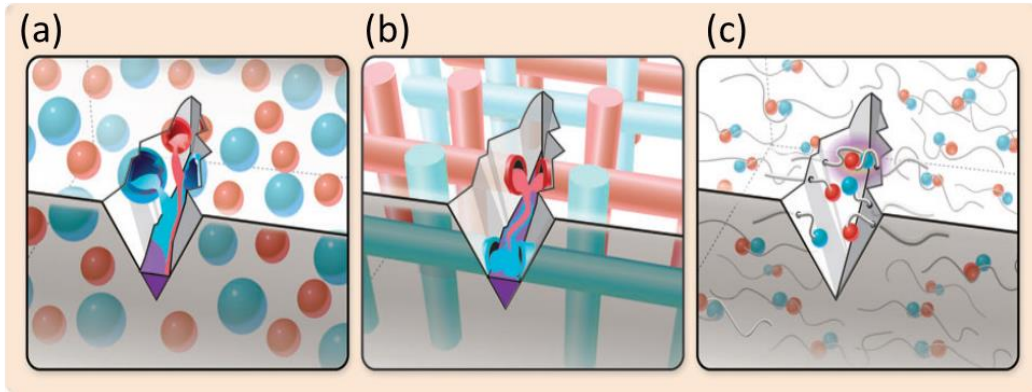
Figure 2.1 Illustrations of three approaches of healable polymers according to the healing mechanism include (a) capsule based, (b) vascular based and (c) intrinsic healable polymer (Reproduced from [5])

In capsule-based healable polymers, the healing agent is stored in capsules until the damage occurs and the capsules break by damages. When the capsules are broken, the healing agent in the capsulation will be released and the reaction of the healing agent will help to heal the damage. For this type of healing mechanism, once the capsules is broken, the healing agent will be depleted therefore it cannot support further damage healing. Capsule based healable polymers can only heal once at the same damage area. [2-5]

Capsule-based healable polymer materials have been developed with various type of schemes based on the different ways of capsules stored and dispersed in the polymer matrix. In each type of scheme, the healing agent is capsuled in an undispersed capsulation until the damage triggers release.[2-5] In Figure 2.2, it shows four different schemes which are the most used ones.[5]
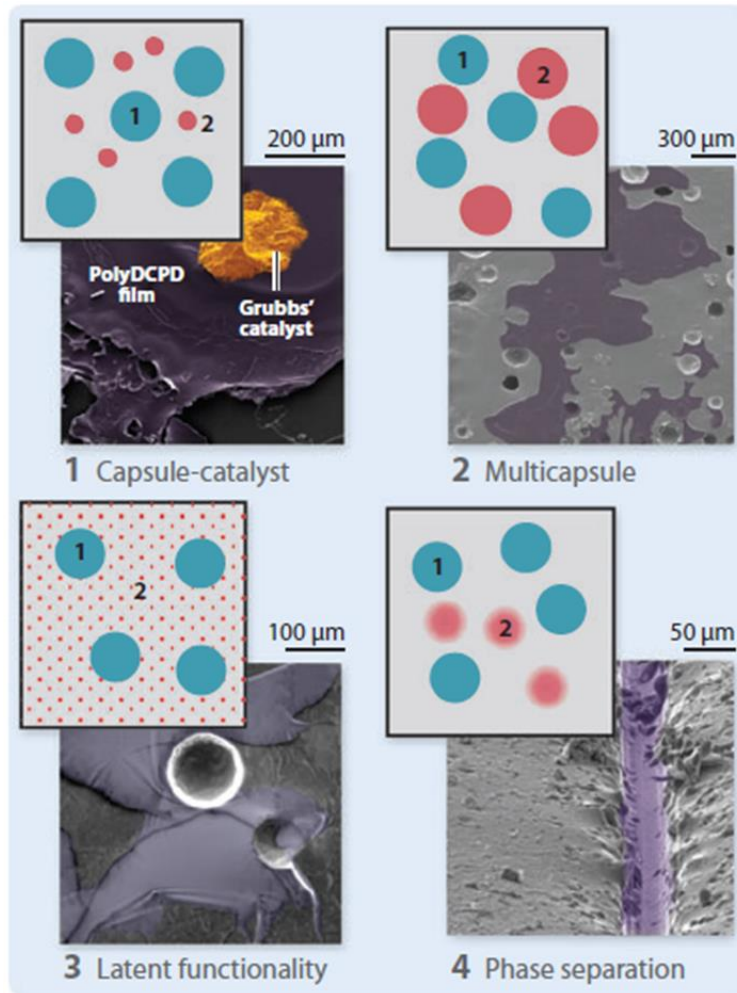
Figure 2.2 Four different schemes of capsule-based healable polymers, (1) dispersed capsule and catalyst coexisted type, (2) multi-capsules coexisted type, (3) latent functionality type and (4) phase separation type. (Reproduced from [5])

For type 1 shown in Figure 2.2 with both dispersed capsules and catalyst, we have both healing agent liquid capsules and also polymerizer catalyst dispersed in polymer matrix systems.[5] The capsules are represents as big blue dot 1 in Figure 2.2 (1) and the catalyst is represents as small pink dot 2 in Figure 2.2 (1). Upon damage, capsules will break and release the healing agent which will reacted to heal the wound as long as they get in touch with the catalyst in polymers. The most famous example for this type is the

12

dicyclopentadiene (DCPD)-Grubbs's capsule-catalyst system established by White et al.[6-10] DCPD was encapsulated and then polymerized through ring-opening metathesis polymerization (ROMP) via Grubbs' catalyst. The healing mechanism and healing efficiency have been very well studied. People have used this DCPD-Grubbs' healable system into epoxy polymers and their composite.

For type 2 multi-capsules type, both the healing agent and the polymerizers are encapsulated and dispersed in polymer matrix. This multi-capsules technique will capsule all the components needed for the healing reaction to occurs. With this method, it broadens the types of healing agent.[5] One of the earliest example is using two distinct capsules each filled with one part of the two-part Sylgard® 180 poly-dimethylsiloxane (PDMS) in an elastomeric matrix.[11] The healing reaction among this two encapsulations is a platinum-catalyzed hydrosilylation of vinyl-terminated PDMS resin.

The third type is called as latent functionality.[5] The healing agent is encapsulated or dispersed in the matrix polymer as particles and then reacted with residual reactive functional groups from the matrix polymers. Except the functional groups, the polymerizer can also be a type of environmental stimulus. When there is a damage to break the capsules, the healing agent polymerized with the help of external environmental stimulus. On good example for this latent systems is the solvent-promoted and resin-solvent healable polymer system.[12, 13] Residual amine functionality in the epoxy matrix is used to initiate polymerization of the healing agent released from the capsules.

For the last type 4, either the healing agent or the polymerizer, at least one component is phase separated with the matrix. [14, 15] Upon damage, the capsulated healing agent or

catalyst will release and if they get contact with the separated phase, the whole healing system will get chance to polymerize and heal the damage. One example is phase separated hydroxyl end-functionalized polydimethylsiloxane (HOPDMS) and polydiethoxysiloxane (PDES) mixture in an epoxy vinyl ester matrix. The tin catalysts were kept in capsules dispersed in matrix and the HOPDMS/PDES are phase separated as droplets in the matrix. When the damage induced Ti catalyst release, then it catalyzed the reaction of the phase separated HOPDMS/PDES.

The second approach for healable polymer system is vascular based healable polymers.[2-5] In order to allow multiple healing at the same location, people began to use network hollow fibers or capillaries as vascular to substitute microcapsules. The healing agent is stored in the network vascular. Upon damage, the healing agent is released to heal the wound. Because it can be refilled from external injection source or other connected fibers which has not been used, this type of design ensures the ability of multiple healing at the same location. As shown in Figure 2.3, people tried to make from 1D to 3D vascular network to hold the healing agents.[5]
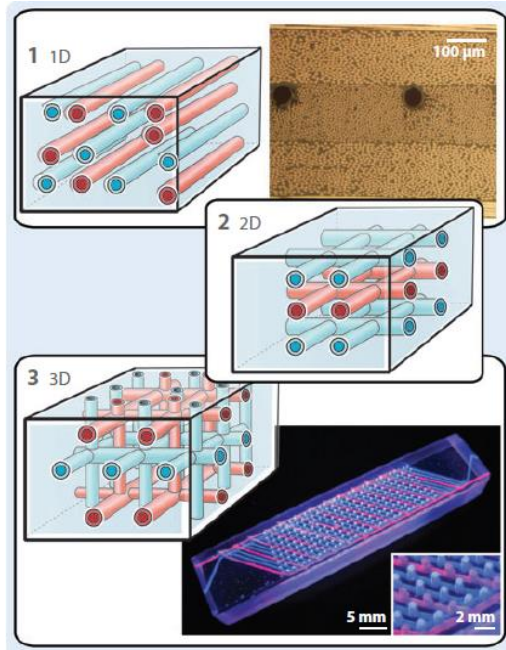
Figure 2.3 Vascular based healable polymer systems from one-dimension (1D) to three-dimensions (3D) networks. (Reproduced from [5])

Currently, people use hollow glass fibers (HGFs) with around 60 μm diameter as channels filled with appropriate healing agent to make the 1D vascular healable system.[16-19] HFGs are compatible with many polymer matrixes such as epoxy. Also, they are inert to most popular self-healing agents such as two part epoxy resin systems. Therefore, HGFs filled with two parts epoxy resin and composite within epoxy matrix is the pioneer work. For 2D and 3D vascular networks, people also did carefully study from both the healing agent types and also the built up of the network whose details can be easily found in literatures. On the other hand, the complicate fabrication process of the vascular system together with the composite inherent limits the application of this type of healable polymer systems. Therefore, intrinsic healable polymer with repeatable healing ability is in great demand.

Intrinsic healable polymers as a type of smart polymers achieve repair because of the inherent reversible bonding in the polymers.[2-5] Intrinsic healing is achieved through hydrogen bonding, ionomeric coupling, a dispersed meltable thermoplastic phase and thermally reversible reactions and so on.[5] The explanations and examples for some types of intrinsic healable polymers are listed as follows.

A hydrogen bond is the electromagnetic attractive interaction between polar molecules in which hydrogen (H) is bound to a highly electronegative atom, such as nitrogen (N), oxygen (O) or fluorine (F). Hydrogen bonds are widely existed in supermoleculars which are formed through hydrogen bonds or polymers which have end groups or side groups can form hydrogen bond. Because the hydrogen bonding is reversible, for the above supermoleculars or polymers will be self-healable due to the naturally reforming ability of hydrogen bond.[5] A supermolecular self-healing rubbery material has been developed as an example for this type of healable polymers. The molecular structure and the illustration of the supermolecule network are shown in Figure 2.4.[20] It introduces three types of functional groups, which are amidoethyl imidazolidone, di(amido ethyl)urea and diamido tetraethyl triurea, are able to strongly associate through multiple hydrogen bonds to form the supermolecule. The reversibility of the hydrogen bonds give the self-healing ability of this material.
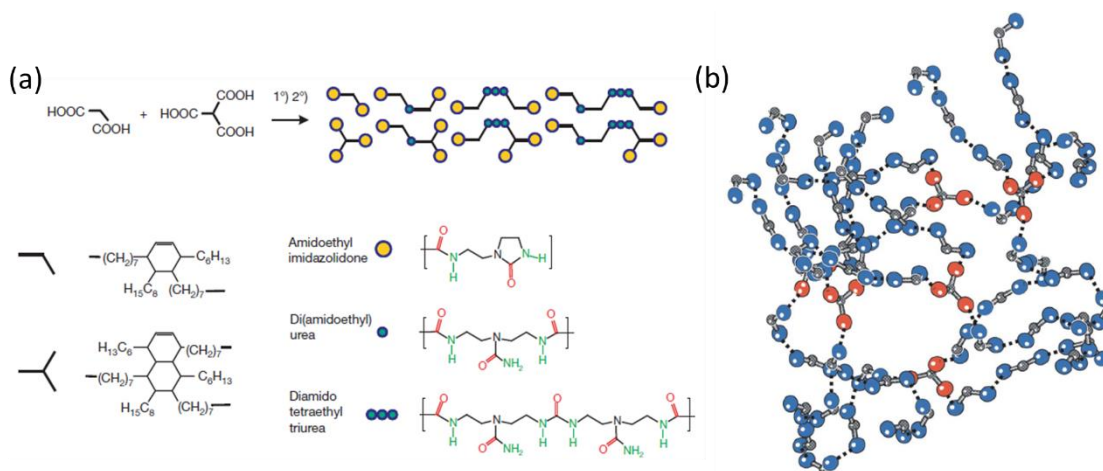
Figure 2.4 (a) A synthesis scheme show a mixture of fatty diacid and triacid is condensed first with diethylene triamine and then reacted with urea to give a mixture of oligomers equipped with complementary hydrogen bonding groups. The hydrogen bond acceptors are shown in red, donors in green. (b) Schematic view of a reversible supermolecule formed by mixtures of ditopic (blue) and tritopic (red) molecules. (Figure reproduced from [20])

Ionomeric healable polymers normally have ionic segments that can form clusters. The clusters act as reversible cross-links to realize the healable property of the polymers. Because the formation of the clusters is reversible and repeatable, multiple local healing is possible for this type of healable polymer. The healing can be activated by external stimuli such as temperature or UV light.[2-5] In Figure 2.5, it is an illustration to show the ionomeric healing process.[21, 22] P(ethylene-*co*-methacrylic acid) (EMAA) copolymers with ionic segments is healable polymers based on such a healing mechanism.
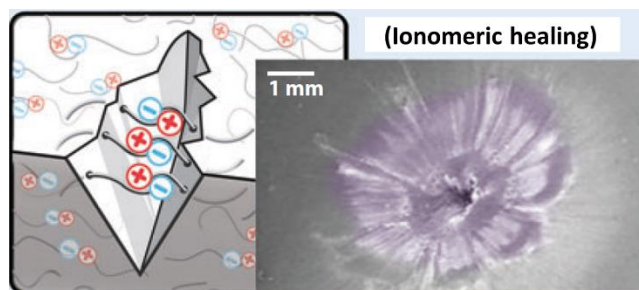
Figure 2.5 Illustration of healing mechanism of ionomeric healable polymer (Reproduced from [5])

Adding dispersed meltable thermoplastic polymer into thermoset polymers creates a new type of healable polymers.[5] The advantage for these type of healable polymers is that they can be processed using existing manufacturing technology for traditional thermosets. Also, this type of healable polymers can perform repeatable healing on the same wound area. When there is a damage on the material, through heating the sample above the melting point of the thermoplastic additives, the thermoplastic material will flow into the crack plane, heal the crack and mechanically interlock with the surrounding matrix polymers. One example for this type of healable polymers is dispersed thermoplastic linear poly(bisphenol-A-coepichlorohydrin) into an epoxy composite.[23, 24] The adding of thermoplastic additives reduced delamination area, eliminated matrix crack and allowed for recovery of damage after thermal healing.

Lastly, Diels-alder (D-A) based polymers are one of most promising healable polymers which invented by Dr. Wudl.[25, 26] This type of polymers generally are copolymer from multi-furan based monomer and multi-maleimide based monomer. Furan and maleimide functional groups will react through a reversible Diels-Alder (D-A) cyclo-addition reaction to form the healable network polymer. The C-C covalent bond formed

in the D-A reaction is weaker than the other covalent bonds initially present in the two monomers and could break upon mechanical stress to regenerate the furan and maleimide functional groups. Thanks to the reversibility of the D-A reaction, the furan and maleimide groups can cross-couple again under modest heating to re-form the broken bonds. Therefore, cracks in this copolymer can heal for multiple times or re-mend. The reversible Diels-Alder cycle-addition reaction through furan and maleimide groups is illustrated as in Figure 2.6.

Furan   Maleimide

Figure 2.6 Reversible Diels-Alder cycle-addition reaction (Reproduced from [25])

The first D-A based healable polymer is 3M4F with monomer chemical structure shown as in Figure 2.7. Later, the same groups developed healable polymer 2ME4F and 2MEP4F from respectively monomers also shown in Figure 2.7. The 2ME4F and 2MEP4F polymers need easier polymerization procedure without solvent and also higher healing efficiency and higher strength. 2MEP4F has been shown to have virtually 100% healing efficiency of fracture toughness. Due to its high mechanical strength comparable with commercial epoxy, moderate glass transition temperature (Tg=80°C) and good repeating healing ability, 2MEP4F is chosen as a potential candidate to composite with carbon fibers as structural material in aerospace application.
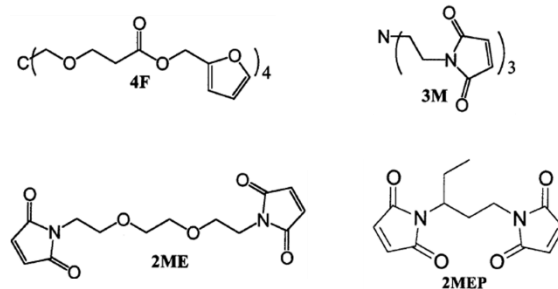
Figure 2.7 Monomer structures for D-A based healable polymer 3M4F, 2ME4F and 2MEP4F. (Reproduced from [25, 26])

Using 2MEP4F as matrix healable polymer composite with carbon fiber as structural material in aerospace application has been well studied by Dr. Park and Dr. Riendeau. It was demonstrated that matrix polymer 2MEP4F with cracking on the order of 1mm can be healed with heat alone. Damage was created by modified short beam shear and thermal shock. Mechanical properties of this type can be recovered with healing efficiencies of around 90%. Although the carbon fiber composite with 2MEP4F is already a good choice, the adhesion between the 2MEP4F and the carbon fiber still need to be increased. The properties of composites are largely governed by the interactions at the interface between the components of the composite. In the case of carbon fiber composites, a critical interface interaction is between carbon fiber reinforcement and the resin matrix. The adhesive properties of the resin and the ability of the polymer to bond to the carbon fiber are critical. When the material properties of epoxy and 2MEP4F are compared, they are quite similar and can be expected to result in carbon fiber composites with similar properties. In some of the testing performed during this work, the epoxy composites were shown to have improved strength relative to the 2MEP4F composite. If the resin properties are similar, the difference in strength must be due to the interaction

between the resin and the fiber reinforcement. Based on the analysis, it is clearly that the main reason for fracture failure of the composite is delamination between the reinforced carbon fiber and the 2MEP4F polymer matrix. Glass fiber is another common reinforce candidate in composite material system. The unique strong mechanical property together with more active surface chemistry and more tractable surface chemistry reaction made it as our new candidate in our composite.[27-30] In this chapter, our aim is to put organic tails with maleimide end group on surface of glass fiber which can join the reaction of D-A reaction during the polymer matrix formation to achieve better adhesion between fibers and polymers. To successfully put maleimide group on glass fiber, we firstly treated glass fibers through silanization and then did Michael addition reaction to glass fibers. A series of experiments were performed to evaluate the interface interactions of the 2MEP4F resin with glass fibers. By functionalizing the glass fiber surface to be compatible with the 2MEP4F resin, improved interfacial interactions and improved bulk properties were observed.

2.2 Experiments

2.2.1 Materials

Commercial available unidirectional glass fiber fabric (Hexcel HexForce SA060) was purchased from Fiberglass Supply Inc. for surface functionalization experiments. The material was chosed based on the unidirectional fiber orientation and a fabric density comparable to the carbon fiber used throughout this investigation. The fabric is intended for use with epoxy composite, suggesting the surface functionality is optimized for resins such as Epon 862. 3-aminopropyltriethoxysilane (APTEs) was obtained from Sigma Aldrich. 1,1′-(Methylenedi-4,1-phenylene)bismaleimide (MDPB) 95% was also gained

from Sigma Aldrich. All other solvents such as ethanol, propylene carbonate, tetrahydrofuran (THF) were all purchased from Sigma Aldrich.

2.2.2 Glass fibers functionalization

Commercial available glass fiber sheet were washed with acetone under sonication for 30 minutes to remove any impurity from processing and shipping before the silanization. After cleaning, the cleaned glass fibers were put in 5wt% of 3-aminopropyltriethoxysilane (APTEs) ethanol solution. The reaction was kept at 75 ^{o}C for 24 hours. After reaction, the glass fibers were sintered at 120 ^{o}C for 2 hours which condensed the functionalized APTE group on the glass fibers surface. The final aim to do the treatment to glass fibers is to composite it to 2MEP4F polymer matrix. Therefore, after the glass fibers treatment, the glass fibers sheet should keep the original bundle shape. The in-solution method of silanization in ethanol for 24 hours will partially dissolved the material holding the glass fiber tows together. Therefore, a vapor phase reaction with APTEs was developed instead of in-solution method. The whole piece of the glass fibers with size of 12cm *8 cm was put in vacuum oven with 5 g APTE in an open petridish. The vapor phase reaction was run under 1torr vacuum at 90 ^{o}C for 24 hours followed by annealing of the silane at 120 ^{o}C for 2 hours. Amine content on the glass fiber was confirmed using Ninhydrin testin and FTIR measurement. Amine functionalized fiber was reacted with 1,1′-(Methylenedi-4,1-phenylene)bismaleimide (MDPB) in propylene carbonate at 80 ^{o}C for 2 hours to introduce maleimide functional groups to the fiber through Michael addition.[31] After reaction, the MDPB treated glass fibers were washed with THF for four times. FTIR measurements and Ninhydrin tests

were conducted to MDPB treated glass fibers as well. The FTIR measurement was done with a FT-IR model 420, JASCO. The Ninhydrin test solution is 10wt% of Ninhydrin dye dissolved in ethanol.[32] APTE and MDPB reaction on glass surface were illustrated in Figure 2.8.
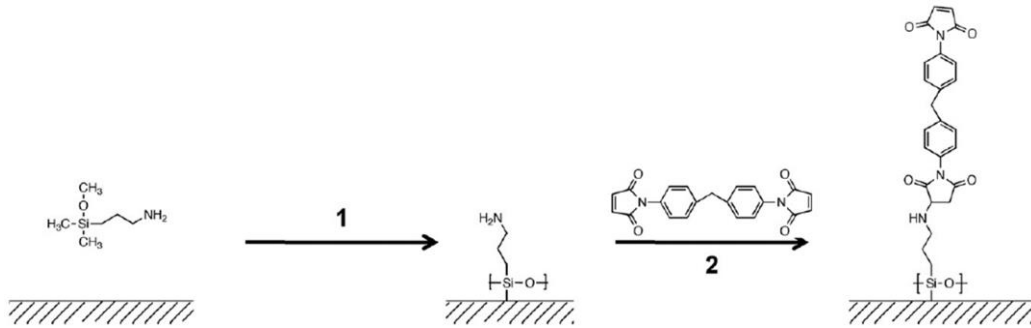
Figure 2.8 Scheme of APTEs reaction on glass surface (step 1) and subsequently MDPB reaction on the treated surface (step 2) (Reproduced from [31])

2.2.3 Composite coupons fabrication

To evaluate the effect of glass fibers functionalization, the as-received and functionalized glass fibers reinforced composite samples which named as coupons for SBS testing in this work were fabricated with both 2MEP4F and Epon 862. All coupons were fabricated for testing with a [0, 0, 90] 2s layup fiber orientation as we did previously with carbon fiber reinforced composite coupons. Epon 862 and curing agent W were mixed with a mass ratio of 100: 26.4. The Epon 862 panels were cured at 120 $^\circ$C for 5 hours. The 2MEP and 4F monomers are synthesized as described in literature. The furan is a viscous liquid at room temperature and the maleimide is a solid that can be melt and mixed with the furan. Both 2MEP and 4F monomers were co-dissolved in dichloromethane and pre-polymerized at 30 ^{0}C. After this pre-polymerization stage, solvent dichloromethane was

removed at 30 ^{0}C which yielded a semi-viscous, single-phase liquid. The liquid pre-polymer was used for a wet lay-up with the composited fibers. After the pre-polymer thoroughly wetting the glass fibers, the composite mixture were placed in a mold under light pressure and heated to 90 ^{o}C to cure for overnight. In this work, SA060 glass fibers, APTE-glass fibers and MDPB-glass fibers were used in the composite coupons fabrication. The size of the each coupon is 4cm ×4cm in area with thickness around 1.1-1.2mm.

2.2.4 Short beam shear testing

Short beam shear (SBS) testing was used to compare the quality of different panel fabrication methods and to evaluate healing. Inter-laminar shear strength is used to compare resin systems and fabrication methods. Recovery of inter-laminar shear strength is used to evaluate healing of the composites. Short beam shear testing was done in accordance with ASTM D2344. For each group of composite samples, we made 2 large piece coupons which provided 8 samples to provide valid and repeatable testing result. The typical span used for testing was 20mm and the cross-head speed was 1mm/min. Specimen thickness varied between 1.1mm and 1.2mm. The samples were loaded until there was a sharp decrease in stiffness, which corresponds to the formation of a delamination. The delamination length was typically about 6mm in length. Short beam strength was calculated in accordance with ASTM D2344 and stiffness was determined using the chord modulus as described in ASTM D7264.

2.3 Results and Discussion

2.3.1 Glass fiber functionalization

We would like to verify the reaction of glass fibers with APTEs and further reaction with MDPB. Therefore Fourier Transform Infrared Spectrum (FTIR) of as received glass fibers, APTEs and MDPB were taken as reference data which were shown as in Figure 2.9 (a), (b) and (c) respectively.
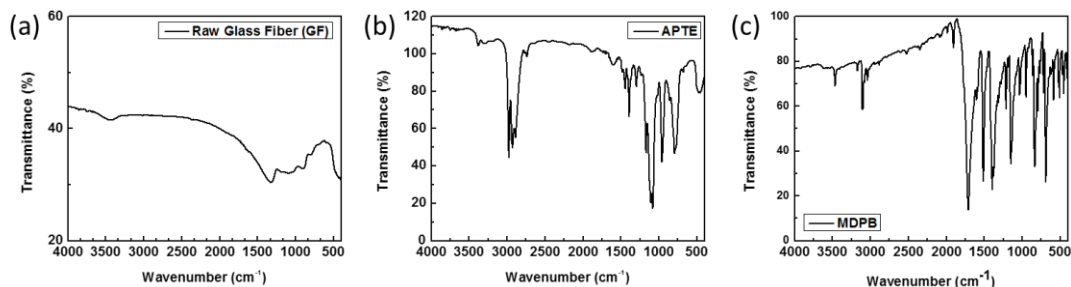
Figure 2.9 FTIR spectrum of as received glass fibers (a), APTEs (b) and MDPB (c).

As indicated in Figure 2.9 (a), purchased glass fiber as solvent cleaning shows a broad peak at around 3460cm^{-1} which dues to the –OH groups on surface of glass fibers. For APTEs, the FTIR spectrum as Figure 2.9 (b) shows all the representative peaks. The double peaks in the range of 3250cm^{-1} to 3400cm^{-1} come from primary amine N-H stretch. The sharp peaks in the range of 2850cm^{-1} to 3000cm^{-1} and in the range of 1350cm^{-1} to 1480cm^{-1} are responsible to C-H stretch and C-H bending respectively. The peaks in the range of 1080cm^{-1} to 1360cm^{-1} belongs to the –C-N stretching in APTEs and the peaks. For MDPB FTIR spectrum Figure 2.9 (c), the most representative peak is the sharpest peak with highest absorption at 1705cm^{-1} from carbonyl group C=O stretch.[33] The representative peaks for both APTEs and MDPB are the targeting peaks we would like to see from FTIR spectrum of the functionalized glass fibers.

The glass fibers treated with APTEs through both in-solution reaction and vapor phase reaction were checked with FTIR. In Figure 2.10, the spectrum for vapor phase treated glass fibers from wavenumber as 3600 to 2600 cm^{-1} range is given for details analysis.
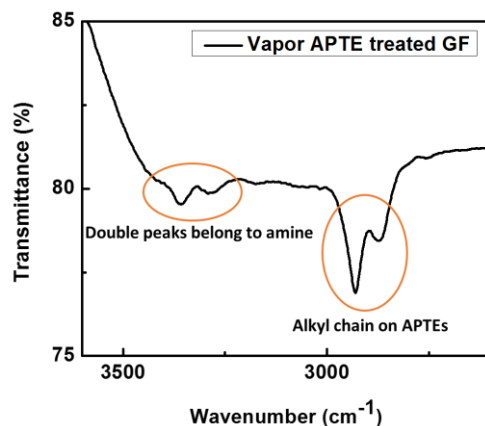
Figure 2.10 FTIR spectrum for APTEs treated glass fiber through vapor phase reaction

As clearly indicated in Figure 2.10, double peaks in the range of 3400-3250 cm^{-1} belongs to the primary amine N–H stretch of the NH$_2$ groups on APTEs. The sharp double peaks at 2930 cm^{-1} and 2873 cm^{-1} are due to the C-H stretch of the alkyl (-CH$_2$CH$_3$) groups of APTEs tails. Clearly, the 3-aminopropyltriethoxy (APTEs) group were successfully reacted on to the surface of glass fiber.

To compare the two APTEs treatment method, FTIR spectrum of APTEs treated glass fiber for both vapor phase and in solution 24 hours treatment was given in Figure 2.11 (a). If we compared the two methods, it is clear that vapor phase reaction even works better which gives more clear peaks. As we known, ninhydrin as a kind of dye will react with primary amine to show deep blue or purple color. To ensure the success of our APTEs treatment reaction on glass fiber, Ninhydrin test was done on the treated glass fibers. As

shown in Figure 2.10 (b), the APTE treated glass fiber turned into deep purple color while the raw glass fiber without treatment still keep its original colorless.
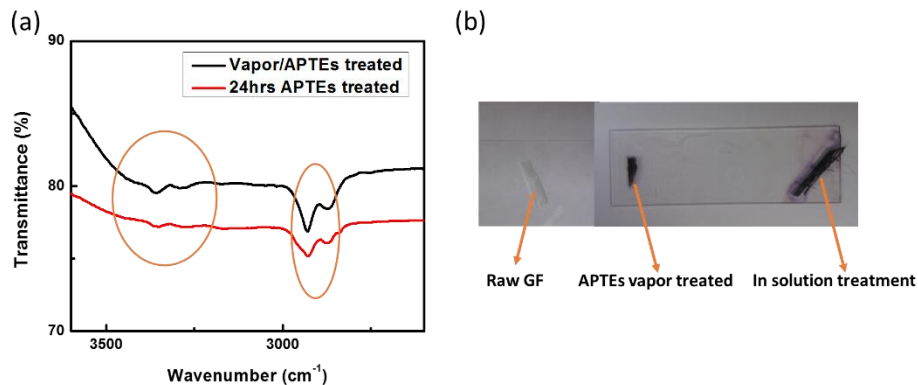
Figure 2.11 (a) FTIR spectrum for APTEs treated glass fiber for both vapor phase and in solution 24 hours treatment. (b) Photo image shows Ninhydrin testing color response on as received raw glass fiber and APTEs treated glass fibers.

Similarly, the MDPB treated glass fibers were also checked with FTIR and Ninhydrin test. The FTIR spectrum for MDPB treated glass fibers is shown in Figure 2.12 (a) and the Ninhydrin test result is in Figure 2.12 (b).
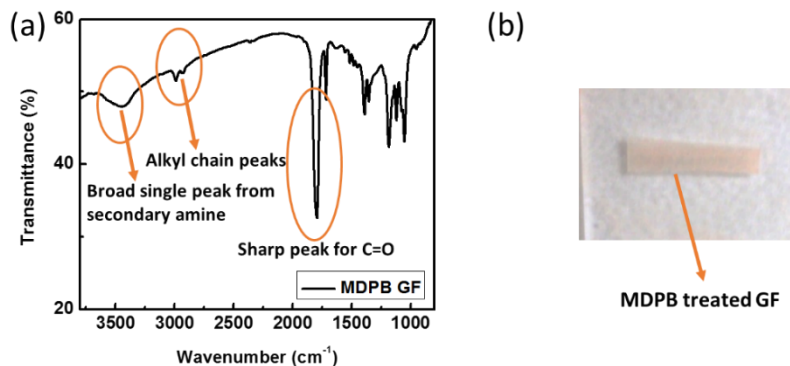
Figure 2.12 (a) FTIR spectrum for MDPB treated glass fibers (b) Photo image shows Ninhydrin testing on MDPB treated glass fibers.

The FTIR spectrum shown in Figure 2.12 (a) clearly indicates the success of putting maleimide tail on glass fibers surface. The broad single peak show in the range of 3400cm^{-1} to 3550cm^{-1} belong to the secondary amine N-H stretch. The most representative peak is the sharp peak at 1790cm^{-1} induced by C=O stretch of carbonyl group on maleimide structure. Furthermore, we ensured the success of this MDPB treating glass fiber reaction through ninhydrin dye test. As we know, ninhydrin dye will change into pinky-yellow color when it reacts with secondary amine. Clearly shown in Figure 2.12 (b), MDPB treated glass fibers turned to pink color in ninhydrin test.

2.3.2 SBS testing

After successfully putting maleimide groups on glass fibers surface, it is necessary to check the effect of functionalized glass fibers in composite system. Coupons for SBS testing were fabricated with both 2MEP4F and Epon 862 using the as received and functionalized glass fibers. In Figure 2.13 (a) and (b), it shown the SBS strength vs displacement curves for all three types of glass fibers composite with both Epon 862 and 2MEP4F polymer matrix, respectively. Table 2.1 summarizes the SBS strength data for all samples tested. A notable improvement for 2MEP4F composites with maleimide functionalized glass fibers (MDPB-GF) was observed while no change was observed with amine modified fibers (APTEs-GF). The maleimide fibers can participate in the Diels-Alder crosslinking of the 2MEP4F matrix whereas the amine fibers cannot. The strength increase for the MDPB-GF healable composite demonstrate the benefit of improved interfacial bonding between the resin and reinforcement for improved mechanical properties. The covalent bonding between maleimide moieties on MDPB-GF

and reactive species in 2MEP4F matrix resulted in the 20% increase in SBS strength relative to the control coupon with as received glass fiber.
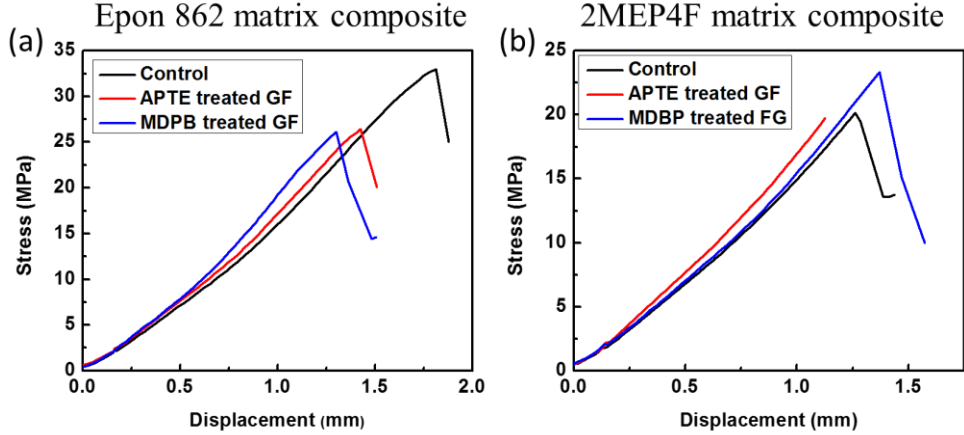
Figure 2.13 SBS strength strength vs displacement curves for (a) Epon 862 matrix and (b) 2MEP4F matrix composite with different glass fibers.

Table 2.1 SBS strength data for both Epon 862 and 2MEP4F composite with different glass fibers.

Matrix	Control GF SBS Strength (MPa)	APTE GF SBS Strength (MPa)	MDPB-GF SBS Strength (MPa)
2MEP4F polymer	19.02	19.63	23.16
Epon 862 polymer	32.51	26.69	26.82

As clearly summarized in table 2.1, a drop in mechanical performance was observed for Epon 862 composites with functionalized glass fibers. The as-received glass fiber is intended for use with epoxy composite systems and has been optimized by the manufacturer for maximum mechanical performance with resins such as Epon 862. Modification of this epoxy-specific surface with APTEs and MDPB resulted in altered

interfacial bonding with the epoxy and reduced the mechanical strength. Although the APTEs-GF contains amine moieties which can covalently bond with epoxide groups in the resin, the properties were reduced relative to the optimally functionalized glass fibers.

2.4 Conclusion and Future Work

Glass fibers were successfully functionalized by APTEs through silanization and by MDPB through Michael addition. 2MEP4F healable polymer and Epon 862 polymer composite coupons fabricated with as-received glass fibers and functionalized glass fibers were tested through short beam shear test. The SBS data suggest that functionalized glass fibers with MDPB groups on surface has successfully bonded with 2MEP4F polymer matrix as indicated through dramatically increasing of SBS strength. Therefore, further optimization of the functionalized MDPB-GF will continue to improve the mechanical Strength of 2MEP4F panels. Furthermore, the healing properties of the 2MEP4F polymer composite with optimized MDPB-glass fibers need to be carefully studied as an important future work.

Reference:

[1]   X. Wang, S. Wang, and D. D. L. Chung, "Sensing damage in carbon fiber and its polymer-matrix and carbon-matrix composites by electrical resistance measurement," vol. 4, pp. 2703–2713, 1999.

[2]   E. B. Murphy and F. Wudl, "The world of smart healable materials," *Progress in Polymer Science*, vol. 35, no. 1–2, pp. 223–251, Jan. 2010.

[3]   R. P. Wool, "Self-healing materials: a review," *Soft Matter*, vol. 4, no. 3, p. 400, 2008.

[4]   D. Y. Wu, S. Meure, and D. Solomon, "Self-healing polymeric materials: A review of recent developments," *Progress in Polymer Science*, vol. 33, no. 5, pp. 479–522, May 2008.

[5]   B. J. Blaiszik, S. L. B. Kramer, S. C. Olugebefola, J. S. Moore, N. R. Sottos, and S. R. White, "Self-Healing Polymers and Composites," *Annual Review of Materials Research*, vol. 40, no. 1, pp. 179–211, Jun. 2010.

[6]   S. R. White, N. R. Sottos, P. H. Geubelle, J. S. Moore, M. R. Kessler, S. R. Sriram, E. N. Brown, and S. Viswanathan, "Autonomic healing of polymer composites.," *Nature*, vol. 409, no. 6822, pp. 794–7, Feb. 2001.

[7]   E. Brown, S. White, and N. Sottos, "Retardation and repair of fatigue cracks in a microcapsule toughened epoxy composite – Part I: Manual infiltration," *Composites Science and Technology*, vol. 65, no. 15–16, pp. 2466–2473, Dec. 2005.

[8]   E. Brown, S. White, and N. Sottos, "Retardation and repair of fatigue cracks in a microcapsule toughened epoxy composite—Part II: In situ self-healing," *Composites Science and Technology*, vol. 65, no. 15–16, pp. 2474–2480, Dec. 2005.

[9]   J. D. Rule, N. R. Sottos, and S. R. White, "Effect of microcapsule size on the performance of self-healing polymers," *Polymer*, vol. 48, no. 12, pp. 3520–3529, Jun. 2007.

[10]   E. L. Kirkby, J. D. Rule, V. J. Michaud, N. R. Sottos, S. R. White, and J.-A. E. Månson, "Embedded Shape-Memory Alloy Wires for Improved Performance of Self-Healing Polymers," *Advanced Functional Materials*, vol. 18, no. 15, pp. 2253–2260, Aug. 2008.

[11]   M. W. Keller, S. R. White, and N. R. Sottos, "Torsion fatigue response of self-healing poly(dimethylsiloxane) elastomers," *Polymer*, vol. 49, no. 13–14, pp. 3136–3145, Jun. 2008.

[12]   M. M. Caruso, D. a. Delafuente, V. Ho, N. R. Sottos, J. S. Moore, and S. R. White, "Solvent-Promoted Self-Healing Epoxy Materials," *Macromolecules*, vol. 40, no. 25, pp. 8830–8832, Dec. 2007.

[13]   M. M. Caruso, B. J. Blaiszik, S. R. White, N. R. Sottos, and J. S. Moore, "Full Recovery of Fracture Toughness Using a Nontoxic Solvent‐Based Self‐Healing System," *Advanced Functional Materials*, vol. 18, no. 13, pp. 1898–1904, Jul. 2008.

[14]   S. H. Cho, S. R. White, and P. V. Braun, "Self-Healing Polymer Coatings," *Advanced Materials*, vol. 21, no. 6, pp. 645–649, Feb. 2009.

[15]   S. H. Cho, H. M. Andersson, S. R. White, N. R. Sottos, and P. V. Braun, "Polydimethylsiloxane-Based Self-Healing Materials," *Advanced Materials*, vol. 18, no. 8, pp. 997–1000, Apr. 2006.

[16]   S. Bleay, C. Loader, V. Hawyes, L. Humberstone, and P. Curtis, "A smart repair system for polymer matrix composites," *Composites Part A: Applied Science and Manufacturing*, vol. 32, no. 12, pp. 1767–1776, Dec. 2001.

[17]   J. W. C. Pang and I. P. Bond, "A hollow fiber reinforced polymer composite encompassing self-healing and enhanced damage visibility," *Composites Science and Technology*, vol. 65, no. 11–12, pp. 1791–1799, Sep. 2005.

[18]   J. W. C. Pang and I. P. Bond, "'Bleeding composites'—damage detection and self-repair using a biomimetic approach," *Composites Part A: Applied Science and Manufacturing*, vol. 36, no. 2, pp. 183–188, Feb. 2005.

[19]   R. S. Trask and I. P. Bond, "Biomimetic self-healing of advanced composite structures using hollow glass fibres," *Smart Materials and Structures*, vol. 15, no. 3, pp. 704–710, Jun. 2006.

[20]   P. Cordier, F. Tournilhac, C. Soulié-Ziakovic, and L. Leibler, "Self-healing and thermoreversible rubber from supramolecular assembly.," Nature, vol. 451, no. 7181, pp. 977–80, Feb. 2008.

[21]   S. J. Kalista and T. C. Ward, "Thermal characteristics of the self-healing response in poly(ethylene-co-methacrylic acid) copolymers.," Journal of the Royal Society, Interface / the Royal Society, vol. 4, no. 13, pp. 405–11, Apr. 2007.

[22]   S. J. Kalista, T. C. Ward, and Z. Oyetunji, "Self-Healing of Poly(Ethylene-co-Methacrylic Acid) Copolymers Following Projectile Puncture," Mechanics of Advanced Materials and Structures, vol. 14, no. 5, pp. 391–397, Jun. 2007.

[23]   S. a Hayes, W. Zhang, M. Branthwaite, and F. R. Jones, "Self-healing of damage in fibre-reinforced polymer-matrix composites.," *Journal of the Royal Society, Interface / the Royal Society*, vol. 4, no. 13, pp. 381–7, Apr. 2007.

[24]   S. a. Hayes, F. R. Jones, K. Marshiya, and W. Zhang, "A self-healing thermosetting composite material," Composites Part A: Applied Science and Manufacturing, vol. 38, no. 4, pp. 1116–1120, Apr. 2007.

[25]   X. Chen, F. Wudl, A. K. Mal, H. Shen, and S. R. Nutt, "New Thermally Remendable Highly Cross-Linked Polymeric Materials," Macromolecules, vol. 36, no. 6, pp. 1802–1807, Mar. 2003.

[26]   X. Chen, M. a Dam, K. Ono, A. Mal, H. Shen, S. R. Nutt, K. Sheran, and F. Wudl, "A thermally re-mendable cross-linked polymeric material.," Science (New York, N.Y.), vol. 295, no. 5560, pp. 1698–702, Mar. 2002.

[27]   J. S. Park, H. S. Kim, and H. Thomas Hahn, "Healing behavior of a matrix crack on a carbon fiber/mendomer composite," *Composites Science and Technology*, vol. 69, no. 7–8, pp. 1082–1087, Jun. 2009.

[28]   J. S. Park, T. Darlington, A. F. Starr, K. Takahashi, J. Riendeau, and H. Thomas Hahn, "Multiple healing effect of thermally activated self-healing composites based on Diels–Alder reaction," *Composites Science and Technology*, vol. 70, no. 15, pp. 2154–2159, Dec. 2010.

[29]   K. Takahashi, Z. Guo, Y. Wang, E. Bolanos, C. Hamann-Schaffner, E. Murphy, F. Wudl, and H. T. Hahn, "Towards Development of a Self-Healing Composite using a Mendable Polymer and Resistive Heating," *Journal of Composite Materials*, vol. 42, no. 26, pp. 2869–2881, Dec. 2008.

[30]   F. Ghezzo, D. R. Smith, T. N. Starr, T. Perram, a. F. Starr, T. K. Darlington, R. K. Baldwin, and S. J. Oldenburg, "Development and Characterization of Healable Carbon Fiber Composites with a Reversibly Cross Linked Polymer," *Journal of Composite Materials*, vol. 44, no. 13, pp. 1587–1603, Mar. 2010.

[31]   A. M. Peterson, R. E. Jensen, and G. R. Palmese, "Thermoreversible and remendable glass–polymer interface for fiber-reinforced composites," *Composites Science and Technology*, vol. 71, no. 5, pp. 586–592, Mar. 2011.

[32]   http://en.wikipedia.org/wiki/Ninhydrin

[33]   http://en.wikipedia.org/wiki/Infrared_spectroscopy_correlation_table

CHAPTER THREE

Development of Healable Composite Formulated Using Commercially Available Poly Furfuryl Alcohol and Bismaleimide

3.1 Introduction

A self-healing material is a type of smart material that has the ability to repair damage by itself and recover mechanical properties.[1] The idea comes from biological systems that are called "self-healing", for example the human body's ability to recover from various kinds of wounds or damage resulting from internal or external causes.[2-5] Over several decades, self-healing materials have been extensively studied and can go beyond biological aspects. Most of the self-healing materials or healable materials are based on functional or smart polymers with healable properties. These materials and properties have been adapted to support technologies such as satellite applications, wind blades and automobiles.[1]

A healable property is also important in terms of both composite life span and mechanical properties. Having a characteristic that repairs micro cracks can delay structural failure and also reduce effects on the life cycle from delamination between reinforced fiber and matrix resin. Most micro cracks are generated by this type of inter-laminar failure from internal and external forces.[3, 6, 7] Micro cracks can be propagated by further forces when fatigued or from elevated temperature, resulting in a reduced life cycle and composite failure. Numerous papers have been published looking at and seeking a healable process in composites to resolve various issues.[3, 8-12]

As described in chapter 2, 2MEP4F, a thermally-healable resin has been developed and become a strong candidate as a healable resin in composites by showing excellent efficiency in terms of healing,[12, 13] 2MEP4F has already been chosen as a candidate to composite with carbon fibers or glass fibers as structural material in aerospace application as described in our previous work. However, the chemical synthesizing process and sensitivity of the furan group[14, 15] are considered critical problems that need to be resolved prior to application as a commercial composite resin. Additionally, its mechanical strength is lower than current commercially-available epoxy resins. Although thermally re-mendable epoxy compounds have been studied and developed by many researchers, including Tian et al.[15-17], who introduced one with excellent healing properties, it still remains a challenge to resolve various issues as this group also uses a two-step route synthesizing method for furan derivatives[18-20] to avoid unwanted side products. Therefore, the purpose of the research in this chapter is to develop a functional polymer composite that is thermally healable and also with mechanical properties that are as strong as epoxy if possible. Poly furfuryl alcohol (PFA), also called furan resin, is well-known as a cross-linkable thermoset material, and the furan group in furan resin is relatively stable in comparison with 4F or other furan derivative monomers. 1,1'-(Methylenedi-4,1-phenylene) bismaleimide (MDPB)[21] includes two maleimide groups which we used as reagent in previous glass fiber functionalization work are also cross-linkable thermoset and commercially available. Based on our experimental data, a PFA and MDPB mixture shows a thermally healable property, but the mechanical properties were not strong enough compared to 2MEP4F. In order to improve the mechanical properties, a blend of thermally remendable resin (PFA and MDPB) and commercially-

available epoxy was studied. The healing and mechanical properties were studied by controlling the ratio of PFA and MDPB. The details of making healable polymers based of the above mentioned multi-furan and multi maleimide materials and epoxy to achieve comparable healing ability and mechanical strength with 2MEP4F will be described in this chapter.

3.2 Experiments

3.2.1. Materials

Poly (furfuryl alcohol) resin (PFA), EDR 176, and Epon 828 were kindly provided by Dynachem, Huntsman, and Miller-Stephenson Chemical Company, respectively. Epon 828 was a liquid diglycidyl ether of bisphenol A (DGEBA) epoxy resin with an equivalent of 185 - 192 g/eq. 1,1'-(Methylenedi-4,1-phenylene) bismaleimide (MDPB) that was purchased from Sigma Aldrich. These chemicals were used without further purification. The chemical structures of these materials are shown in Figure 3.1.

(a) PFA

(b) MDPB

(c) Diglycidal Ether of Bisphenol A Resin
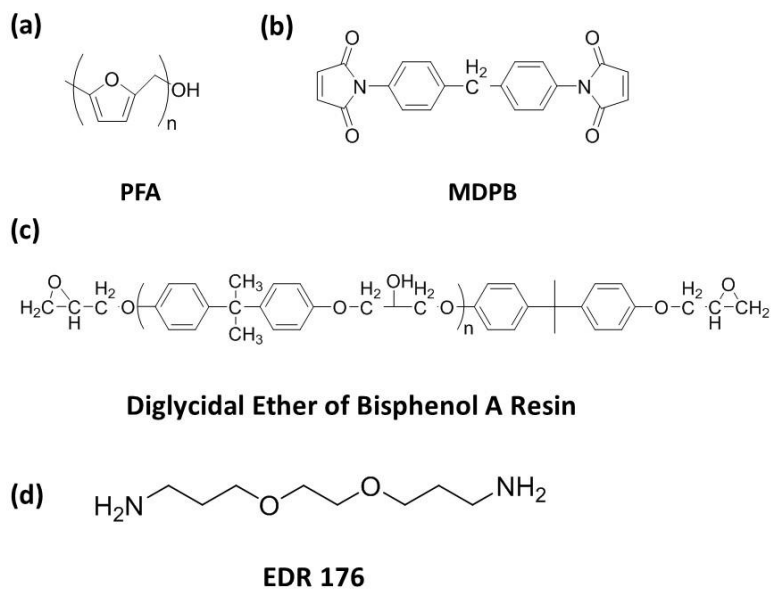
(d) EDR 176

Figure 3.1 Chemical structures of (a) poly(furfuryl alcohol), PFA (b) MDPB, (c) molecular structure of Epon 828, and (d) EDR 176.

3.2.2. Composite samples fabrication

Commercially-available and thermally-healable polymers were produced by mixing PFA and MDPB. In order to calculate the correct stoichiometric ratio of the mixture, it was assumed that a repeating unit of PFA was a furfural unit as shown in Figure 3.1 (a). The resins used in this research were prepared by hybridization of a healable resin and conventional epoxy resin mixed with hardener. A detailed recipe of hybridization and resin ID are listed in Table 3.1.

PFA of 2 g, for example, was mixed with 2.24 g of MDPB for FM41 resin with a mole ratio of PFA(4) and MDPB(1), then the epoxy resin, which was a mixture of 5 g of Epon 828 and 1.19 g of EDR 176 was prepared per the stoichiometric ratio. Two mixtures that consisted of the healable mixtures and epoxy mixtures were stirred vigorously by a magnetic bar on a stirring plate. FM81 (PFA: 2 g and MDPB: 1.12 g) and FM161 (PFA: 2 g and MDPB: 0.56 g) resins were prepared by the same method. The final resins for the healing test were prepared with a mixture of a healable resin and epoxy resin with the same volume ratio (1:1). The resins were also stirred using a magnetic stirring plate with vigorous stirring in order to obtain well-mixed final resins with hybridized properties.

The fabrication of the composite panel was conducted by a lay-up, drop casting and curing process. The dimension of prepared panel was 40 mm in length and 40 mm in width. After a [0/0/90/90/0/0] lay-up sequence of GA045 unidirectional carbon fiber reinforcement (purchased from Fiberglass Supply), the mixture of matrix polymers was

poured on to the fibers and allowed enough time for wetting. After then, the polymer composites were cured at 115 $^\circ$C for 15 hours followed by a gradually cooling to room temperature as we did with 2MEP4F composite samples previously.

Table 3.1: Experimental recipe and panel ID of thermally-healable samples.

Panel ID	PFA	MDPB	Epon828	EDR176	Note
FM41E1	4	1			mole ratio
	1		1		volume ratio
FM81E1	8	1			mole ratio
	1		1		volume ratio
FM161E1	16	1			mole ratio
	1		1		volume ratio

3.2.3 Characterization

Fourier Transform Infrared spectroscopy (FT-IR) was performed using a FT-IR model 420, JASCO. The spectra were recorded using 128 scans at a resolution of 4 cm^{-1} in a range of between 4000 and 600 cm^{-1}. The FT-IR samples were prepared using a KBr pellet with a press machine (for the solid sample) and using sodium chloride plates dissolved in dichloromethane (for the liquid sample).

Healing properties were tracked through X-ray micro-tomography (micro-CT) in a Desktop Micro CT-system (Model: Skyscan 1172, Micro Photonics Inc.), operated at a medium resolution mode. The X-ray source was powered at 40 KV with a current of 250 µA without a filter. Each sample was projected with a 0.4° rotation step between 0.1° and 180°. The reconstruction was obtained from more than 400 individual X-ray images and generated cross-sectional images using Skyscan-NRecon Software. The illustration of principles for generating reconstructed images is shown in Figure 3.2.

The crack generated by the SBS test was not easy to detect by micro CT because of a mixture of voids and cracks at several micron sizes. The crack of the samples for micro CT were prepared by fixing one side of the sample, then slowly bending the other side of the sample until a crack was generated which was observable with the naked eye.
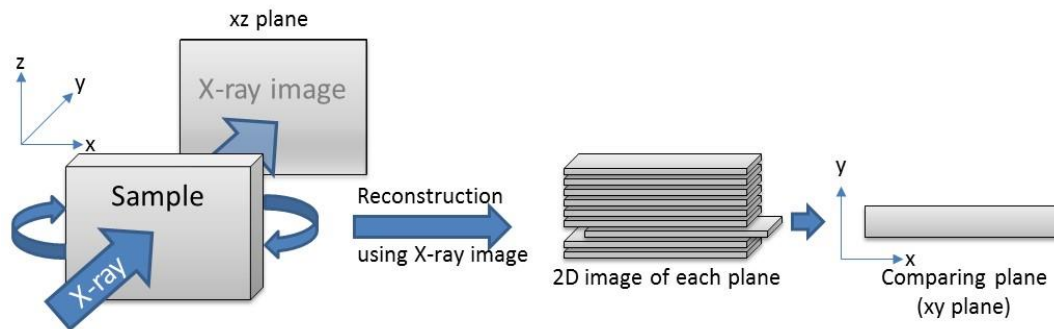
Figure 3.2: Principles for generating reconstructed images from x-ray scanned images (micro CT).

Short-beam shear strength was measured by using a universal test machine (Model: 4411, Instron) with a three-point bending mode and the test was conducted and calculated in accordance with ASTM D2344. The span used for the test was 20 mm and the cross-head speed was 0.5 mm/min. At least three samples were tested to obtain one repeatable and valid data set.

3.2.4 Healing test

All of the samples were healed while using the compressive healing fixture as shown in Figure 3.3. The applied healing pressure was controlled by the number of rotations of the screws. The applied pressure was adjusted by approximately 140 KPa.[22]
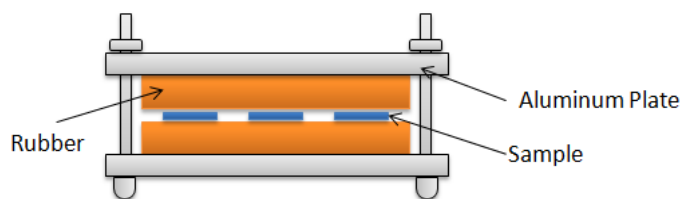
Figure 3.3: Schematic illustration of compressive healing fixture.

Healing and its efficiencies were explored in the following steps:

Step 1: Short beam test

Step 2: Pressing: tested samples were loaded into a compressive fixture with adjusted pressure

Step 3: Healing: increasing temperature up to 115 $^{\circ}$C for 15 hours

Step 4: Cooling down naturally to room temperature in the oven.

3.3 Results and Discussion

3.3.1 FTIR spectrum analysis

The FT-IR results of (1) PFA, (2) MDPB, (3) cured polymer of PFA and MDPB are shown in Figure 3.4. The reaction condition was chosen as 15 hours at 115°C following our previous condition. The evidence peak of DA adduction was shown at 1776 cm^{-1}[15, 17, 23] from (3) compared to (1) PFA and (2) MDPB. This indicates that the reaction between the furan group in PFA and bismaleimide group in MDPB occurred successfully at cured temperature 115°C.[22, 24]
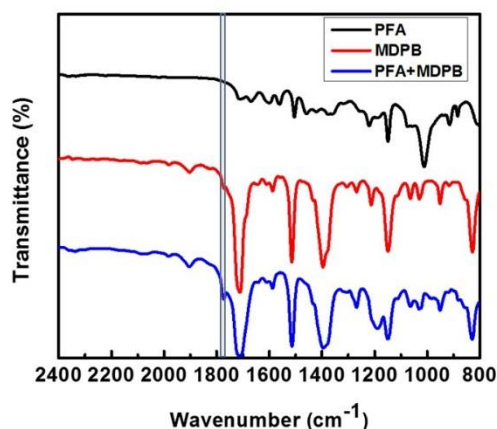
Figure 3.4: FT-IR spectrum of (1) PFA, (2) MDPB, and (3) PFA and MDPB mixture cured at 115°C for 15 hrs.

3.3.2 Micro CT characterization for only polymers healing ability

To characterize the healing ability of the new developed polymers composed from PFA, MDPB and epoxy, we checked the formed cracks and also the healed cracks with X-ray micro-tomography and the images were shown in Figure 3.5 for sample FM81E1 and in Figure 3.6 for sample FM161E1. For the images of sample FM81E1 resin, it showed that the crack generated in the middle of the resin disappeared after the healing process. Similarly as for sample FM161E1, the crack that also generated by the three-point bending fixture was clearly observed in the micro CT images. After the healing process, the crack was not observed in the micro CT image and only a small crack remained in the center of the sample. In the resin healing test, only a minimum weight was applied for the healing process in order to test the healing process, and thus the crack did not heal completely. Based on X-ray images and reconstructed images, the healing reaction occurred not only on the surface, but also inside of the samples. Overall, the resins

41

blended with PFA and MDPB in epoxy resin have a thermally-healable property similar to 2MEP4F but higher mechanical strength compared with 2MEP4F.
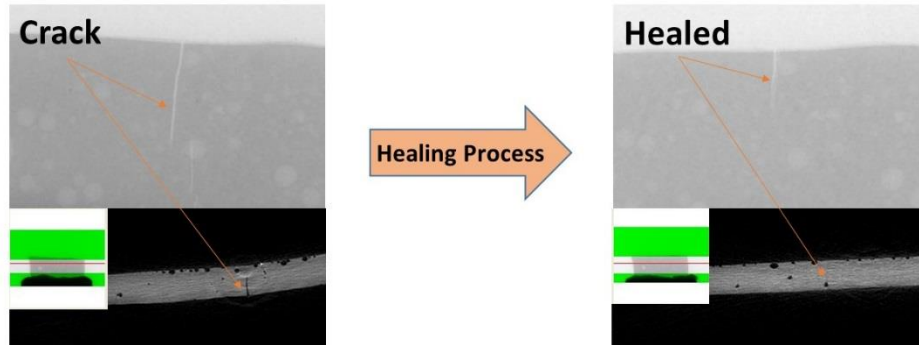
Figure 3.5 X-ray images (top grays images) and reconstructed images (bottom black background images) of FM81E1 shown the crack before and after the healing process. The images on the black background indicate the reconstructed features of the samples. The gray area and green boarder on the inserted image are the selected and unselected area for reconstruction of the sample, respectively. The red line on the inserted image indicates a reconstructed XY area.
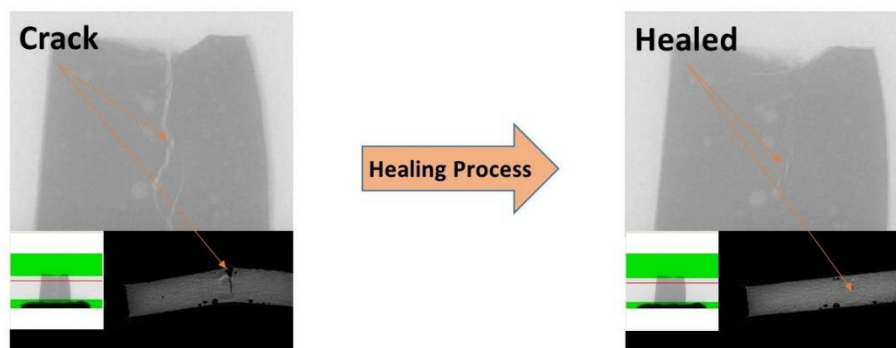
Figure 3.6 X-ray images (top grays images) and reconstructed images (bottom black background images) of FM161E1 shown the crack before and after the healing process. The images on the black background indicate the reconstructed features of the samples. The gray area and green boarder on the inserted image are the selected and unselected

area for reconstruction of the sample, respectively. The red line on the inserted image indicates a reconstructed XY area.

As we have proved the healing ability of the PFA/MDPB/Epoxy resins, we made composite samples with carbon fibers sheet as we did previously with 2MEP4F healable polymer matrix. The fabrication method and recipe were listed in experimental section. The repeatable healing was also traced through micro-CT images as shown in Figure 3.7, 3.8 and 3.9 for FM41E1, FM81E1 and FM161E1 coupons respectively.
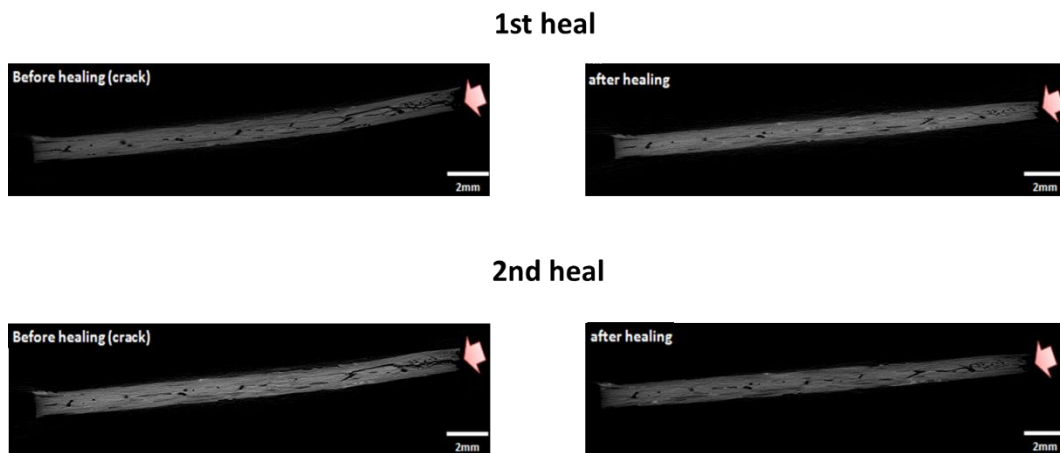
Figure 3.7 Reconstructed images of FM41E1 samples before and after healing with the first cycle (top) and second (bottom) healing cycle. The red arrows indicate the position of the generated and healed crack in each healing cycle.

Figure 3.7 shows the reconstructed images of before and after the healing of the FM41E1 panel in terms of healing cycles. As described in experimental section, the crack generated by holding one side using a fixture and then bending the other side as shown in Figure 3.7 (top, crack) and indicated by an arrow, where the crack was propagated to the interlaminar layer perpendicular to the reinforcement. After healing via the healing process, the crack was successfully repaired by the process and only a small crack was

detected as shown in Figure 3.7 (top, after healing). A 2nd healing cycle was also tested and reconstructed by micro CT in Figure 3.7 bottom, which indicates individually the before and after of the 2nd healing cycle. The 2nd crack was also repaired, but in the case of the FM41E1 panel the crack still remained inside the panel. This indicates that healing efficiency may have decreased with the increase in healing cycles of the FM41E1 panel. Healing efficiency will be discussed further in the mechanical property section.
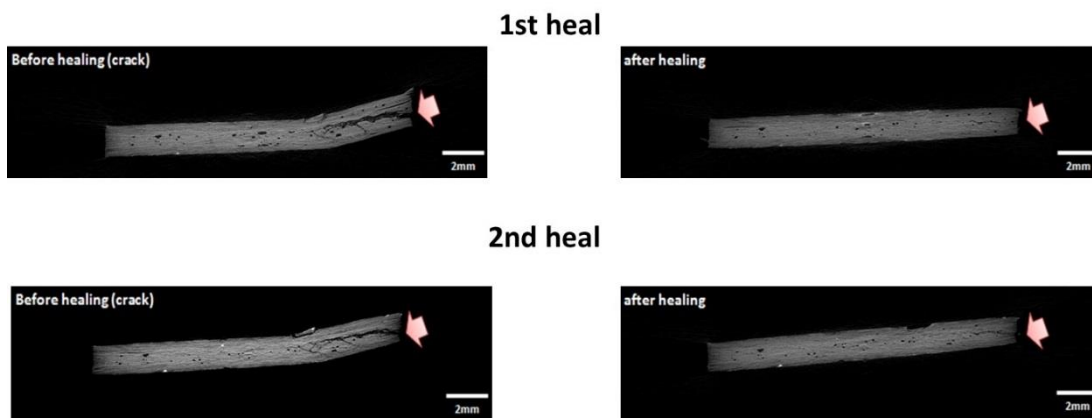
Figure 3.8 Reconstructed images of FM81E1 samples before and after healing with the first cycle (top) and second (bottom) healing cycle. The red arrows indicate the position of the generated and healed crack in each healing cycle.

As shown in Figure 3.8, the FM81E1 panel was also tested for healing property in terms of healing cycles. Figure 3.8 (top) indicate the before and after of the 1st healing cycle for the FM81E1 panel. As seen, the crack that was manually generated is observable and the crack existed from the end of the panel to the center. The size of crack was around 5 mm in length and 0.5 mm in thickness. After the healing process, the crack completely disappeared in the panel as indicated by the red arrow. In comparison to the FM41E1 panel, the healing efficiency was improved. For the 2nd healing cycle, the crack was re-

generated and healed by the same healing process as shown in Figure 3.8 (bottom). After healing, the crack was almost completely repaired, but a micro-sized crack that still remained might affect the maximum SBS strength.
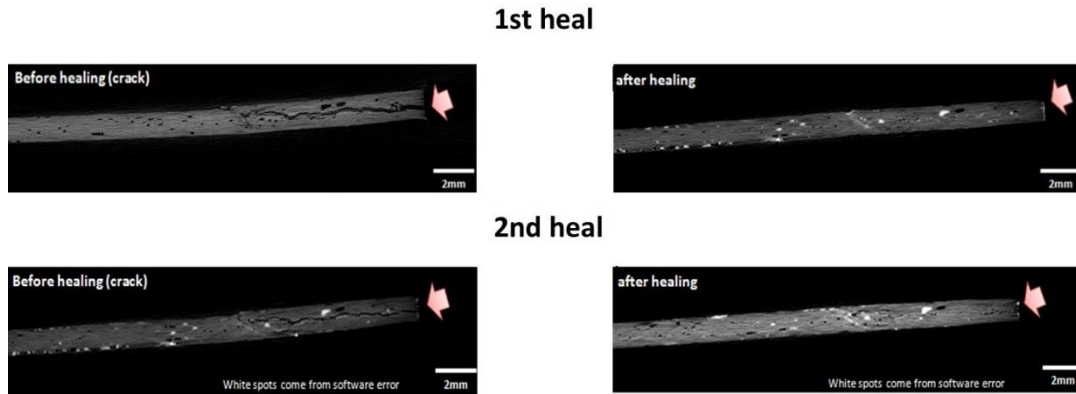
Figure 3.9 Reconstructed images of FM161E1 samples before and after healing with the first cycle (top) and second (bottom) healing cycle. The red arrows indicate the position of the generated and healed crack in each healing cycle.

The FM161E1 panel, which was produced with relatively less resin, was also examined by micro CT, and the x-ray images were reconstructed in order to investigate the healing properties. As can be seen in Figure 3.9 (top), the before and after of the 1st healing images were imaged and the crack from the end of the panel to the center was clearly detected and indicated by the red arrow in Figure 3.9. After the healing process, the crack clearly disappeared. In the same way, a 2nd healing cycle was conducted and the foundation of the re-generated crack also completely disappeared. In a previous reconstructed image of the FM41E1 and FM81E1 panels, for the 2nd healing cycle, the

re-generated cracks were not completely repaired which indicates an incomplete repair. A more accurate analysis in terms of mechanical property will be described in the next parts.

3.3.3 Short-beam shear strength characterization

The short beam shear (SBS) test introduces a facile and repeatable method for understanding the apparent inter-laminar shear strength of composite materials and the result reveal strength-displacement curves that show inter-laminar failure in the samples.[25-27] In our research here, SBS tests were conducted to our composite samples and were used to evaluate the shear strength and healing efficiency. In Figure 3.10, 3.11 and 3.12, shear strength-displacement curves for virgin samples, after healing samples of FM41E1, FM81E1 and FM161E1 were given together with 2MEP4F healable polymer and epoxy samples.
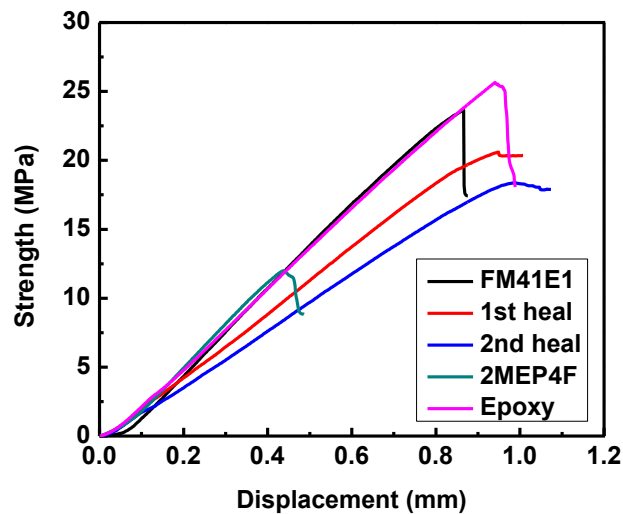
Figure 3.10 Short beam shear strength vs displacement curves of FM41E1 samples.

The stiffness of the composite is defined by the rigidity of a composite and formulated by the ratio of force and displacement.[28] The stiffness can also be judged as the slope of

46

stress-displacement curves. In Figure 3.10, the stiffness decreased with increasing healing cycles. The stiffness in a composite is affected by damage on reinforcement fibers or on the matrix resin. This means that the cross-linked epoxy bond or reinforced carbon fibers were damaged during SBS test. As discussed in the previous section, the flexibility of resin decreased with an increasing MDPB ratio because of the brittleness of MDPB caused by the phenyl group in the chemical structure.

When a micro crack is generated by an external force in the panel body, some of the cross-linked epoxy bonds or reinforced carbon fibers can be broken. This damage cannot be repaired by the healing process, so the results are reflected in the next healing cycle with decreasing stiffness. In addition, the maximum load decreased with increasing healing cycles. This also indicated that the interfacial delamination induced by external force and the bonds broken in the carbon fibers and in unrepairable epoxy chemical bonds.
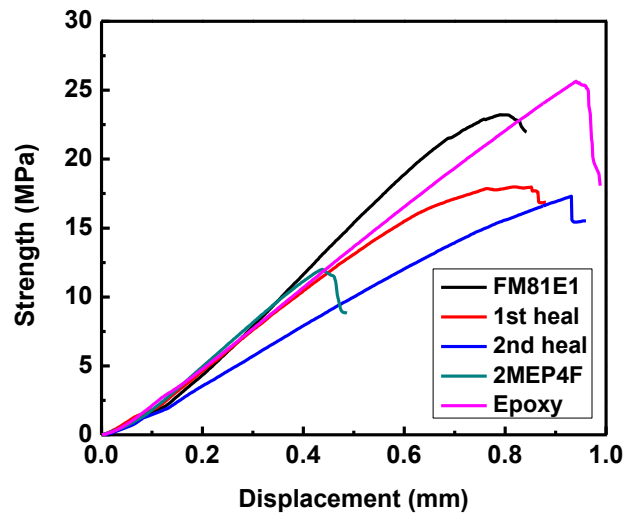
Figure 3.11 Short beam shear strength vs displacement curves of FM81E1 samples.

In Figure 3.11, the stiffness of the FM81E1 panel was higher than that of epoxy and 2MEP4F panel until the 1st healing cycle, but the values decreased with increasing healing cycles. As seen in this data, the FM81E1 combination shows some hybrid effects and the stiffness values were much higher than the conventional epoxy panel. The maximum load of the FM81E1 panel also decreased with additional healing cycles due to damage of reinforcements or cross-linked epoxy resin due to brittleness.

A sample of four times low MDPB was mixed in the FM161E1 panel in order to understand the PFA effect on the healable property and we found that the stiffness of the panel followed a very similar trend to the epoxy and 2MEP4F sample. As shown in Figure 3.12, the stiffness decreased with increasing healing cycles, similarly as in previous samples, but the maximum load of the panel maintained its original value. This indicates that in the case of FM161E1 resin, the crack generated by the external force was repaired completely by our healing process.
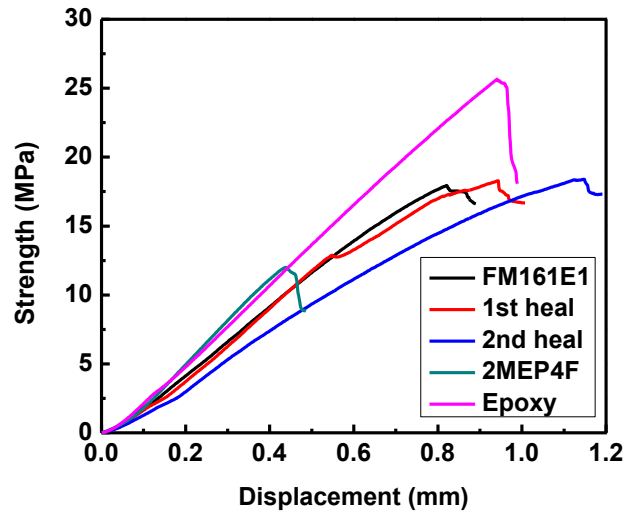
Figure 3.12 Short beam shear strength vs displacement curves of FM161E1 samples.

Based on our expectations, FM161E1 would not have a better healing property than the other resins. However, the plot of the load and displacement of FM161E1 panel shows around a 100% recovery from the virgin panel. This means the less MDPB is more suitable amount for PFA and MDPB copolymerization. The repeating furan groups on the PFA main chain cannot have full reactivity with MDPB due to the high steric hindrance. Therefore, if we have more MDPB and less PFA in composite system, it will lead to over amount of MDPB without reacted with PFA in the composite. Because the MDPB can self-polymerized, the polymerized MDPB will increase the brittleness of the whole composite and decrease the healing ability.

The maximum short-beam shear (SBS) strength given in this work was calculated by the following equation:[27]

$$F(SBS) = 0.75 \times \frac{P}{w \times t}$$

P is applied load, w and t are width and thickness of the sample, respectively. The healing efficiency E of the short beam shear strength was calculated by following equation in each healing cycle.

$$E = \frac{F_h}{F_v} \times 100\%$$

Fv is short beam strength of a virgin sample and Fh is short beam strength of a healed sample. All measured and calculated results are listed in Table 3.2.

Table 3.2 SBS strength and healing efficiencies of each sample with virgin, 1st, and 2nd healing cycles.

Sample	Virgin		1st healed		2nd healed	
	SBS (MPa)	Efficiency (%)	SBS (MPa)	Efficiency (%)	SBS (MPa)	Efficiency (%)
FM41E1	24.13	N/A	19.33	79.33	16.09	66.83
FM81E1	21.96	N/A	16.59	75.83	14.07	62.40
FM161E1	14.49	N/A	16.98	119.7	15.43	107.1
2MEP4F	12.28	N/A	15.32	122.6	14.89	119.5
Epoxy	26.38	N/A	N/A	N/A	N/A	N/A

For the virgin samples, the SBS strength of epoxy is the strongest SBS strength value among the samples and the SBS strength decreases with a decreasing proportion of bismaleimide in the resin as listed in Table 3.2. This means the amount of bismaleimide in the sample affects both the healing ability and also the SBS strength. Less amount of bismaleimide is a suitable ratio for D-A reaction occurring and good for healing processing. On the other hand, more amount of bismaleimide can give higher strength of the composite. Basically, the stoichiometric ratio for complete DA adduction is reflected in FM21, but the viscosity of the resin is too high to do a hand lay-up process, even if there is a high temperature of around 80°C. Thus, the ratio of FM21 was not listed in this work. In comparison to FM41E1 and FM161E1, the FM41E1 resin has higher SBS strength but the healing ability is worse than that of FM161E1. With a 100% healing efficiency, FM161E1 sample also owned 2.2MPa higher of a maximum SBS strength than that of 2MEP4F, which means the FM161E1 sample has high enough strength and prefect healing ability for our structural composite application. The epoxy group plays an important role in improving interlaminar shear strength because most commercially-available carbon fibers have been treated with a surface modification agent to improve the interfacial strength between the carbon fibers and epoxy resin.

3.4 Conclusion and Future Work

A thermally-healable and easily synthesized healable polymer composite was investigated. The polymer composes with polymer of PFA and MDPB and epoxy resin. Three types of composite with various PFA to MDPB ratio were detailed studied. The composite was evaluated through micro CT images and short beam shear strength tests. To increasing the healing ability, more PFA and less MDPB should be included in the composite. Compared the FM41E1 and FM161E1 samples, it is clear that FM161E1 with less amount of MDPB and more PFA has the highest healing efficiency which was over 100%. The healing ability of FM161E1 is the same as our previously healable 2MEP4F. The short beam shear strength of FM161E1 is higher than that of 2MEP4F. Therefore, we have successfully developed the composite healable polymer system FM161E1/epoxy with same healing ability and strength. The newly developed composite polymer has much lower cost and short synthesis procedure which is suitable candidate for further structural materials application in aerospace industry. For the future work, the ratio of PFA and MDPB healable polymers to epoxy polymers need to be systemically studied to find out the optima value for higher SBS strength with high healing efficiency. Furthermore, multiple times healing possibility need to be investigated for this composite system to prove its potential in real application.

Reference:

[1]   S. v. d. Zwaag, "Self healing materials an alternative approach to 20 centuries of materials science," Dordrecht, The Netherlands: Springer, 2007.

[2]   S. H. Cho, H. M. Andersson, S. R. White, N. R. Sottos, and P. V. Braun, "Polydimethylsiloxane-based self-healing materials," Advanced Materials, vol. 18, pp. 997, Apr 2006.

[3]   M. R. Kessler, N. R. Sottos, and S. R. White, "Self-healing structural composite materials," Composites Part a-Applied Science and Manufacturing, vol. 34, pp. 743-753, 2003.

[4]   K. S. Toohey, N. R. Sottos, J. A. Lewis, J. S. Moore, and S. R. White, "Self-healing materials with microvascular networks," Nature Materials, vol. 6, pp. 581-585, Aug 2007.

[5]   S. R. White, N. R. Sottos, P. H. Geubelle, J. S. Moore, M. R. Kessler, S. R. Sriram, E. N. Brown, and S. Viswanathan, "Autonomic healing of polymer composites," Nature, vol. 409, pp. 794-797, Feb 2001.

[6]   R. Talreja, "Damage Development in composites – mechanisms and modeling," Journal of Strain Analysis for Engineering Design, vol. 24, pp. 215-222, Oct 1989.

[7]   E. K. Gamstedt and R. Talreja, "Fatigue damage mechanisms in unidirectional carbon-fibre-reinforced plastics," Journal of Materials Science, vol. 34, pp. 2535-2546, Jun 1999.

[8]   C. Dry, "Procedures developed for self-repair of polymer matrix composite materials," Composite Structures, vol. 35, pp. 263-269, Jul 1996.

[9]   K. Jud and H. H. Kausch, "Load-transfer through chain molecules after interpenetration at interfaces," Polymer Bulletin, vol. 1, pp. 697-707, 1979.

[10]   P. Cordier, F. Tournilhac, C. Soulie-Ziakovic, and L. Leibler, "Self-healing and thermoreversible rubber from supramolecular assembly," Nature, vol. 451, pp. 977-980, Feb 2008.

[11]   X. F. Luo, R. Q. Ou, D. E. Eberly, A. Singhal, W. Viratyaporn, and P. T. Mather, "A Thermoplastic/Thermoset Blend Exhibiting Thermal Mending and Reversible Adhesion," Acs Applied Materials & Interfaces, vol. 1, pp. 612-620, Mar 2009.

[12]   X. X. Chen, F. Wudl, A. K. Mal, H. B. Shen, and S. R. Nutt, "New thermally remendable highly cross-linked polymeric materials," Macromolecules, vol. 36, pp. 1802-1807, Mar 2003.

[13]   X. X. Chen, M. A. Dam, K. Ono, A. Mal, H. B. Shen, S. R. Nutt, K. Sheran, and F. Wudl, "A thermally re-mendable cross-linked polymeric material," Science, vol. 295, pp. 1698-1702, Mar 2002.

[14]   Y. X. Hu, L. J. Qiao, Y. S. Qin, X. J. Zhao, X. S. Chen, X. H. Wang, and F. S. Wang, "Synthesis and Stabilization of Novel Aliphatic Polycarbonate from Renewable Resource," Macromolecules, vol. 42, pp. 9251-9254, Dec 2009.

[15]   Q. Tian, M. Z. Rong, M. Q. Zhang, and Y. C. Yuan, "Optimization of thermal remendability of epoxy via blending," Polymer, vol. 51, pp. 1779-1785, Apr 2010.

[16]   Q. Tian, Y. C. Yuan, M. Z. Rong, and M. Q. Zhang, "A thermally remendable epoxy resin," Journal of Materials Chemistry, vol. 19, pp. 1289-1296, 2009.

[17]   Q. A. Tian, M. Z. Rong, M. Q. Zhang, and Y. C. Yuan, "Synthesis and characterization of epoxy with improved thermal remendability based on Diels-Alder reaction," Polymer International, vol. 59, pp. 1339-1345, Oct 2010.

[18]   A. Gandini and M. N. Belgacem, "Furans in polymer chemistry," Progress in Polymer Science, vol. 22, pp. 1203-1379, 1997.

[19]   M. Choura, N. M. Belgacem, and A. Gandini, "Acid-catalyzed polycondensation of furfuryl alcohol: Mechanisms of chromophore formation and cross-linking," Macromolecules, vol. 29, pp. 3839-3850, May 1996.

[20]   R. Gonzalez, R. Martinez, and P. Ortiz, "Polymerization of furfuryl alcohol with trifluoroacetic acid – the influence of experimental conditions," Macromolecular Chemistry and Physics, vol. 193, pp. 1-9, Jan 1992.

[21]   M. F. Grenier-Loustalot and L. da Cunha, "Thermostable polymers: spectroscopies and thermal studies of bismaleimide systems in the solid state," High Performance Polymers, vol. 10, pp. 285-308, Sep 1998.

[22]   J. Riendeau, "Self-Healing Fiber Reinforced Polymer Composites for Structural Applications," Ph.D. thesis, Mechanical Engineering, UNIVERSITY OF CALIFORNIA at Los Angeles, 2011.

[23]   Y. Imai, H. Itoh, K. Naka, and Y. Chujo, "Thermally reversible IPN organic-inorganic polymer hybrids utilizing the Diels-Alder reaction," Macromolecules, vol. 33, pp. 4343-4346, Jun 2000.

[24]   J. S. Park, T. Darlington, A. F. Starr, K. Takahashi, J. Riendeau, and H. T. Hahn, "Multiple healing effect of thermally activated self-healing composites based on Diels-Alder reaction," Composites Science and Technology, vol. 70, pp. 2154-2159, Dec 2010.

[25]   J. M. Whitney and C. E. Browning, "On short-beam shear test for composite-materials," Experimental Mechanics, vol. 25, pp. 294-300, 1985.

[26]   E. Sideridis and G. A. Papadopoulos, "Short-beam and three-point-bending tests for the study of shear and flexural properties in unidirectional-fiber-reinforced epoxy composites," Journal of Applied Polymer Science, vol. 93, pp. 63-74, Jul 2004.

[27]   "Apparent horizontal shear strength of reinforced plastics by short-beam method," in American Society for Testing Materials, 1965, pp. D2344-65T.

[28]   Available: http://en.wikipedia.org/wiki/Stiffness

CHAPTER FOUR

A Healable, Semi-transparent Silver Nanowire-Polymer Composite Conductor

4.1 Introduction

The failure of electronic devices due to mechanical fracture limits the lifetime and reliability of the devices and leads to the increasing amount of electronic wastes. Healable electronics have been explored that could help alleviate these problems.[1-3] So far, healable electronic conductors, a key component in healable electronics, have been reported in several publications.[4-10] In one approach, an organometallic polymer complex formed between N-heterocyclic carbenes (NHCs) and transition metals has been used as a healable conductor with a (bulk) conductivity on the order of 10^{-3} S/cm.[3] The structure of the complex and its dynamic equilibrium state changes are shown in Figure 4.1.
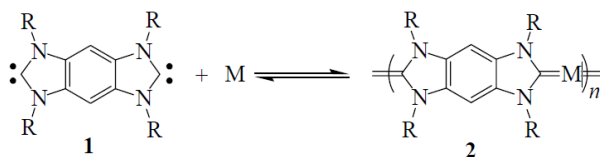
Figure 4.1 A dynamic equilibrium between a monomer species (left) and a organometallic polymer (right) that is controlled via an external stimulus such as heat. (Reproduced from [3])

This organometallic polymer complex has the conductivity on the order of 10^{-3}S/cm. As shown in Figure 4.1, the monomer 1 can form conductive complex polymer with metal M reversibly with tunable equilibrium constants. Therefore, this polymer complex is self-healable upon heating with certain conductivity. This complex organometallic is regarded

as the first healable electronic conductor materials. While its conductivity is recoverable upon heating at 200 °C, the low conductivity of this material would limit its application in electronic devices.

To further develop the healable electronic conductor, microencapsulated eutectic gallium-indium liquid metal has been employed to recover the broken conductive pathway in a polymer matrix.[11] Eutectic Ga-In alloy is chosen as the healing agent due to its low melting point (16 °C), its relatively high conductivity of 3.40×10^4 S/cm, and its previously demonstrated ability to form conformal electrodes. Liquid Ga–In was encapsulated in a polymeric urea-formaldehyde (UF) shell wall. The small capsules were patterned in a conductive Au layers to form a composite conductive pathway. Upon mechanical damage, in such a broken circuit, healing was accomplished by the release and transport of a microencapsulated liquid Ga-In to the site of damage. Figure 4.2 is the scheme of the electrode configuration and the healing process. Such a healable system can self-heal very quickly but for only one time. Repeating healing ability is necessary in most of applications therefore various more efforts are inspired and devoted.
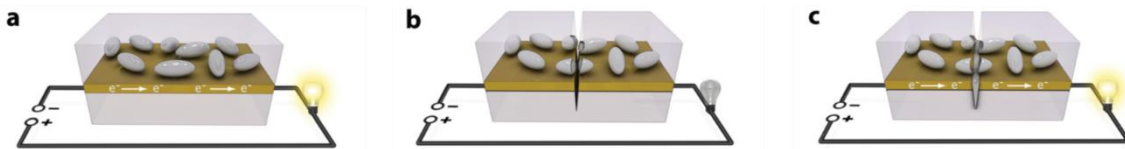
Figure 4.2 Autonomic conductivity restoration concept in an electronic device. a) The self-healing circuit consists of microencapsulated liquid metal dispersed in a dielectric material and deposited on a conductive Au layer. b) Crack damage breaks the conductive pathway, interrupting electron transport and simultaneously rupturing the capsules. c)

The liquid metal flows from the capsules to the area of damage, restoring a conductive pathway. (Reproduced from [11])

Water triggered healable polyelectrolyte multilayer film has also been reported for healable electrode application. A thick layer of silver nanowires was coated on top of healable polyelectrolyte multilayer film to form a conductive pathway.[12] In Figure 4.3, it revealed the structure of such a healable electrode together with illustration of its healing process. When there was a crack on the electrode, drops of water added into the cracks accomplished the healing of both the polyelectrolyte multilayer substrate and the conductive AgNWs network. However, the use of water in electronic systems could cause shorting, water leakage, and loss of water from evaporation, and thus loss of healing property.
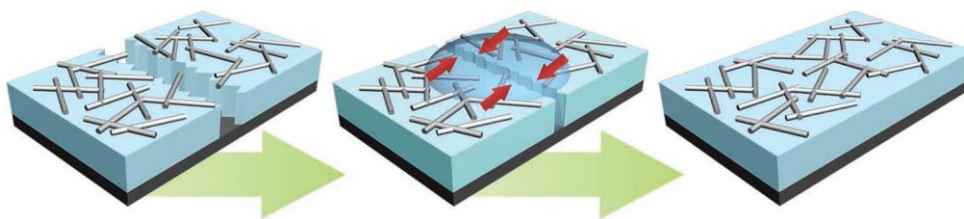
Figure 4.3 Schematic representation of water-enabled healing of electrical conductivity of an AgNWs/ polyelectrolyte multilayer film. (Reproduced from [12])

To further improve the healable electronic conductors, a supra-molecular polymeric hydrogen-bonding network containing homogeneously dispersed nickel micro-particles has been demonstrated as self-healable skin.[13] The composite consist a supramolecular polymeric hydrogen-bonding network with a glass transition temperature Tg below room temperature and chemically compatible micro-nickel (μNi) particles with nanoscale surface features as shown in Figure 4.4. The supramolecular polymeric hydrogen-

bonding network provides the self-healing function via the large number of weak hydrogen bonds, which break preferentially (instead of the stronger covalent bonds) during a mechanical damage event. These 'broken' hydrogen bonds have been shown to dynamically associate and dissociate at room temperature to provide a passive healing mechanism at the fracture surface. The addition of micro-nickel particles up to 31% volume percentage enables the high conductivity of 40 S/cm. Although the self-healable skin can recover both structural and electrical damages repeatedly and effectively, such a self-healable skin is not visually transparent. Thus, a repeatable healable and highly conductive transparent conductor is still urgently needed for the application of optoelectronic devices.
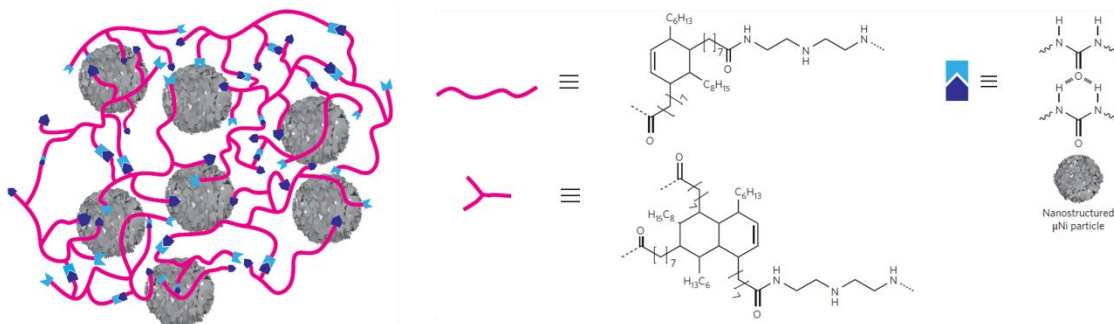
Figure 4.4 Illustration of network of the polymer and μNi particles composite. Pink lines, linear and branched polymers form the randomly branched network; blue and purple shapes, urea groups at the ends of the branched polymers form the primary hydrogen bonds between the polymer chains; grey dots, micro-nickel particles. (Reproduced from [13])

In general, to fabricate healable conductors, conductive or semi-conductive materials are dispersed into a healable polymer or thermoplastic elastomer matrix. This polymer matrix

plays a critical role on the performance of the healable conductor. Polymers based on reversible Diels-Alder (D-A) reaction have been investigated for multiple healing.[14, 15] This category of healable polymers has been investigated for applications that require high structural strength[16-19] and re-mendability in previous chapters of this dissertation. The D-A polymers are also transparent, making them a suitable candidate as the matrix for healable transparent conductors.

Transparent conductor is another subject of extensive current interest on its own: indium tin oxide (ITO), the widely used transparent conductor for a host of optoelectronic devices, has its share of drawbacks. A number of candidate materials have been investigated to replace ITO for mechanical flexibility and low cost. Silver nanowire (AgNW) stands out as a promising material to fabricate flexible and transparent conductors thanks to its high conductivity and large aspect ratio that enable the formation of a highly conductive percolation network with high transparency and mechanical compliance.[20-22] Moreover, silver nanowires can fuse at the intercrossing at relatively low temperature to further reduce the resistance of the conductive pathway. High-performance electronic devices thus have been successfully fabricated employing transparent electrodes based on AgNWs.[23-27] Therefore, a novel healable and transparent conductor is inspired by the combination of high conductive AgNWs with mechanically strong and transparent D-A polymers.

In this chapter, we summarized the synthesis of a semi-transparent composite conductor comprising a layer of AgNW percolation network inlaid in the surface layer of a D-A based healable polymer film. The semi-transparent composite conductor has a highly conductive surface with sheet resistance as low as 9.5 Ω/sq and shows very good

flexibility. The composite film is capable of both structural and electrical healing via heating. A cut crack can heal quickly and efficiently as the D-A polymer matrix reform to bring together the silver nanowires which re-forge to restore the percolation network. Furthermore, this healable semi-transparent conductor can be repeatedly cut and healed at the same location for multiple times without significant loss of surface conductivity.

4. 2 Experiments

4.2.1 Synthesis of healable polymer

For the synthesis of FGEEDR,[28] 4.93g furfuryl glycidyl ether (FGE, Sigma Aldrich) was heated up to 40 °C in glove box or under argon protection without addition of any solvent. Then 1.19 g Jeffamine EDR-176 from Huntsman was slowly added into the FGE dropwise, and the reaction mixture was stirred at 60 °C for 6 hours in an inert environment (either glove box or argon atmosphere). At the end of 6 hours, the crude product was eluded through silica gel column with methanol as eluent to give light yellowish color FGEEDR. The yield is 86%. NMR spectrum of the product is shown in result and discussion section.

4.2.2 Copolymerization of MDPB and FGEEDR

0.35 g MDPB was dissolved into 2.4 g cyclopentanone. After MDPB was fully dissolved, 0.38 g of FGEEDR was added into the solution, and the mixture was sonicated till a clear solution was obtained. The solution was cast on a glass slide. The liquid layer of the co-monomers after evaporation of solvent was copolymerized at 70 °C in a vacuum oven at 1 Torr for 5 hours.

4.2.3 Fabrication of transparent composite conductor

AgNWs were synthesized with an average diameter between 25-35 nm, and average length between 10-20 μm.[29] An AgNW dispersion was drop-cast on a pre-cleaned glass substrate to form conductive AgNW coatings. After drying, the AgNW thin layer was annealed to reduce the inter-nanowire resistance. Similar to the preparation of the neat MDPB-FGEEDR copolymer, a solution of MDPB and FGEEDR in cyclopentanone was drop-cast onto the AgNW coating on a glass (release) substrate. The liquid layer was subsequently copolymerized at 70 °C in vacuum oven for 5 hours. The resulting AgNW-copolymer composite film was peeled off from the release substrate.

4.2.4 Characterization

Transmittance spectra of composite samples were collected by Shimadzu UV-1700 spectrophotometer. Resistance measurements were performed using a Fluke 73III multimeter. Optical microscope images were taken on a TF Probe microspectrophotometer SP100MS. SEM surface and cross sectional micrographs were taken on an FEI Nova Nano SEM 230 scanning electron microscope operated at an accelerating voltage of 5 KV.

Stress-strain test: The tensile test was done using a TA RSA3 dynamic mechanical analyzer (DMA) at a strain rate of 0.1 mms^{-1}. Recovery of the mechanical strength of the polymer and composites is shown in result and discussion section also. The tensile stress-strain response of the following samples is shown:

1)   a fresh neat MDPB-FGEEDR copolymer (sample P1),

2)   a neat MDPB-FGEEDR copolymer thermally treated at 110 °C for 1 hour (sample P2)

3)   a neat MDPB-FGEEDR copolymer after blade cutting (sample P3)

4)   a neat MDPB-FGEEDR copolymer after blade cutting followed by healing for 1 hour at 110°C. (sample P4)

5)   a fresh AgNW-copolymer composite (Sample 1, named as sample C1),

6)   a AgNW-copolymer composite after thermally treatment at 110 °C for 1 hour (sample C2),

7)   an AgNW-copolymer composite after blade cutting (sample C3)

8)   an AgNW-copolymer composite after blade cutting followed by healing for 1 hour healing at 110 °C (sample C4).

4.3 Results and Discussion

4.3.1 Pure MDPB-FGEEDR polymer characterization

The D-A based healable polymer selected for the healable composite conductor is a copolymer network polymerized from two monomers whose chemical structures are shown in Figure 4.5a. The monomer with two maleimide groups, 1, 1'-(methylenedi-4,1-phenylene)bismaleimide (MDPB), is commercially available. The monomer with four furan groups, FGEEDR, was synthesized through the route shown in Figure 4.5b.
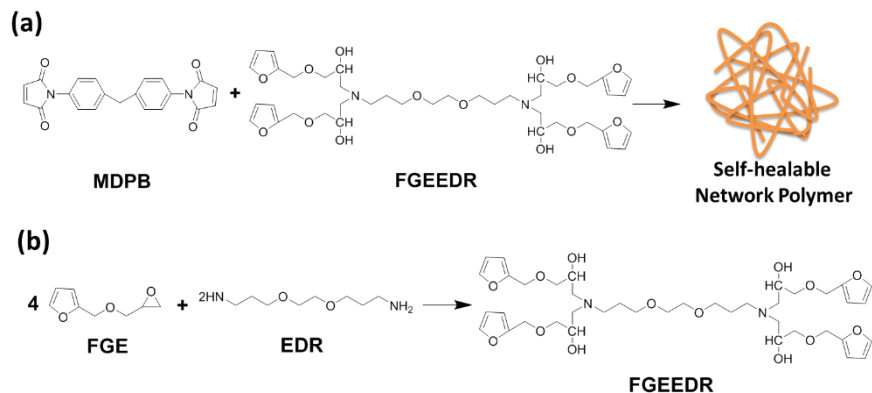
Figure 4.5 (a) Synthesis route of a healable network polymer: MDPB-FGEEDR copolymer. (b) Synthesis route of the co-monomer FGEEDR.

As shown in Figure 4.5 b, the synthesis of FGEEDR is a straightforward reaction and the yield of the reaction is 86%. NMR spectrum of the product FGEEDR is given in Figure 4.6. The broad peak in the range of 3-4 ppm is from the –OH group on FGEEDR.
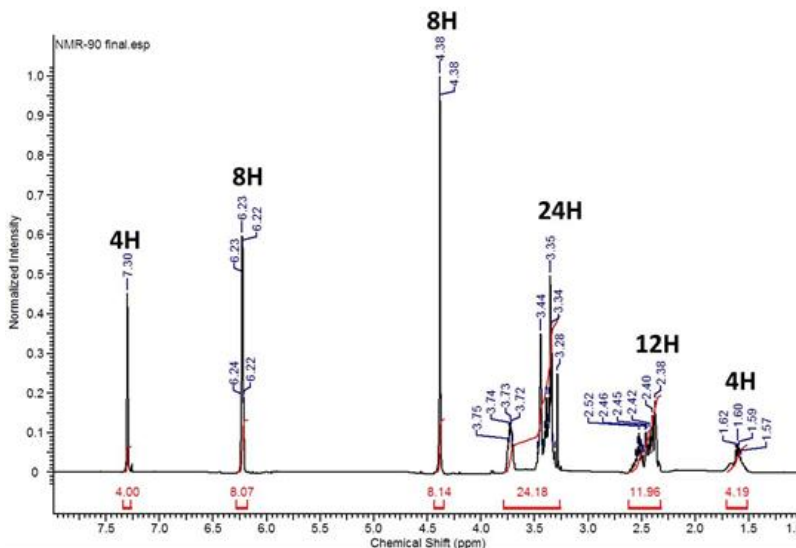
Figure 4.6 NMR spectrum of monomer FGEEDR

MDPB and FGEEDR were cross-copolymerized through a reversible Diels-Alder (D-A) cyclo-addition reaction to form the healable network polymer as shown in Figure 4.5a.

Thin films of MDPB-FGEEDR copolymer were prepared through drop-casting and polymerized under vacuum. Thin films of the MDPB-FGEEDR copolymer with size as large as 8 cm × 12 cm were readily prepared on glass substrate, and the as-prepared films are transparent as shown in Figure 4.7.

Figure 4.7 Optical photograph of a transparent MDPB-FGEEDR copolymer film (12 cm × 10 cm; the square area in light yellow color)

The C-C covalent bond formed in the D-A reaction is weaker than the other covalent bonds initially present in the two monomers and could break upon mechanical stress to regenerate the furan and maleimide functional groups. Thanks to the reversibility of the D-A reaction, the furan and maleimide groups can cross-couple again under modest heating to re-form the broken bonds. Therefore, cracks in this copolymer could heal for multiple times. To check the healing ability, in a typical experiment, a crack was cut with a razor blade across the surface of a film. The crack was around 35 μm depth, about 1/3 of the total film thickness. The film was then heated at 110 °C. The healable property of the polymer is illustrated in Figure 4.8. The driving force for the healing is the compression formed at the interface because the bottom part of the sample film was still

connected. Therefore the two cut parts tended to re-combine due to the compression stress. When being heated at 110 °C, the reversible D-A reaction had enough energy to take place, the broken D-A bonds re-formed to release the compression in the film and the crack healed. If the film were cut through and separated into two pieces, the restoring compression force would be lost, and an externally applied compression be required to bring the broken pieces together. The broken pieces compressed together should still heal.
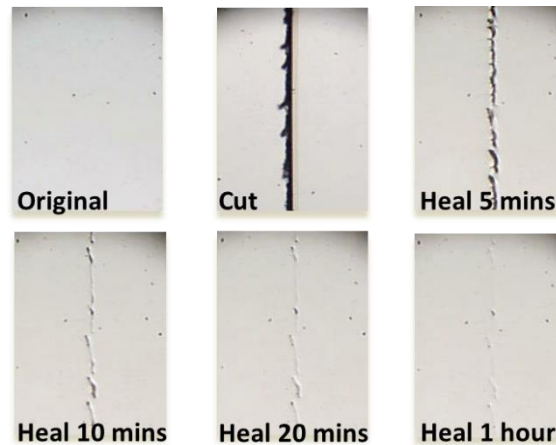
Figure 4.8 Optical micrographs showing the progress of healing of a MDPB-FGEEDR copolymer film with specified time of heating at 110 °C.

The healing process can be clearly seen from the optical micrographs shown in Figure 4.8. The freshly cut crack appears as a dark stripe shown in the upper center image in Figure 4.8. After 5 minutes of heating, some areas on the dark stripe disappeared and became light color, which means these areas have healed. After around 20 minutes of healing, most areas on the crack have recovered. In 1 hour, the dark areas have mostly disappeared, and the crack has completely healed.

The mechanical strength of the cut film can also recover after 1 hour of heating at 110 °C as shown in Figure 4.9. There were 4 types of samples tested, and at least 5 samples were tested for each type. Figure 4.9 (a) is the illustration of tensile test sample with specified dimension. The test samples were cut with 6 mm width, 10 mm length, and 100 μm thickness. The red line in the Figure 4.9 (a) indicates a cut crack along the width direction and with a depth about 1/6 that of the total thickness. The cut depth was measured under an optical microscope. Seen from Figure 4.9 (b), the tensile strength of the cut sample is 30 MPa which is only 57% of that of the original sample (53MPa). After healing, the tensile strength is increased to 43MPa which is 81% of the original staple. These results clearly indicate that the MDPB-FGEEDR copolymer is healable.
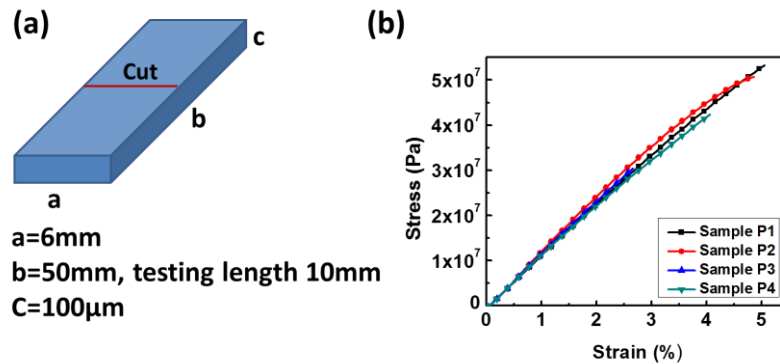
Figure 4.9 (a) Illustration of tensile test sample with specified dimension, the red line indicates a cut crack. (b) Stress-strain curves of neat copolymer samples.

4.3.2 MDPB-FGEEDR polymer / AgNWs composite conductor characterization

The fabrication procedure of a healable AgNWs-polymer composite conductor is illustrated in Figure 4.10. It starts with drop-casting a layer of AgNWs from a dispersion in methanol, followed by coating a solution of MDPB and FGEEDR co-monomers on top

of the AgNW layer. The liquid co-monomer solution is cured at 70 °C in vacuum to form

a network polymer film which is then peeled off from the release glass substrate.
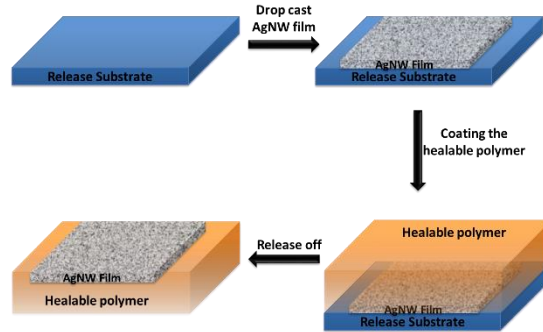
Figure 4.10 Schematic illustration of the fabrication of a healable composite conductor based on AgNWs and MDPB-FGEEDR copolymer.

The as-prepared composite conductors are semi-transparent as shown Figure 4.11a wherein the background logo can be clearly seen through. The AgNW percolation network is transferred into the surface layer of the polymer film. Surface conductivity of the resulting AgNW-polymer composite film is determined by the coating density of the AgNW percolation network originally on the release substrate. Two kinds of composite films were prepared for comparative purpose: Sample 1 with 341 mg/m^2 AgNW coating, and Sample 2 with 427 mg/m^2 AgNW coating (see Figure 4.11a). The sheet resistance of these two samples was 18.6 Ω/sq for Sample 1 and 9.5 Ω/sq for Sample 2, respectively. These values are comparable to typical ITO coatings on glass. To determine the transparency of the composite conductor, the optical transmittance of the samples was measured with a UV-Vis spectrometer, and the transmittance at 550 nm is 58% for sample 1 and 50% for sample 2, respectively (Figure 4.11b). The modest transmittance comes from the absorption of both the polymer matrix and silver nanowire layer.

(a)

Optical Image of Composite Samples

(b)
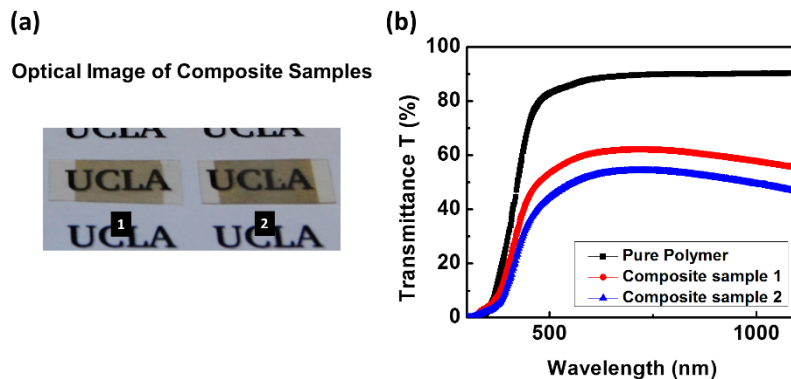
Figure 4.11 (a) Photographs of composite conductor Samples 1 and 2 with different thickness of the AgNWs layer. (b) Transmittance spectra of pure MDPB-FGEEDR copolymer 113 µm thickness and composite conductor samples of the same thickness.

The flexibility of the composite was evaluated by repeated bending-unbending cycle test. A specimen cut from Sample 2 with an area of 13 mm × 20 mm and thickness of 113 µm was bent over a NMR tube with an outside diameter of 5 mm. The initial sheet resistance of the test sample was 9.1 Ω/sq. After 1000 cycles of bending/unbending, the sheet resistance increased to 9.6 Ω/sq (see Figure 4.12(a)). The conductivity decreased by only 5.7%, indicative of high flexibility for the thin film composite conductor. The high flexibility of the composite is attributed to the flexibility of the matrix polymer and the compliance of the AgNW network.

The bonding of the AgNWs with the matrix polymer, which is also the substrate of the composite conductor, was investigated by repeated adhesion and peeling test using 3M Scotch® adhesive tape.[30] Figure 4.12(b) shows that repeated adhesion/peeling does not alter the sheet resistance. Only a 1% decrease of conductivity was observed after 100 cycles of repeated operations. The strong bonding between AgNWs and the substrate

68

polymer is essential for healing of the composite conductor in the event of surface crack formation.
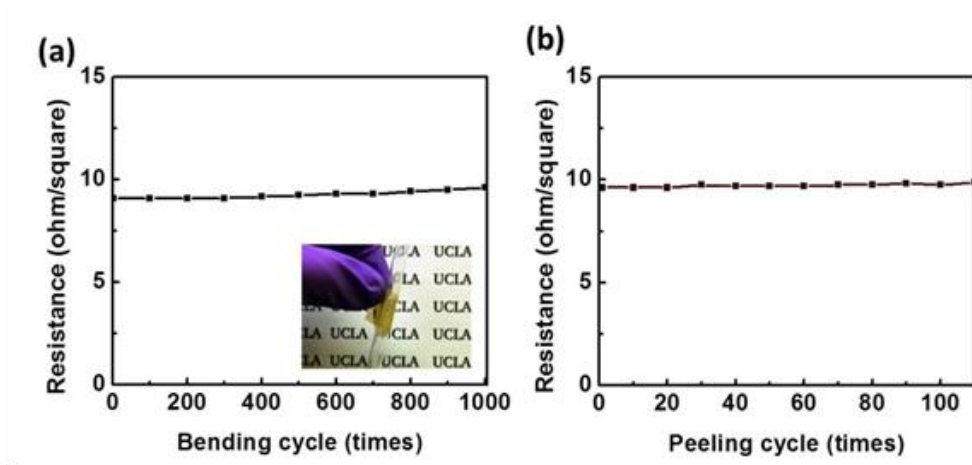
Figure 4.12 (a) Resistance changes of a Sample 2 specimen with number of bending-unbending cycles. Inset photograph shows the specimen wrapped around a 5 mm diameter tube. (b) Resistance changes of a Sample 2 specimen with cycles of adhesion and peeling with Scotch tape.

The healable property of the composite conductor was examined by cutting cracks on the conductive surface and measuring the recovery of the surface conductivity upon heating. The crack depth was about 1/3 of the film thickness, and its width across the entire width of the conductive area such that conductivity between the separated areas was completely lost. A specimen of Sample 1 with a cut crack was heated at 110°C which was chosen as an optimal temperature for both the broken D-A bonds and AgNWs to heal. There are known healing chemistry that can take place at room temperature, the so-called self-healing. However, the healing, or fusion of AgNWs to restore high conductivity, would be much slower, perhaps too slow to be practical. Its resistance change with time is shown in Figure 4.13(a). The specimen before crack formation had a measured resistance

of 18.5 Ω, corresponding to a sheet resistance of 18.6 Ω/sq. After cutting, the resistance increased to $> 3{\times}10^7$ Ω (beyond the measurement range of the multi-meter used for resistance measurement). In 20 seconds of heating at 110 ^oC, the resistance dropped to 32.2 Ω. It continued to decrease with additional heating time. After 5 minutes of heating, the resistance reached 19.1 Ω which means that the conductivity has recovered by 97%. Longer heating led to additional, but small recovery. Sample 2 with denser AgNW coating has the same performance upon cut and healing as shown in Figure 4.13 (b).
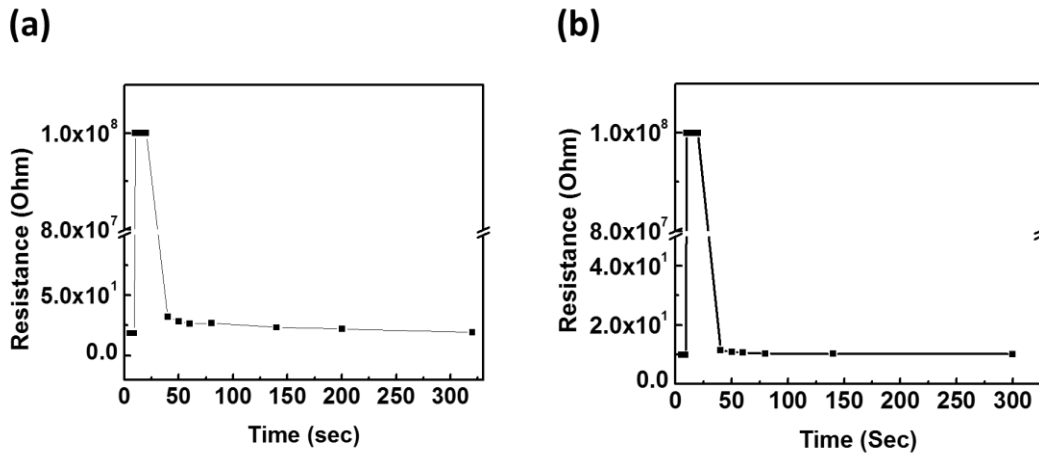
4.13 Resistance change of composite conductor Sample 1 (a) and Sample 2 (b) during a cutting and healing test.

The re-healing property of the semi-transparent composite conductor is important for the durability of functional devices and structures comprising the conductor. Thus, the cutting and healing cycle was repeated on a Sample 1 specimen at the same cut location. In each cycle, the healing was performed for 5 minutes at 110 °C. The recovery of the surface conductivity after each cut is shown in Figure 4.14. The initial resistance of the test sample was 18.5 Ω. After each cutting, the resistance increased to beyond

measurement limit. The resistance was 19.1 Ω after the first healing, and 22.7 Ω after the second cut and healing at the same location, 106.7 Ω after the third cycle, and 120.7 Ω after 4 cycles. The sheet resistance after 4 cycles is calculated to be 121 Ω/sq, which is comparable to the sheet resistance of commercial flexible transparent electrode, ITO coating on polyester substrate. The re-healing ability is rapidly lost in further cutting-healing cycles.
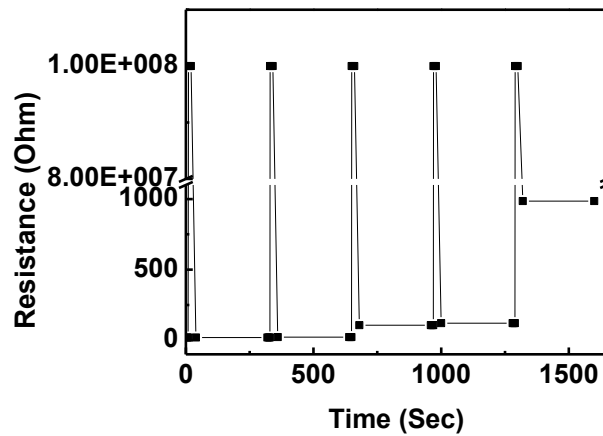
Figure 4.14 Resistance change of the composite conductor (sample 1) upon repeated cutting and healing at the same location.

Scanning electron microscopy (SEM) was used to image the healing process. Figure 4.15 shows the dense AgNWs percolation network in the composite conductor. The AgNW network is a thin layer in the surface of the MDPB-FGEEDR copolymer substrate. When a crack is cut across the surface layer, the AgNW network is divided into two halves, electrically insulated from each other (Figure 4.15b). The relatively uniform dark grey area in the crack exposes a region deep in the substrate where there are no silver nanowires. Figure inserted in Figure 4.15b shows the cross-section of the cut crack. The

thin AgNW layer is too thin to be seen at this scale. Figure 4.15c shows the crack area after 5 minutes of healing. The crack area on the right half has healed, some AgNWs are in contact with each other, and the surface appears relatively flat. The left half of the crack has not healed yet. The healing is completed in 1 hour as shown in Figure 4.15d. The crack becomes almost invisible.
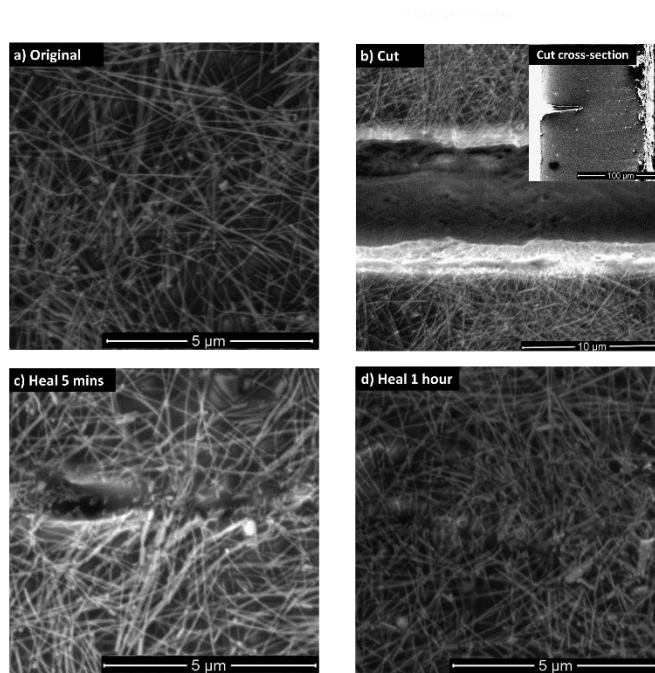
Figure 4.15 SEM images for a composite conductor specimen (Sample 1) (a), after being cut with a razor blade to form a crack in the surface (b), cross-section of the crack (inserted SEM image) after heating for 5 min (c) and 1 hour (d) at 110 ° C.

The healing property of the composite conductor is the result of the following two healing processes: the healing of the MDPB-FGEEDR copolymer substrate and the re-forming of the AgNW percolation network. The former involves D-A cyclo-addition reaction, and the latter results from the reconnection of silver nanowires over where the crack was to re-forge the percolation network. The small diameter of the nanowires

72

should allow the fusion to take place at relatively low temperature, which is important for low contact resistance.[31, 32]

Tensile tests were also done on the composite samples. Figure 4.16 shows that the initial tensile strength of composite conductor sample is 46.6MPa. After cutting a crack on surface of sample, the tensile strength decreases to 34.6MPa which is 74% of the original value. After 1 hour of healing, the tensile strength of the composite conductor recovers to 40MPa which is 86% of the initial tensile strength of the composite conductor. The composite exhibits the same stress-strain behavior as the neat polymer. This is expected as the amount of silver nanowire in the composite is extremely small, 341mg/m2, compared to the polymer's 146g/m2. The mechanical property of the composite is dominated by the matrix polymer which ensures the healing ability of the composite conductor in mechanical strength.
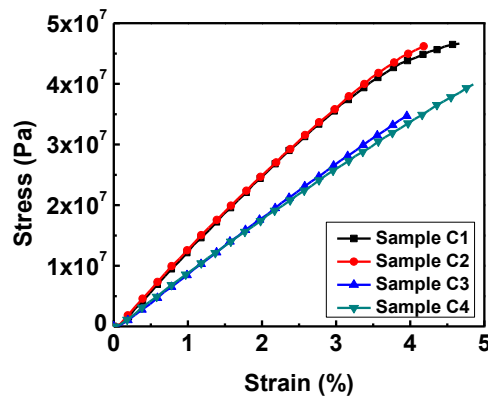
Figure 4.16 Stress-strain curves of composite conductor samples.

To demonstrate the healing property of the composite conductor, a specimen is connected in series with a green LED and a power source (Figure 4.17). The LED is lit as the resistance of the composite conductor is much smaller than that of the LED. After being

cut across the width with a surgical scalpel, the LED is off as the composite conductor is open circuited (Figure 4.17b). The grey line in the middle of the composite conductor sample as highlighted in Figure 4.17b in the red rectangular is the cut crack on the sample. The specimen is then heated at 110 °C for 3 minutes. With the help of the healing, the LED is lit again with about the same brightness as shown in Figure 4.17c. Clearly, the composite conductor can be used as electricity conducting wires in real application.
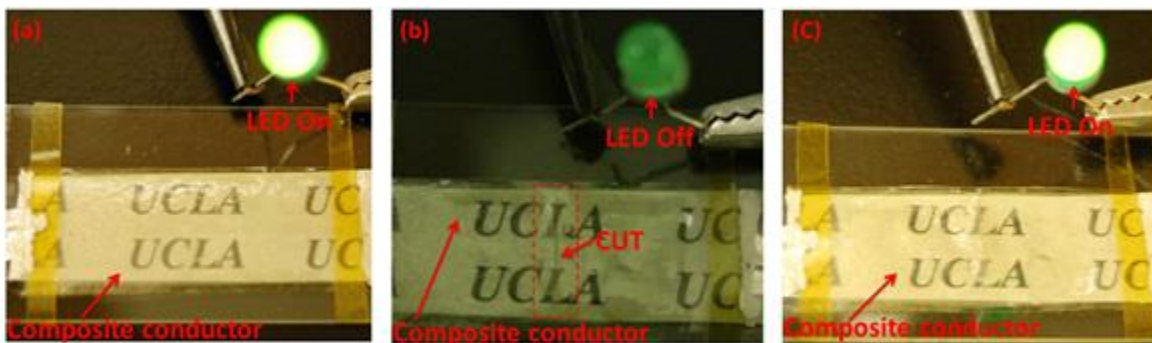
Figure 4.17 (a) A composite conductor specimen is connected in series with a lit LED. The specimen is fixed on a glass substrate. A piece of paper with UCLA logos is placed in between for convenient removal of the specimen from the glass slide and also to show the transparency of the composite conductor. (b) The specimen is cut across its width to open the circuit (see the darker grey line as indicated by the red arrow). (c) The LED is lit again after the cut specimen has healed upon heating.

4.4 Conclusion and Future Work

A healable semi-transparent composite conductor has been demonstrated based on the reversible Diels-Alder cyclo-addition reaction in the MDPB-FGEEDR copolymer and the AgNW percolation network inlaid in the polymer's surface layer. The composite is transparent, flexible, and has a surface conductivity comparable to that of indium tin

oxide coating on glass. A crack cut on the conductive surface can self-heal upon heating at 110 °C. As much as 97% of the surface conductivity can be recovered in 5 minutes. The self-healing is repeatable at the same location for multiple cycles of cutting and healing. For the future work, to make this composite conductor suitable as substrate to substitute the ITO in traditional optoelectronic devices, we need to improve the transparency for this composite conductor. Furthermore, the glass transition temperature or the soften temperature for this composite conductor need to be enhanced. After solving this two problems, healable optoelectronic device could be a very interesting work based on the current healable polymer and composite conductor.

Reference:

[1]   E. Palleau, S. Reece, S. C. Desai, M. E. Smith, and M. D. Dickey, "Self-Healing Stretchable Wires for Reconfigurable Circuit Wiring and 3D Microfluidics.," *Advanced materials*, pp. 3–6, Jan. 2013.

[2]   S. a. Odom, T. P. Tyler, M. M. Caruso, J. a. Ritchey, M. V. Schulmerich, S. J. Robinson, R. Bhargava, N. R. Sottos, S. R. White, M. C. Hersam, and J. S. Moore, "Autonomic restoration of electrical conductivity using polymer-stabilized carbon nanotube and graphene microcapsules," *Applied Physics Letters*, vol. 101, no. 4, p. 043106, 2012.

[3]   K. a Williams, A. J. Boydston, and C. W. Bielawski, "Towards electrically conductive, self-healing materials.," *Journal of the Royal Society, Interface / the Royal Society*, vol. 4, no. 13, pp. 359–362, Apr. 2007.

[4]   Q. Wei, J. Wang, X. Shen, X. a Zhang, J. Z. Sun, A. Qin, and B. Z. Tang, "Self-healing hyperbranched poly(aroyltriazole)s.," *Scientific reports*, vol. 3, p. 1093, Jan. 2013.

[5]   E. B. Murphy and F. Wudl, "The world of smart healable materials," *Progress in Polymer Science*, vol. 35, no. 1–2, pp. 223–251, Jan. 2010.

[6]   B. J. Blaiszik, S. L. B. Kramer, S. C. Olugebefola, J. S. Moore, N. R. Sottos, and S. R. White, "Self-Healing Polymers and Composites," *Annual Review of Materials Research*, vol. 40, no. 1, pp. 179–211, Jun. 2010.

[7]   R. P. Wool, "Self-healing materials: a review," *Soft Matter*, vol. 4, no. 3, p. 400, 2008.

[8]   S. D. Bergman and F. Wudl, "Mendable polymers," *Journal of Materials Chemistry*, vol. 18, no. 1, p. 41, 2008.

[9]   D. Y. Wu, S. Meure, and D. Solomon, "Self-healing polymeric materials: A review of recent developments," *Progress in Polymer Science*, vol. 33, no. 5, pp. 479–522, May 2008.

[10]   L. Huang, N. Yi, Y. Wu, Y. Zhang, Q. Zhang, Y. Huang, Y. Ma, and Y. Chen, "Multichannel and Repeatable Self-Healing of Mechanical Enhanced Graphene-Thermoplastic Polyurethane Composites," pp. 1–5, 2013.

[11]   B. J. Blaiszik, S. L. B. Kramer, M. E. Grady, D. a McIlroy, J. S. Moore, N. R. Sottos, and S. R. White, "Autonomic Restoration of Electrical Conductivity.," *Advanced materials*, pp. 398–401, Dec. 2011.

[12]   Y. Li, S. Chen, M. Wu, and J. Sun, "Polyelectrolyte multilayers impart healability to highly electrically conductive films.," *Advanced materials,* vol. 24, no. 33, pp. 4578–82, Aug. 2012.

[13]   B. C.-K. Tee, C. Wang, R. Allen, and Z. Bao, "An electrically and mechanically self-healing composite with pressure- and flexion-sensitive properties for electronic skin applications," *Nature nanotechnology*, vol. 7, no. 12, pp. 825–32, Dec. 2012.

[14]   X. Chen, M. a Dam, K. Ono, A. Mal, H. Shen, S. R. Nutt, K. Sheran, and F. Wudl, "A thermally re-mendable cross-linked polymeric material.," *Science*, vol. 295, no. 5560, pp. 1698–702, Mar. 2002.

[15]   X. Chen, F. Wudl, A. K. Mal, H. Shen, and S. R. Nutt, "New Thermally Remendable Highly Cross-Linked Polymeric Materials," *Macromolecules*, vol. 36, no. 6, pp. 1802–1807, Mar. 2003.

[16]   J. S. Park, H. S. Kim, and H. Thomas Hahn, "Healing behavior of a matrix crack on a carbon fiber/mendomer composite," *Composites Science and Technology*, vol. 69, no. 7–8, pp. 1082–1087, Jun. 2009.

[17]   J. S. Park, T. Darlington, A. F. Starr, K. Takahashi, J. Riendeau, and H. Thomas Hahn, "Multiple healing effect of thermally activated self-healing composites based on Diels–Alder reaction," *Composites Science and Technology*, vol. 70, no. 15, pp. 2154–2159, Dec. 2010.

[18]   F. Ghezzo, D. R. Smith, T. N. Starr, T. Perram, a. F. Starr, T. K. Darlington, R. K. Baldwin, and S. J. Oldenburg, "Development and Characterization of Healable Carbon Fiber Composites with a Reversibly Cross Linked Polymer," *Journal of Composite Materials*, vol. 44, no. 13, pp. 1587–1603, Mar. 2010.

[19]   K. Takahashi, Z. Guo, Y. Wang, E. Bolanos, C. Hamann-Schaffner, E. Murphy, F. Wudl, and H. T. Hahn, "Towards Development of a Self-Healing Composite using a Mendable Polymer and Resistive Heating," *Journal of Composite Materials*, vol. 42, no. 26, pp. 2869–2881, Dec. 2008.

[20]   W. Hu, X. Niu, L. Li, S. Yun, Z. Yu, and Q. Pei, "Intrinsically stretchable transparent electrodes based on silver-nanowire-crosslinked-polyacrylate composites.," *Nanotechnology*, vol. 23, no. 34, p. 344002, Aug. 2012.

[21]   J. van de Groep, P. Spinelli, and A. Polman, "Transparent conducting silver nanowire networks.," *Nano letters*, vol. 12, no. 6, pp. 3138–44, Jun. 2012.

[22]   L. Hu, H. Kim, J. Lee, P. Peumans, and Y. Cui, "Scalable coating and properties of transparent, flexible, silver nanowire electrodes," *ACS nano*, vol. 4, no. 5, pp. 2955–2963, 2010.

[23]   S. Yun, X. Niu, Z. Yu, W. Hu, P. Brochu, and Q. Pei, "Compliant silver nanowire-polymer composite electrodes for bistable large strain actuation.," *Advanced materials*, vol. 24, no. 10, pp. 1321–7, Mar. 2012.

[24]   C.-H. Chung, T.-B. Song, B. Bob, R. Zhu, H.-S. Duan, and Y. Yang, "Silver nanowire composite window layers for fully solution-deposited thin-film photovoltaic devices.," *Advanced materials,* vol. 24, no. 40, pp. 5499–504, Oct. 2012.

[25]   Z. Yu, Q. Zhang, L. Li, Q. Chen, X. Niu, J. Liu, and Q. Pei, "Highly flexible silver nanowire electrodes for shape-memory polymer light-emitting diodes.," *Advanced materials,* vol. 23, no. 5, pp. 664–8, Feb. 2011.

[26]   Z. Yu, L. Li, Q. Zhang, W. Hu, and Q. Pei, "Silver nanowire-polymer composite electrodes for efficient polymer solar cells.," *Advanced materials*, vol. 23, no. 38, pp. 4453–7, Oct. 2011.

[27]   L. Li, Z. Yu, W. Hu, C. Chang, Q. Chen, and Q. Pei, "Efficient flexible phosphorescent polymer light-emitting diodes based on silver nanowire-polymer composite electrode.," *Advanced materials*, vol. 23, no. 46, pp. 5563–7, Dec. 2011.

[28]   Q. Tian, Y. C. Yuan, M. Z. Rong, and M. Q. Zhang, "A thermally remendable epoxy resin," *Journal of Materials Chemistry*, vol. 19, no. 9, p. 1289, 2009.

[29]   Y. Sun, B. Gates, B. Mayers, and Y. Xia, "Crystalline Silver Nanowires by Soft Solution Processing," *Nano Letters*, vol. 2, no. 2, pp. 165–168, Feb. 2002.

[30]   R. Zhu, C.-H. Chung, K. C. Cha, W. Yang, Y. B. Zheng, H. Zhou, T.-B. Song, C.-C. Chen, P. S. Weiss, G. Li, and Y. Yang, "Fused silver nanowires with metal oxide nanoparticles and organic polymers for highly transparent conductors," *ACS nano*, vol. 5, no. 12, pp. 9877–82, Dec. 2011.

[31]   Y. Lu, J. Y. Huang, C. Wang, S. Sun, and J. Lou, "Cold welding of ultrathin gold nanowires.," *Nature nanotechnology*, vol. 5, no. 3, pp. 218–24, Mar. 2010.

[32]   E. C. Garnett, W. Cai, J. J. Cha, F. Mahmood, S. T. Connor, M. Greyson Christoforo, Y. Cui, M. D. McGehee, and M. L. Brongersma, "Self-limited plasmonic welding of silver nanowire junctions.," *Nature materials*, vol. 11, no. 3, pp. 241–9, Mar. 2012.

CHAPTER FIVE

Polypyrrole Copolymers Actuator with Improved Flexibility and Actuation Performance

5.1 Introduction

Electroactive polymers (EAPs) are a group of smarting polymers which change shape and/or size under the stimulus of an electric field. Electroactive polymers have been studied for a long time because of their promise in robotics applications to mimic the multifunctionalities of natural muscles.[1-3] Based on the mechanism of actuation, EAPs are classified into two categories: electronic EAPs which are driven by electric field or columbic forces; and ionic EAPs which are driven by the motion and diffusion of ions in materials. A sample of electronic EAPs is dielectric elastomers actuator. Dielectric elastomers are smart material systems which produce large strains when electrical field applied on the actuators. The structure of the actuators is an elastomeric film coated with electrodes on both sides. The two sides with electrodes are connected to an external power source. When a voltage is applied to the actuator device, the electrostatic attraction force acts. Due to the mechanical compression, the elastomer film contracts in the thickness direction and expands in the film plane directions. The elastomer film moves back to its original position when the voltage is off.[4-10] For the example of ionic electroactive polymers, conducting polymer actuators are ionic EAPs that can be actuated under low voltages, typically a few volts. Such a low actuation voltage provides tremendous advantages for many potential applications in bio-medical implants and prosthetic surgeries.[11, 12] Furthermore, conducting polymer actuators are bistable, which means they are able to retain a specific shape (volume) without external bias.

Various conducting polymers have been investigated for actuator applications, such as polypyrrole (PPy), polyaniline, poly (3,4-ethylenedioxythiophene) (PEDOT), etc.[13-15] Among these, PPy has shown greater advantages in stability and biocompatibility; moreover, PPy can be easily fabricated into micrometer size actuators.[16-18]

In principle, the working mechanism for polypyrrole actuators involves volume change as a result of diffusion of ions into or out of the polymer during electrochemical redox. There are three scenarios of volume change depending on the size of the original dopants in the polypyrrole and the ions available in the electrolyte solution,[19-22] as illustrated in Figure 5.1.

(1) $PPy^+(A^-) + e^- \rightarrow PPy^0 + A^-$

(2) $PPy^+(A^-) + e^- + M^+ \rightarrow PPy^0(A^-M^+)$

(3) $PPy^+(A^-) + e^- + M^+ \rightarrow PPy^0(A^-M^+) \rightarrow PPy^0 + A^- M^+$ (solution)
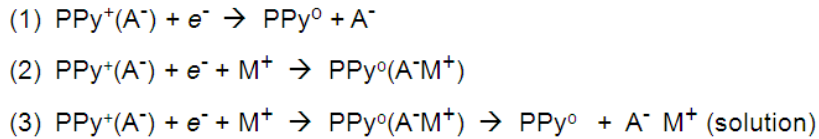
Figure 5.1 Three possible volume change schemes in conducting polymer during electrochemical reduction. (Reproduced from [19])

Scheme (1) is for polypyrrole doped by a small anion such as chloride (Cl⁻). PPy(Cl⁻) undergoes volume contraction when it is dedoped and the dopant anions diffuse out of the polymer. Upon re-doping of the neutral PPy^0 in a NaCl solution, Cl⁻ from the solution diffuse into the polymer. Scheme (2) is for polypyrrole doped by a large anion like dodecyl benzenesulfonate (DBS⁻). PPy(DBS⁻) expands under reduction potential due to the insertion of cations into the polymer to compensate DBS⁻. DBS anions are too bulky to diffuse out of the polymer. When PPy^0 (DBS⁻ Na⁺) is oxidized, it shrinks as the cations diffuse out of the polymer. Scheme (3) is for polypyrrole doped by tosylate (p-methylbenzenesulfonate, TsO⁻). During reduction, PPy (TsO⁻) undergoes initial rapid

expansion followed by long, gradual shrinking. This volume change is due to initial fast cations insertion for charge compensation and subsequently slow salt draining out of the reduced neutral PPy. After the salt draining, the polymer actuates like PPy (Cl$^-$).

Among the three types of doped PPy, PPy (DBS$^-$) attracts the most attention. Compared to PPy (TsO$^-$), the actuation performance of PPy (DBS$^-$) is stable.[20, 21] Moreover, compared to PPy (Cl$^-$), PPy (DBS$^-$) actuation based on cations diffusion gives more choice in tuning the actuation strain. From the application point of view, high-quality PPy (DBS$^-$) films can electrochemically deposited from aqueous solutions, which should be more compliant with GMP requirements.[17-18]

PPy(DBS$^-$) actuators are mostly based on bilayer bending actuation. The flexibility of PPy(DBS$^-$) is critical, not only to the actuation cycle lifetime, but also to the safe handling, shipping, and implementation of the bending actuators. To improve the polymer's flexibility, it is worthwhile to review the causes for PPy's brittleness. The backbone of PPy (DBS$^-$) is an extended π-conjugated chain that is rigid. Cross-linking makes the polymer more brittle.[23] The inter-chain interaction due to π-π overlapping and strong electrostatic force among the charged polymer chains and the DBS- anions further increases the brittleness.[24] In order to lower the crosslink density and weaken the interchain interactions, copolymerization of pyrrole with pyrrole derivatives containing substituent groups have been carried out. The side groups in the copolymers should effectively separate the polymer chains and lower the probability of crosslinking. In this chapter, we summarized our improvement work on polypyrrole actuator through the selection of suitable pyrrole derivatives and evaluation of the copolymers for flexible bending actuators.

5.2 Experiments

Eleven different monomers are tested for copolymerization with pyrrole. The chemical structures are listed in Table 5.1. All chemicals were purchased from Sigma-Aldrich and used without further purification. Water used in experiments was deionized. Solubility of all the monomers was tested first in water and/or water/propylene carbonate (7:1) solvents. Soluble monomers with solubility higher than 0.01 mol/L were selected for electrochemical polymerization under constant oxidation potential. The oxidation potentials were determined through cyclic voltammetry tests through the onset of the oxidation peak.

5.2.1 Solubility Test

The first step is to check the solubility of each of the 11 monomers in different solvents. Two solvents were chosen: H_2O and mixture of propylene carbonate (PC) and H_2O with weight ratio of 7 to 1, both being suitable solvents for the pyrrole electropolymerization. Since the typical electropolymerization uses 0.1 mol/L DBSNa and 0.1 mol/L pyrrole. For solubility test of the co-monomers, 0.1 mol/L was set as the standard checking concentration. Firstly, a 0.1 mol/L co-monomer was dispersed in H_2O and the mixture of PC/H_2O. When the co-monomer did not completely dissolved in the solvent at 0.1 mol/L, then more solvent was added until the monomer became fully dissolved and that concentration was recorded.

5.2.2 Oxidation Potential Measurement

Co-monomers with a measured solubility greater than 0.01mol/L in either H_2O or PC/ H_2O mixture solvent were considered to be candidates for copolymerization. The

oxidation potential of each of the candidate monomers was tested through cyclic voltammetry (CV) method. CV testing was done with a three-electrode electrochemical cell (BASI Epsilon potentiostat). Platinum (Pt) wires were used as both working and counter electrode and Ag/AgCl was used as the reference electrode. Pt wires were first polished by fine sand paper (600 grits) and then soaked with acetone and 1mol/L H_2SO_4 acid. Finally the Pt wires were ultrasonic washed twice in DI water. Before the CV testing for each monomer, background scanning was done in 0.1 mol/L DBSNa water solution and 0.1 mol/L DBSNa PC/water mixture solvent solution. Then CV testing for each of the monomers was done. The voltage scanning range for all the CV testing was from -2000 mV to +2000 mV and the starting point and end point both were 0 V. The scanning rate was 10 mV/sec.

5.2.3 Preparation of 3-methylpyrrole Homopolymer and 3-methylpyrrole/Pyrrole Copolymer

As one of the chosen monomers for copolymerization, 3-methylpyrrole homopolymer and its copolymer with pyrrole were electrochemically prepared. For homopolymer polymerization, stainless steel was used as working electrode, to electrochemically polymerize 3-methyl pyrrole in an aqueous solution containing 0.05mol/L 3-methylpyrrole and 0.1mol/L DBSNa. For copolymer preparation, stainless steel was still served the as working electrode for electrochemical polymerization of 3-methylpyrrole/pyrrole in a solution of 0.05mol/L 3-methylpyrrole, 0.05mol/L pyrrole and 0.1mol/L DBSNa in water. A three-electrode electrochemical cell (BASI Epsilon potentiostat) was used with an Ag/AgCl reference electrode and a stainless steel plate counter electrode. A potential of 600 mV was applied at room temperature and 3-

methylpyrrole or 3-methylpyrrole/pyrrole were oxidized onto stainless steel surface to form a homopolymer or a copolymer film.

5.2.4 Preparation of N-methylpyrrole homopolymer and N-methylpyrrole/Pyrrole copolymer

As another chosen monomer for copolymerization, N-methylpyrrole homopolymer and its copolymer with pyrrole were electrochemically prepared also. For homopolymer polymerization, stainless steel was used as working electrode and electrochemically polymerization was done on stainless steel with an aqueous solution containing 0.1mol/L N-methylpyrrole and 0.1mol/L DBSNa. For copolymerization, stainless steel was still served the as working electrode for electrochemical polymerization of N-methylpyrrole/pyrrole in a solution of 0.1mol/L N-methylpyrrole, 0.1mol/L pyrrole and 0.1mol/L DBSNa in water. A three-electrode electrochemical cell (BASI Epsilon potentiostat) was still used with an Ag/AgCl reference electrode and a stainless steel plate counter electrode. A potential of 700 mV was applied at room temperature and N-methylpyrrole or N-methylpyrrole/pyrrole were oxidized onto stainless steel surface to form a homopolymer or a copolymer film.

5.2.5 N-methylpyrrole/pyrrole copolymer actuator performance test

As a promising material, N-methylpyrrole and pyrrole copolymer was used for unimorph bending actuators fabrication. A one side Au coated polyimide substrate with total thickness of 1 μm was used as working electrode. Counter electrode was stainless steel and reference electrode was Ag/AgCl electrode. A three-electrode electrochemical cell (BASI Epsilon potentiostat) was used and N-methylpyrrole/pyrrole copolymer was

electrochemically deposited on this Au coated polyimide substrate from an aqueous solution with 0.1mol/L N-methylpyrrole, 0.1mol/L pyrrole and 0.1mol/L DBSNa. A potential of 700 mV was applied at room temperature and a copolymer film was form on Au coated polyimide substrate. Therefore, a uniform copolymer bending actuator with structure of one active N-methylpyrrole/pyrrole copolymer layer and one non-active substrate layer was fabricated.
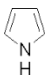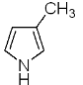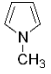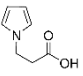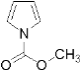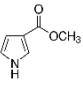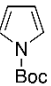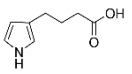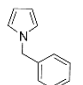
Before the electrochemical actuation testing, flexibility test was done through mechanical bending method. Then the bending actuation test was conducted in aqueous solution containing 0.1mol/L NaCl in the three electrode electrochemical cell (BASI Epsilon potentiostat). One end of the copolymer bending actuator fabricated above was hanged under electrode clip as the working electrode with the other end kept free in water solution. A Cu foil was used as counter electrode and an Ag/AgCl electrode was served as reference electrode. Firstly, a reduction potential -850 mV was applied for 2 minutes to reduce the copolymer active layer and then an oxidized potential + 850 mV was applied to oxidize the copolymer active layer for another 2 minutes. Such a reduction-oxidation (redox) process was regarded as one actuation cycle and 5 cycles were repeated in order to see the reversibility of the bending performance. A video camera was fixed in front of the cell setup to record the deflection of the free end during the electrochemical redox of copolymer layer.
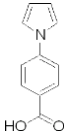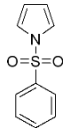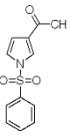
5.3 Results and Discussion

5.3.1 Solubility of monomers

In order to select proper monomers for further copolymerization with pyrrole, solubility of monomers in solvents of water and PC/water (1:7 by weight) mixture was tested. Table 5.1 is the summary of chemicals and their solubility test results for all the monomers including pyrrole.

Table 5.1 Summary of monomers name, chemical structure and their solubility test results.

Chemical Name and Formula	Molecular Structure	Solubility (mol/L) in H_2O with 0.1mol/L DBSNa	Solubility (mol/L) in PC/H_2O with 0.1mol/L DBSNa
Pyrrole C_4H_5N		>0.1	>0.1
3-Methylpyrrole C_5H_7N		>0.1	>0.1
N-Methylpyrrole C_5H_7N		>0.2	>0.2
1H-Pyrrole-1-propanoic acid $C_7H_9NO_2$		>0.1	>0.02
Methyl 1-pyrrolecarboxylate $C_6H_7NO_2$		>0.05	>0.02
Methyl 1H-pyrrole-3-carboxylate $C_6H_7NO_2$		>0.025	>0.02
tert-Butyl 1-pyrrolecarboxylate $C_9H_{13}NO_2$		~0.25	~0.02
4-(3-Pyrrolyl)butyric acid $C_8H_{11}NO_2$		<0.01	<0.01
N-Benzylpyrrole $C_{11}H_{11}N$		<0.01	<0.01

4-(1H-Pyrrol-1-yl)benzoic acid $C_{11}H_9NO_2$		<0.01	<0.01
1-(Phenylsulfonyl)pyrrole $C_{10}H_9NO_2S$		<0.01	<0.01
3-Acetyl-1-(phenylsulfonyl)pyrrole $C_{12}H_{11}NO_3S$		<0.01	<0.01

As shown clearly in table 5.1, the solubility of 3-methylpyrrole, N-methylpyrrole, and 1H-pyrrole-1-propanoic acid are all greater than 0.1mol/L which is comparable to that of pyrrole in both solvents. For methyl 1-pyrrolecarboxylate, methyl 1H-pyrrole-3-carboxylate, and tert-Butyl 1-pyrrolecarboxylate, their solubility in water and in PC/H_2O mixture are still higher than 0.01mol/L which although are 2 to 4 times worse than that of pyrrole in both solvents. However, 0.01mol/L was considered as high enough for polymerization. On the other hand, for the other five monomers, 4-(3-Pyrrolyl) butyric acid, N-Benzylpyrrole, 4-(1H-Pyrrol-1-yl)benzoic acid, 1-(Phenylsulfonyl)pyrrole, and 3-Acetyl-1-(phenylsulfonyl)pyrrole, their solubility in both solvents are smaller than 0.01mol/L which is too low to be suitable for polymerization because if the monomer concentration is too low, it is hard to get a uniform film. In summary, 3-Methylpyrrole, N-Methylpyrrole, 1H-Pyrrole-1-propanoic acid, Methyl 1-pyrrolecarboxylate, Methyl 1H-pyrrole-3-carboxylate, and tert-Butyl 1-pyrrolecarboxylate were selected for further copolymerization with pyrrole monomer. Therefore, oxidation potential test for them were done in next step.

5.3.2 Oxidation potential

In order to do copolymerization, the oxidation potential for each monomer was tested. As described in the experimental section, the oxidation potential for each of the monomers was tested through cyclic voltammetry. A total of 6 monomers were tested and the summary of their CV testing results is shown in table 5.2.

Table 5. 2 Summary of oxidation potential test results for monomers with solubility > 0.01mol/L in selected solvents.

Chemical Name	Testing Solution	Results
3-Methylpyrrole	0.1mol/L in $H_2O\surd$	Oxidation potential range: ~350-500 mV in H_2O; Black deposition on electrode;
N-Methylpyrrole	0.1mol/L in $H_2O\surd$	Oxidation potential range: ~500 mV in H_2O; Black deposition on electrode;
1H-Pyrrole-1-propanoic acid	0.1mol/L in H_2O × 0.02mol/L in PC/H_2O×	Current stayed very low before hydrolysis; No deposition and only hydrolysis on electrode;
Methyl 1-pyrrolecarboxylate	0.05mol/L in H_2O× 0.02mol/L in PC/H_2O×	Current stayed very low before hydrolysis; No deposition and only hydrolysis on electrode;
Methyl 1H-pyrrole-3-carboxylate	0.025mol/L in H_2O× 0.02mol/L in PC/H_2O×	Current stayed very low before hydrolysis; No deposition and only hydrolysis on electrode;
tert-Butyl 1-pyrrolecarboxylate	0.01mol/L H_2O 0.02mol/L in PC/H_2O×	Current stayed very low before hydrolysis; No deposition and only hydrolysis on electrode;

$\surd$: represents CV testing was done in this solution and also there were black deposition on electrode during CV testing.

×: represents CV testing was done in this solution but no deposition on electrode during CV testing.

As shown in table 5.2, only for 3-methylpyrrole and N-methylpyrrole testing, black film was deposited on the working electrode by sweeping the potential between -2000mV and 2000mV during CV scanning with clear monomer oxidation peak shown on CV curves, which means polymerization occurred during the CV testing. Their CV scanning curves were given in Figure 5.2 and Figure 5.3. For the testing with the other 4 monomers, there was no any deposition on the working electrode and no monomer oxidation peak shown from CV curve except water hydrolysis. Therefore, only 3-methylpyrrole and N-methylpyrrole were selected for next copolymerization with pyrrole monomer.
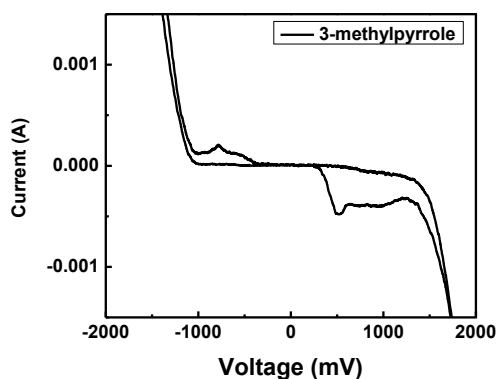
Figure 5.2 Cyclic voltammetry (CV) curve of 3-methylpyrrole in water

As shown in Figure 5.2, 3-methylpyrrole has onset oxidation potential at around 350 mV and it reaches its peak current at 500mV. As observed during the CV testing, at about 600 mV, there was a layer of black deposition on the working electrode and there are bubbles on the counter electrode, which indicates the occurrence of electrochemical polymerization. Therefore, the applied potential for the polymerization was chosen as 600 mV.
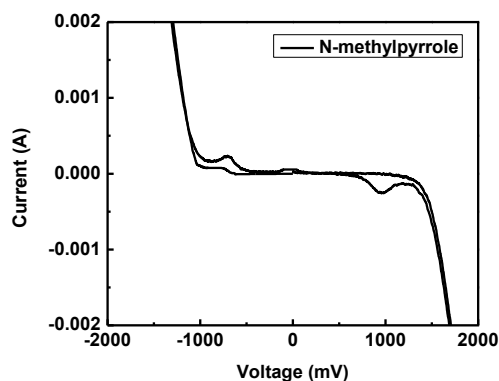
Figure 5.3 Cyclic voltammetry (CV) curve of N-methylpyrrole in water

As shown from Figure 5.3, onset oxidation potential of N-methylpyrrole is at around 500mV. Over that potential, the current increased drastically together with a layer of black deposition formed on the working electrode immediately. The applied potential for N-methylpyrrole was chosen as 700mV for its polymerization, which is the same as that for pyrrole polymerization.

Although the solubility of other 4 monomers, 1H-Pyrrole-1-propanoic acid, Methyl 1-pyrrolecarboxylate, Methyl 1H-pyrrole-3-carboxylate and tert-Butyl 1-pyrrolecarboxylate was larger than 0.01mol/L which is large enough for polymerization, as observed, there were no deposition on the working electrodes during the CV sweeping from -200mV to 2000mV, which suggests that those monomers were hard to be electrochemically polymerized at the potential range between -2000mV and 2000mV. The CV curve of Methyl 1H-pyrrole-3-carboxylate is shown in Figure 5.4 as one example of the CV curves for those four monomers. It is clear from Figure 5.4 that before the water hydrolysis, the current stayed at very low level which corresponds to no deposition on working electrode.
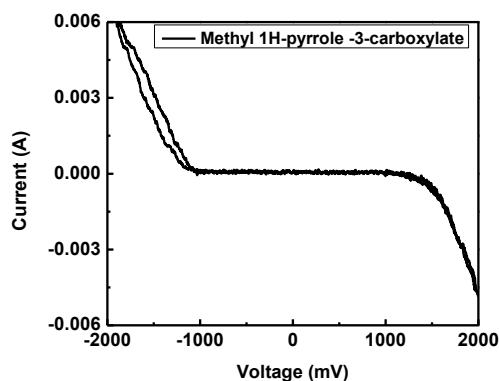
Figure 5.4 Cyclic voltammetry (CV) curve of Methyl 1H-pyrrole -3-carboxylate in water

To understand the reason why some monomers can be polymerized while the others cannot, it is necessary to look into the mechanism during electrochemical polymerization of pyrrole and its derivatives. The active species of those reactions were now widely accepted to involve radical cations. After the initial oxidation of the monomer, the radical cations are formed, followed by reacting with other monomers present in the solution to form oligomeric products and then form the polymer. The extended conjugation in the polymer lowers the oxidation potential as compared to the oxidation potential of the monomer itself. Because of the decrease in oxidation potential, the synthesis and doping of the polymer are generally done simultaneously. The anion is incorporated into the polymer to ensure the electrical neutrality of the film and at the end of the reaction; a polymeric film is formed at the anode. Radical cations formed during the polymerization process leads us to use the electrophilic substitution reaction mechanism as a basis for our explanation.[25] An electron-donating side group stabilizes transition state cations, thereby aiding polymerization. Furthermore, the electron-donating effect can help to lower the oxidation potential; therefore less over oxidation occurs during the polymerization, which might result in a better flexibility of the final films. Inversely, an

91

electron-withdrawing side group destabilizes the transition state, hindering polymerization. The methyl group, an electron-donating group, contained in N-Methylpyrrole and 3-Methylpyrrole, is further evidence for this conclusion. The side groups for 1H-Pyrrole-1-propanoic acid, Methyl 1-pyrrolecarboxylate, Methyl 1H-pyrrole-3-carboxylate, and tert-Butyl 1-pyrrolecarboxylate are all electron withdrawing group consequently leading to the failure for electrochemical polymerization for those monomers.[26] It should also be noted that the steric hindrance might also play a role to affect the reactivity of those pyrrole derivatives. The steric effect of large side group may be another reason for failure of the polymerization of those monomers.

5.3 3-Methylpyrrole and pyrrole copolymer

Both 3-methylpyrrole homopolymer and 3-methylpyrrole-pyrrole copolymer were prepared. The homopolymer was polymerized at 600mV with 10C of total charges consumed during the polymerization. The resulting free standing films were thin and brittle. The 3-methylpyrrole-pyrrole copolymer was prepared at the same condition as the homopolymer. The copolymer film was a biscuit-like brittle thin film. The thin films of 3-methylpyrrole homopolymer and 3-methylpyrrole-pyrrole copolymer were brittle, more so than polypyrrole films. This could be resulted from over-oxidation. The oxidation potential for 3-methylpyrrole was lower than pyrrole, 600mV may lead to certain degree of overoxdization of 3-methylpyrrole polymer chain or segments.

5.3.4 N-methylpyrrole and pyrrole copolymer

Both poly (N-methylpyrrole) homopolymer and N-methylpyrrole-polypyrrole copolymer were prepared. The polymerization of N-methylpyrrole homopolymer was done at 700

mV with a total polymerization charge of 10 C. N-methylpyrrole homopolymer was found to be rigid with a surface resistance around 1-10 M Ω/sq. This is similar to the values reported in literature.[26-28] It was easy to peel off the homopolymer film from the substrate without breaking any of the film. The N-methylpyrrole-pyrrole copolymer at 1:1 molar ratio was also polymerized at 700 mV with 10C of charge consumed. The surface resistance of the copolymer was around 1000 Ω/sq. This value is comparable to that of polypyrrole prepared by the similar conditions. In order to check the flexibility of the copolymer, free standing films of the copolymer and polypyrrole with the same size and thickness were prepared. After mechanically bending fatigue test at bending angle of around 70 degree, the of copolymer films showed higher flexibility than the polypyrrole films. They survived more bending cycles before final failure.

5.3.5 N-methylpyrrole and Pyrrole Copolymer Actuator Performance Testing

Due to the increased flexibility of the N-methylpyrrole-pyrrole copolymer film, unimorph bending actuators were fabricated based on the 1:1 molar ratio copolymer as shown in Figure 5.5a. The copolymer was deposited on a 1µm thick polyimide substrate coated on one side with a thin layer of gold. The size of this actuator was 8mm by 40mm. The thickness of copolymer layer was 50µm.

Figure 5.5 Pictures show flexibility of a copolymer unimorph actuator

In Figure 5.5b, the same unimorph was curved into the shape required for an intended application for the device. Figure 5.5c shows the unimorph curved into a full circle with a diameter 1cm. In these experiments, the copolymer layer was dried in air. PPy(DBS) in similar configuration would have broken under similar conditions.

Figure 5.6 Actuation performance of an N-methylpyrrole-pyrrole copolymer actuator

In Figure 5.6, all of the black stripes in the middle of the beaker is the N-methylpyrrole-pyrrole copolymer actuator with the same unimorph architecture as the ones shown in Figure 5.5. The copolymer layer faces the counter electrode to the right. Figures 5.6a to 5.6c show the actuation from oxidized state (5.6a) to moderately reduced state (5.6b) and to fully reduced state (5.6c). The bending of the unimorph is resulted from the volume increase of the coolymer layer during reduction when cations are inserted to compensate the charges on DBS$^-$. Alternating the polarity of the applied voltage reverses the bending of the actuator.

The response speed of the N-methylpyrrole-pyrrole copolymer based actuator was slower than that of the pure polypyrrole actuator. This could be caused by the differences in morphology or in conductivity. The conductivity of N-methylpyrrole homopolymer is two orders of magnitude lower than that of polypyrrole. However, the 1:1 molar ratio

copolymer has conductivity similar to that of polypyrrole. The morphology could be the main factor in slowing down the response speed of the copolymer.

5.4. Conclusion and Further Work

Various pyrrole derivatives were studied for the electrochemical co-polymerization with pyrrole monomer. The monomers that passed the screening of solubility and CV testing were tried for polymerization of homopolymer first. Copolymers with pyrrole were successfully synthesized with N-methylpyrrole/pyrrole and 3-methylpyrrole/pyrrole pairs. The N-methylpyrrole/pyrrole copolymer showed improved flexibility over than that of pyrrole homopolymer. Unimorph bending actuators were fabricated based on the N-methylpyrrole/pyrrole copolymer. Large bending angle was observed by switching the potential from -850mV to 850mV. The actuation was reversible. For the future work, the mechanical properties for those newly developed polypyrrole copolymers need to be carefully characterized. Bimorph bending actuator device based on polypyrrole copolymers could be an interesting direction as it will be suitable for application in implantable medical device area. Thereafter, to establish the database about the blocking force, bending angle, actuation holding time without electrical field and lifetime for the bimorph polypyrrole copolymer actuator will be very necessary work.

Reference:

[1]   Kwang J. Kim and Satoshi Tadokoro (eds.), "*Electroactive Polymers for Robotic Applications: Artificial Muscles and Sensors*", Springer Press, Verlag, London, 2007.

[2]   Y. Bar-Cohen (ed.), Electroactive *Polymer (EAP) Actuator as Artificial Muscles: Reality, Potential, and Challenges Second Edition*, SPIE Press, Bellingham, Washington, 2004.

[3]   P. Brochu and Q. Pei, "Advances in dielectric elastomers for actuators and artificial muscles," Macromolecular rapid communications, vol. 31, no. 1, pp. 10–36, Jan. 2010.

[4]   S. Yun, X. Niu, Z. Yu, W. Hu, P. Brochu, and Q. Pei, "Compliant silver nanowire-polymer composite electrodes for bistable large strain actuation.," Advanced materials (Deerfield Beach, Fla.), vol. 24, no. 10, pp. 1321–7, Mar. 2012.

[5]   R. Pelrine, R. Kornbluh, J. Joseph, R. Heydt, Q. Pei, and S. Chiba, "High-field deformation of elastomeric dielectrics for actuators," Materials Science and Engineering: C, vol. 11, no. 2, pp. 89–100, Nov. 2000.

[6]   R. Pelrine, "High-Speed Electrically Actuated Elastomers with Strain Greater Than 100%," Science, vol. 287, no. 5454, pp. 836–839, Feb. 2000.

[7]   S. M. Ha, W. Yuan, Q. Pei, R. Pelrine, and S. Stanford, "Interpenetrating Polymer Networks for High-Performance Electroelastomer Artificial Muscles," Advanced Materials, vol. 18, no. 7, pp. 887–891, Apr. 2006.

[8]   Q. Pei, M. Rosenthal, S. Stanford, H. Prahlad, and R. Pelrine, "Multiple-degrees-of-freedom electroelastomer roll actuators," Smart Materials and Structures, vol. 13, no. 5, pp. N86–N92, Oct. 2004.

[9]   Z. Yu, W. Yuan, P. Brochu, B. Chen, Z. Liu, and Q. Pei, "Large-strain, rigid-to-rigid deformation of bistable electroactive polymers," Applied Physics Letters, vol. 95, no. 19, p. 192904, 2009.

[10]   W. Yuan, L. B. Hu, Z. B. Yu, T. Lam, J. Biggs, S. M. Ha, D. J. Xi, B. Chen, M. K. Senesky, G. Grüner, and Q. Pei, "Fault-Tolerant Dielectric Elastomer Actuators using Single-Walled Carbon Nanotube Electrodes," Advanced Materials, vol. 20, no. 3, pp. 621–625, Feb. 2008.

[11]   E. Smela, O. Inganäs, Q. Pei, I. Lundström, "Electrochemical muscles: Micromachining fingers and corkscrews", *Adv. Mater.*, 9, 630-632, 1993.

[12]   E. Jager, E. Smela, O. Inganas, "Microfabricating conjugated polymer actuators," *Science*, 290, 1540-1545, 2000.

[13]   E.Smela, W. Lu, B.Mattes, "Polyaniline actuators Part 1. PANI(AMPS) in HCl", *Synth. Met.*, 151, 25-42, 2005.

[14]   C. Baker, B. Shedd, P. Innis, P. Whitten, G. Spinks, G. Wallace, R. Kaner, "Monolithic actuators from flash-welded polyaniline nanofibers", *Adv. Mater*, 20, 155-158, 2008.

[15]   M. Cho, H. Seo, J. Nam, H. Choi, J. koo, K. Song, Y. Lee, "A solid state actuator based on the PEDOT/NBR system", *Sens. & Actu. B*, 119, 621-624, 2006.

[16]   Smela, O. Inganäs, I. Lundström, "Controlled Folding of Micrometer-Size Structures", Science, 268 (5218), 1735-1738, 1995.

[17]   E. Smela, "Conjugated polymer actuators for biomedical applications", *Adv. Mater.*, 15, 481-494, 2003.

[18]   E. Smela, "Conjugated polymer actuators", *MRS Bulletin*, 33, 197-204, 2008.

[19]   Q. Pei, O. Inganas, "Conjugated polymers and the bending cantilever method: electrical muscles and smart devices", *Adv. Mater.*, 4, 277-278, 1992.

[20]   Q. Pei, O. Inganas, "Electrochemical applications of the bending beam method 1. mass-transport and volume changes in polypyrrole during redox", *J. Phys. Chem.*, 96, 10507-10514, 1992.

[21] Q. Pei, O. Inganas, "Electrochemical applications of the bending beam method 2. electroshrinking and slow relaxation in polypyrrole", *J. Phys. Chem.*, 97, 6034-6041, 1993.

[22]   Q. Pei, O. Inganas, "Electrochemical applications of the bending beam method; a novel way to study ion transport in electroactive polymers", *Solid State Ionic*, 60, 161-166, 1993.

[23]   U. Gedde (eds.), *Polymer Physics*, Springer Press, 1995.

[24]   R. Ebewele (eds), "*Polymer science and technology*", CRC Press, 2002

[25]   E.Genies, G. Bidan, A.Diaz, "Spectroelectrochemical study of polypyrrole films", *J. Electroanal. Chem*, 149, 101-113, 1983.

[26] S.Sadki, P.Schottland, N.Brodie, G Sabouraud, "The mechanisms of pyrrole electropolymerization", *Chem. Soc. Rev*, 29, 283-293, 2000.

[27] R. Singh, A. Narula, R. Tandon, A, Mansigh, S. Chandra,"Low frequency alternating current conduction and dielectric relaxation in polypyrrole, poly (N-methyl pyrrole), and their copolymers, *J. Appl. Phys*, 80, 985-992, 1996.

[28] M. Cross, D. Walton, N.Morse, R. Mortimer, D. Rosseinsky,D. Simmonds, " A voltammetric survey of steric and β-linkage effects in the electropolymerisation of some substituted pyrrole", *J. Electroanal. Chem.*, 189, 389-396, 1985.

CHAPTER SIX

Ferroelectric Polymer / Ceramics Nano-Composite for Solid-state Refrigerator Application Based on Electrocaloric Effect

6.1 Introduction

As stated in chapter 1, in the group of smarting and functional polymers, ferroelectric polymers are a group of crystalline polar polymers that are also ferroelectric.[1, 2] Ferroelectrics maintain a permanent electric polarization that can be reversed or switched upon an external electric field. Ferroelectric polymers, such as polyvinylidene fluoride (PVDF), are widely used in acoustic transducers and electromechanical actuators because of their inherent piezoelectric response, and as heat sensors because of their inherent pyroelectric response.[3] Beyond those, solid state refrigerator based on the electrocaloric effect of ferroelectrics has attracted great attention and investigation recently.[4-8] For traditional refrigeration using Freon as the refrigerant, the large volume of the whole system limits it application in small devices with cooling need. Currently, lots of electronic devices need the solid state cooling.[9] In this chapter, we would like to review the mechanism of electrocaloric effect in solid state refrigeration application and then summarized our efforts in developing nanocomposite from ferroelectric polymers / ceramics and our achievements in fabricating integration electrocaloric effect based refrigeration device.

6.1.1 Thermodynamically Analysis on the Principle of Refrigerator

Refrigerator is an example of a heat pump, which applies the reverse principle as a heat engine.[9] Heat generally moves from hot side to cold side as shown in Figure 6.1(a) for heat engine, but heat pump works against the temperature gradient. As showing in Figure 6.1 (b), the heat pump removes heat from the cold reservoir to the hot reservoir when work is input to the heat pump. This causes the hot reservoir becomes hotter and the cold reservoir become cooler. Thermodynamically, the heat pump works as a reversed cycle of the Carnot cycle. Figure 6.2 (a) shows the reversed Carnot cycle (pressure-volume diagram) to analysis of the heat pump and Figure 6.2 (b) shows the corresponding temperature and entropy change during the cycle.
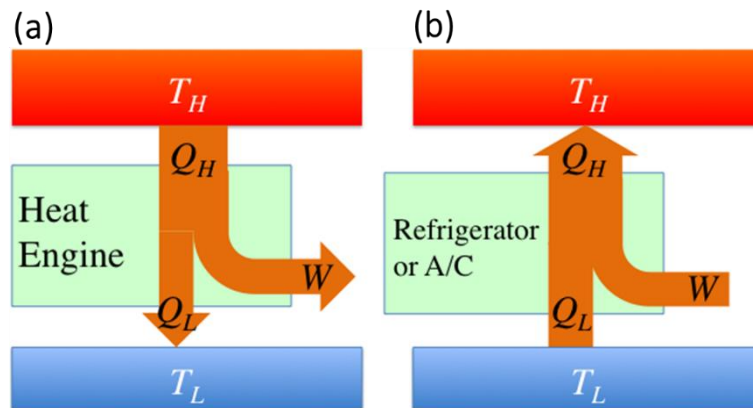
Figure 6.1 Illustration of heat flow in (a) heat engine and (b) heat pump (Reproduced from [9])

As indicated in Figure 6.2 (a), the reserved Carnot cycle is a counter clockwise with four steps. Refrigerant is used as an intermediate fluid in the reserved Carnot cycle application. From point 1 to 2, it is an isothermal process with a compression of the volume. During this process, the temperature is kept as a constant at high temperature therefore the internal energy of the refrigerant will not change during this process. According to the first law of thermodynamics, $\delta U = \delta W + \delta Q$. δU represents the internal energy of the

system; δW represents the work done by the system and δQ represents the heat added to the system. δU term in this process is zero, $\delta U=0$. Because of the decreasing of volume and the increasing of the pressure, work is done onto the refrigerant and δW term is positive ($\delta W>0$). Therefore, δQ is negative ($\delta Q<0$) which means the system release heat to the environment at high temperature. Corresponding to the process from point 1 to 2 in Figure 6.2 (b), entropy decreased and δS is negative. Thus it accompanies with negative δQ because $\delta Q=T \cdot \delta S$. From point to 2 to 3, it is an adiabatic process which means δQ is zero. Because the volume enlarges, this means the system output work to the environment and δW is negative ($\delta W<0$). Therefore, δU is also negative ($\delta U<0$) with decreasing of system temperature. This is also indicated in the Figure 6.2 (b) that the temperature decreases to low temperature from point 2 to 3. For the isothermal process from point 3 to 4, the system continuously expands with decreasing of pressure. This means δW term is negative ($\delta W<0$) during this process. The isothermal process limits the change of temperature and internal energy, therefore δU is zero for the system. According to first law of thermodynamics, δQ in this process is positive ($\delta Q>0$) which means the system absorb heat from environment. In the corresponding temperature-entropy diagram Figure 6.2(b), it is clearly that from point 3 to 4, the entropy increase to S_2 at low temperature point. Lastly step for the cycle from point 4 to 1, it is an adiabatic process with a decreasing of system volume. It is clearly that δQ is zero and δW is positive ($\delta W>0$) in this process. Therefore, δU is positive ($\delta U<0$) with increasing of system temperature, which is also shown in Figure 6.2(b). Overall, in the reversed Carnot cycle, the refrigerant absorbs heat ($\delta Q>0$) from environment at low temperature state (step 3 to 4). Thereafter, with the help of work (step 4 to 1), the system reaches to high temperature

state and then releases the heat ($\delta Q < 0$) to environment at high temperature. As a heat pump, the refrigerant bring heat from low temperature reservoir to high temperature reservoir countered to the temperature gradient.
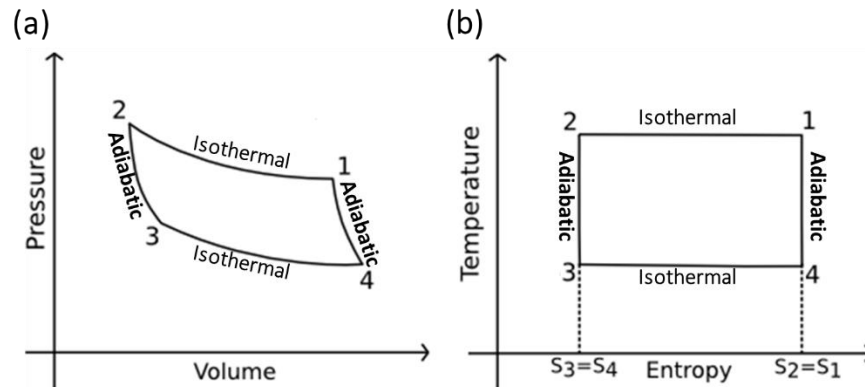
Figure 6.2 Reversed Carnot cycle (a) in a pressure and volume plot, (b) in a temperature and entropy plot (Reproduced from [9])

As we have described the reversed Carnot cycle in above, to accomplish the function of the heat pump, it need external work done upon the system. The external work can be mechanical work in mechanical heat pumps. The most important examples for mechanical heat pumps nowadays are refrigerator and air conditioner. The most common type of refrigerators out in market are vapor-compression refrigerator and the refrigerant are "Freon". Freon is a volatile evaporating and condensing fluid. Here in Figure 6.3, it is the illustration of the vapor-compression refrigeration cycle of a "Freon" based refrigerator: 1) condenser, 2) expansion valve, 3) evaporator, 4) compressor. The four steps indicated in Figure 6.3 are related to the process steps in the reversed Carnot cycle from point 1 to point 4 and then cycling back to point 1 again.

As indicated in Figure 6.3, the Freon in its hot gaseous state after pressurized by a compressor and circulated through the system, it experiences the isothermal process at high temperature occurred in condenser. In the condenser step 1, the refrigerant has heat exchange and releases heat to the environment. In the real refrigerator, this is a step that refrigerant exhausts heat obtained from the food in the freezer to the environment. The refrigerator is condensed into its liquid state as a hot liquid. The hot liquid flows into a pressure-lowering device such as expansion valve shown in Figure 6.3.[9] This is step 2 which is an adiabatic process without heat exchange. During this step, the high pressure hot refrigerant decrease its pressure and also temperature, which ends up to a low pressure cold liquid refrigerant. Such a liquid refrigerant then enters to another heat exchanger, the evaporator, and undergoes another isothermal process. For step 3 in evaporator, the liquid refrigerant absorbs heat from environment at constant low temperature and boils into gaseous state. This step in real refrigerator means the heat of food in the freezer is taken away and the food is cooling. Next, the gaseous state refrigerant returns to the compressor as step 4. The compressor increases the pressure of the gaseous refrigerant and applies work to the refrigerant. Therefore, during this adiabatic process, the internal energy of the refrigerant increases and the temperature elevates to high temperature state. At this moment, the refrigerant is at hot gaseous state as described at the beginning. Thereafter the hot gaseous Freon enters into condenser again and the cycle is repeated. Clearly, to bring heat from low temperature reservoir (food) to high temperature reservoir (environment) against the temperature gradient in this mechanical heat pump, mechanical work done by the compressor and condenser helps to achieve this task.
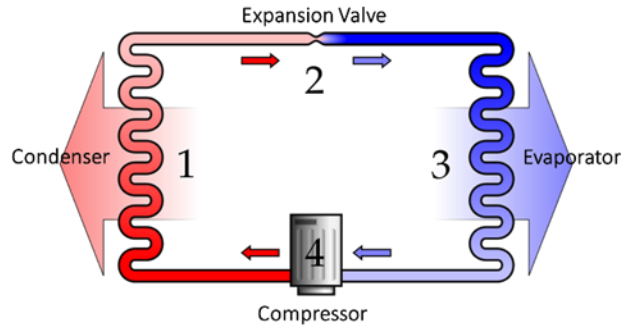
Figure 6.3 Illustration of the four working parts of the refrigerator. (Reproduced from [9])

However, the severe damage of "Freon" to the ozone and its huge volume inspired the exploration of another types of heat pump.[9] To realize heat flows against the temperature gradient, electrical or magnetic field can be the actor to perform the work. Solid state refrigeration based on electrocaloric effect (ECE) or magnetic-caloric effect is explored as new types of heat pump.[4-8]

6.1.2 Solid State Refrigerator Based on Electrocaloric Effect

As mentioned in previous section, a desired heat pump for refrigeration need to have temperature change and entropy change as shown in Figure 6.2 (b) to accomplish a reversed Carnot cycle as in Figure 6.2(a).[8] The electrocaloric effect (ECE) is the change in temperature and / or entropy of a dielectric material upon electrical field change. The change of electrical field induces the change of dipole states inside of the dielectric material. The dipole alignment upon electrical field and disorder because of releasing of electrical field corresponding to entropy and temperature change inside the materials system, which can be understood through a reversed Carnot cycle as shown in Figure 6.4.

104
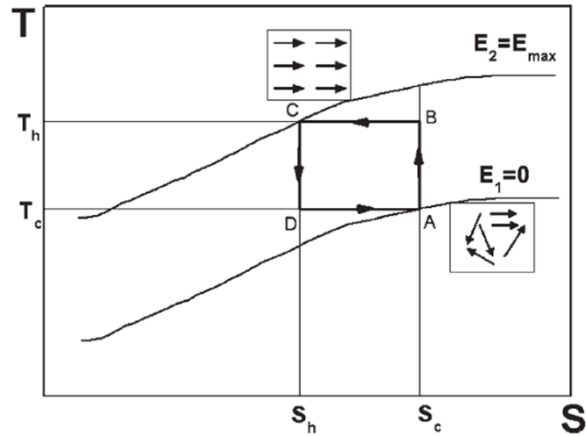
Figure 6.4 Thermodynamic refrigeration cycle based on electrocaloric effect(Reproduced from [8])

Starting from point A in Figure 6.4, dipoles in a dielectric material at that state without electrical field applied ($E_1=0$)are disorderly arranged. When the electrical field applies to the dielectric material as from A to B, the dipoles begin to align. Electrical field reaches to it maximum value at point B as E_2 ($E_2=E_{max}$). At the moment of turning on electrical field, there is no enough time for heat exchange ($\delta Q=0$). Typically, electrical fields stabilize quickly, and there is no enough time for heat exchange. Therefore, from A to B, it is assumed as an ideal adiabatic process without change of heat and entropy ($\delta S=0$). Because electrical field inputs electrical work to the dielectric material ($\delta W>0$), the temperature of the dielectric material rises to Th ($\delta U>0$). From point B to C, electrical field is maintained on the dielectric material and dipoles are aligned orderly inside of dielectric material. Therefore, the entropy of the system decreased ($\delta S<0$) and the system gives out heat to environment ($\delta Q<0$). As in real refrigeration application, from point B to C, the material in contact with a hot reservoir environment, during this step it is regarded as an isothermal process and the temperature of the system is kept at high

temperature state Th ($\delta U=0$). From point C to D, the electrical field is taken away ($E=E_1=0$) from the system and the system outputs work to environment ($\delta W<0$). Therefore during this moment, the system experiences an adiabatic process ($\delta Q=0$) with a decreasing of temperature ($\delta U<0$). Right at point D, the system is on low temperature Tc state. With the disappearing of the electrical field ($\delta W<0$), the order dipoles in dielectric material begin to relax and turn to disorder. Therefore, the entropy increases from point D to A ($\delta S>0$). In such a process, the dielectric material will contacted with a cold reservoir in the refrigeration application, therefore the temperature of the system is assumed to be constant Tc from D to A step ($\delta U=0$). During this step process, the dielectric material absorbs heat from cold environment as the evaporator step in Freon refrigerator. After returning to point A, the cycle continues in the manner as described above. Overall, the dielectric materials absorb heat at low temperature state. With the help of electrical work, the dielectric materials perform as a refrigerant exhaust heat to high temperature environment. Such an electrical heat pump also brings heat opposite to temperature gradient.

Comparing solid state electrocaloric cooling cycle and the typical vapor-compression refrigeration cycle which both are described in detail above, it is clear that the thermodynamics analysis are the same for both heat pumps. The differences are the refrigerant material and the work helps to move heat up-gradient.

For solid state electrocaloric cooling, we can analyze the electrocaloric effect based on Maxwell relations to calculate the entropy change (ΔS) and the temperature change (ΔT) of electrocaloric materials[4,6-8] which are represented as in the following equations 6.1 and 6.2.

$$\Delta S = -\int_{E_1}^{E_2} \left(\frac{\partial D}{\partial T}\right)_E dE \qquad\qquad \text{Equation 6.1}$$

$$\Delta T = -\frac{T}{\rho}\int_{E_1}^{E_2} \frac{1}{C_E}\left(\frac{\partial D}{\partial T}\right)_E dE \qquad\qquad \text{Equation 6.2}$$

Where D=displacement of the dielectric material sample under electric field

   E=electric field applied on the sample

   C_E=heat capacity of the dielectric material (specific heat)

   P=density of the dielectric material

The derivation of the equation 6.1 and 6.2 are shown below:

For a certain system, we have the first law of thermodynamics:

$$dU = TdS - PdV \qquad\qquad \text{Equation 6.3}$$

Where U is internal energy, P is pressure and V is volume; dU can be represents with

total differentials form: $dU = \left(\frac{\partial U}{\partial S}\right)_V dS + \left(\frac{\partial U}{\partial V}\right)_S dV$ Equation 6.4

Compared Equation 6.3 and 6.4, we know that T=$\left(\frac{\partial U}{\partial S}\right)_V$, P=$-\left(\frac{\partial U}{\partial V}\right)_S$,

Since we also know that for functions with continuous second derivatives, the mixed

partial derivatives are identical, that is: $\dfrac{\partial U}{\partial S}\dfrac{\partial U}{\partial V} = \left[\dfrac{\partial\left(\frac{\partial U}{\partial V}\right)_S}{\partial S}\right]_V = \left[\dfrac{\partial\left(\frac{\partial U}{\partial S}\right)_V}{\partial V}\right]_S$

Equation 6.5

After substituting the values of T and P,

We have so called Maxwell Relation: $\left(\frac{\partial T}{\partial V}\right)_S = -\left(\frac{\partial P}{\partial S}\right)_V$,   Equation 6.6

Similarly, for a dielectric material system in electrocaloric effect, we assume there is no mechanical work but only electrical work. We also assumed it is an unstrained system under adiabatic conditions in thermal equilibrium. Therefore, we have change of Gibbs free energy dG as

$$dG = -SdT - DdE, \hspace{2cm} \text{Equation 6.7}$$

Here, we have two variables electrical field and temperature which we can change during experiments.

Therefore, we will have Maxwell relation that: $\left(\frac{\partial S}{\partial E}\right)_T = -\left(\frac{\partial D}{\partial T}\right)_E$.

Therefore, from above Maxwell relation, we know that

$$\Delta S = -\int_{E_1}^{E_2} \left(\frac{\partial D}{\partial T}\right)_E dE \hspace{1cm} \text{Equation 6.1}$$

Also we know that $\Delta Q = \Delta T \bullet (C_E \bullet \rho)$, and $\Delta Q = T \bullet \Delta S = T \bullet \left[-\int_{E_1}^{E_2} \left(\frac{\partial D}{\partial T}\right)_E dE\right]$,

Finally we get that: $\Delta T = -\frac{T}{\rho}\int_{E_1}^{E_2} \frac{1}{C_E}\left(\frac{\partial D}{\partial T}\right)_E dE$ Equation 6.2

Therefore, with help of equation 6.1 and 6.2, also long as we measure the displacement change with electrical field and temperature, we can estimate the entropy and temperature change of the dielectric electrocaloric effect based refrigerator. Based on equations 6.1 and 6.2, we can analyze that a large polarization change with is always desirable in order to achieve a large ECE, ferroelectric materials particularly ferroelectric ceramics with

very high polarization are a type of candidates for developing solid state refrigerator base electrocaloric effect. Meanwhile, a high breakdown field is demanding to harvest large ECE entropy and temperature change. Therefore, ferroelectric polymers with high breakdown field are also excellent candidates as well. Furthermore, it is necessary to understand the correlation between the EC effect entropy change and polarization change under an applied electric field. Beyond the requirement of high polarization and high dielectric strength, to get a large EC effect with a large entropy change, it is very beneficial when operating the material just above its ferroelectric to paraelectric transition temperature (Cuire temperature, Tc) thus the large polarization changes can be achieved. The EC effect is the strongest at the transition temperature and it decreases gradually as the system enters the paraelectric state.

6.1.3 Electrocaloric Effect Materials used for refrigeration

In this section, we focused on the materials aspect to review the types of ferroelectrics materials, their performance in EC effect based solid state refrigerator development and then point out our research focus and design rules.

Ferroelectric materials are a kind of dielectric materials which show ferroelectric properties such as a spontaneous polarization on cooling below the Curie point, ferroelectric domains and a ferroelectric hysteresis loop. Basically there are two groups of ferroelectrics: ferroelectric ceramics and ferroelectric polymers.[4] Barium titanate (BaTiO$_3$) based ceramics is a large group of ferroelectric ceramics including lead titanate (PbTiO$_3$), lead zirconate titanate (PZT), and lead lanthanum zirconate titanate (PLZT). This group of ferroelectrics all has BaTiO$_3$ style crystals structure as shown in Figure

6.5.[10] The spontaneous polarization is a consequence of the positioning of the Ba^{2+}, Ti^{4+}, and O^{2-} ions within the unit cell. The Ba^{2+} ions are located at the corners of the unit cell, which is of tetragonal symmetry (a cube that has been elongated slightly in one direction). The dipole moment results from the relative displacements of the O^{2-} and Ti^{4+} ions from their symmetrical positions as shown in the side view of the unit cell. The O^{2-} ions are located near, but slightly below, the centers of each of the six faces, whereas the Ti^{4+} ion is displaced upward from the unit cell center. Thus, a permanent ionic dipole moment is associated with each unit cell. For the group of ferroelectric ceramics, usually they own very high dielectric constant, very small dielectric loss but low dielectric strength.[11]
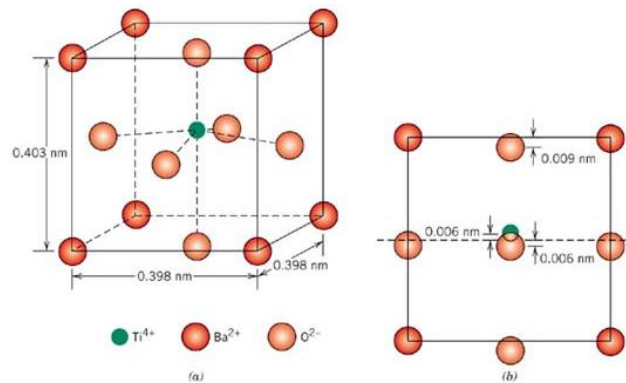
Figure 6.5 A barium titanate ($BaTiO_3$) unit cell (a) in an isometric projection, and (b) looking at one face, which shows the displacements of Ti^{4+} and O^{2-} ions from the center of the face. (Reproduced from [11])

The representative of ferroelectric polymers are polyvinylidene fluoride(PVDF) and PVDF based copolymers and terpolymers. PVDF exists in several forms: alpha (α, TGTG'), beta (β, TTTT), and gamma (γ, TTTGTTTG') phases, depending on the chain conformations as trans (T) or gauche (G) linkages.[3] In Figure 6.6, it shows the alpha

110

and beta phase of PVDF. Clearly, PVDF polymers with β phase crystalline state have large dipole moment because all F atoms are arranged on the same side and dipoles cannot cancel each other as in α or γ phase. The glass transition temperature (Tg) is around -35°C with 50-60% crystalline. To give the material its piezoelectric properties, it is mechanically stretched to orient the molecular chains and then poled under tension. Regarding the dielectric properties of PVDF based ferroelectric polymers, they always have high dielectric strength and reasonable large dielectric constant but also high dielectric loss.
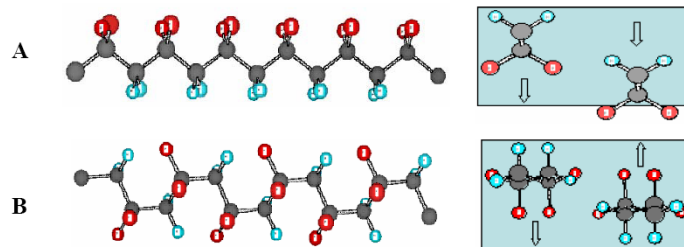
Figure 6.6 The molecular conformations and lattice structures of (A) β, beta-phase and all trans conformation and (B) α, alpha-phase and TGTG' conformation for PVDF. (Reproduced from [3])

The application of both ferroelectric ceramic and ferroelectric polymer in the EC effect based refrigeration has been studied intensively.[12-20] In the following tables, it is the reported EC characteristics of various ceramics thin films and various ferroelectric polymer films as in table 6.1.[6] As indicated in the tables, both the ferroelectric ceramic thin films and the ferroelectric polymer films are able to have temperature change around a few to ten degree Celsius. Such a dramatically change on temperature predict the potential of both types materials in real refrigeration application. Therefore, based on the

current state of art, we would like to make ferroelectric composite with both ceramics and polymer to try to overcome their disadvantages and harvest their strong point to try to improve the electrocaloric effect of the composite.

Table 6.1 Materials and characterization summary for electrocaloric effects. (Reproduced from [6]), IM means indirect method obtained experiment value; DIR means direct reading temperature.

Reported EC characteristics of polymer films.

Material	Thickness of the film (μm)	T (°C)	ΔT (°C)	ΔE (MV/ m)	$\Delta T/\Delta E$ (10^{-6}m K/V)	Measur. method
P(VDF–TrFE) 55/45	0.4–2	80	12.6	209	0.06	IM
P(VDF–TrFE) 55/45	4–7	67	12	120	0.10	DTR
Irradiated P(VDF–TrFE) 68/32	10–15	33	20	160	0.125	DTR
P(VDF–TrFE) 68/32	0.4–6	70	2	50	0.05	DTR
P(VDF–TrFE) 70/30	0.09	117	21	300	0.07	IM
P(VDF–TrFE–CFE) 59.2/33.6/ 7.2	7	30	15	150	0.10	DTR
P(VDF–TrFE–CFE) 59.2/33.6/ 7.2	0.4	55	12	307	0.04	IM
P(VDF–TrFE–CFE) 56.2/36.3/ 7.6	0.09	77	21	350	0.06	IM
P(VDF–TrFE–CFE) 56.2/36.3/ 7.6 annealed	1	45	9	300	0.03	IM
P(VDF–TrFE–CFE) 56.2/36.3/ 7.6 quenched	1	45	5	300	0.02	IM
P(VDF–TrFE–CFE)$_{0.9}$–P(VDF– TrFE–CTFE)$_{0.1}$	4–6	45	6	120	0.05	DTR

Reported EC characteristics of thin films.

Material	Deposition method	Thickness of the film (nm)	T (°C)	ΔT (°C)	ΔE (MV/m)	$\Delta T/\Delta E$ (10^{-6}m K/V)	Measur. method
PbZr$_{0.95}$Ti$_{0.05}$O$_3$	Sol–gel	350	222	12	48	0.25	IM
PbZrO$_3$	Sol–gel	700	235	11.4	40	0.29	IM
(Pb$_{0.88}$La$_{0.08}$)(Zr$_{0.65}$Ti$_{0.35}$)O$_3$	Sol–gel	450	45	40	125	0.32	DTR
(Pb$_{0.97}$La$_{0.02}$)(Zr$_{0.95}$Ti$_{0.05}$)O$_3$	Sol–gel	1700	210	8.5	110	0.08	IM
PbZr$_{0.52}$Ti$_{0.48}$O$_3$ $\langle 001 \rangle$	PLD	260	387	11.1	57.5	0.19	IM
PMN-PT 65/35	PLD	240	140	31	74.7	0.41	IM
PMN-PT 67/33 no buffer layer	PLD	430	235	2.13	11.6	0.18	IM
PMN-PT 67/33 buffer layer	PLD	430	235	4.25	11.6	0.37	IM
PMN-PT 67/33 $\langle 001 \rangle$	RFMS	200	145	14.5	60	0.24	IM
PMN-PT 68/32 $\langle 100 \rangle$	RFMS	200	146	13.4	60	0.22	IM
PMN-PT 90/10	Sol–gel	260	60	5	96	0.05	IM
PMN-PT 93/07	Sol–gel	210	25	9	72	0.13	IM
PbSc$_{0.5}$Ta$_{0.5}$O$_3$	Sol–gel	200	70	6.9	77.4	0.09	IM
SrBi$_2$Ta$_2$O$_9$	Sol–gel	200	288	4.93	60	0.08	IM

6.1.4 Requirements for the composite system

As we planned to make polymer-metal oxide (PVDF-BaTiO$_3$) nanocomposites, we would like to first understand the requirements for the composite in order to harvest the strong points from both materials to improve the EC effect.[21-27] Obviously, the volume fraction of the nanofillers (BaTiO$_3$ nanoparticles) in the composite will play a very important role in the properties of the composite systems. If the nanofillers volume fraction is too low, it won't give out high dielectric constant and also won't lower the dielectric loss because the polymer feaction is still large amount. Therefore, there will be a certain threshold above which the composite can have high dielectric constant, high dielectric strength with low loss. Oppositely, if the nanofillers volume fraction is too high, the existence of large amount of low dielectric strength nanofillers will decrease the dielectric strength of composite apparently.[25] Also, the air voids in the composite will be very harmful to the dielectric strength of composite either because the dielectric breakdown field of air is very low. Based on the analysis above, people already done a lot of simulation works together with experimental proves, the good volume fraction for nanofillers to give out high dielectric constant is from 50% to 60%. From the dielectric loss point of view, the higher volume fraction of nanofillers, the lower dielectric loss. When the volume fraction reaches to 80%, the dielectric loss will be small. When thinking about the dielectric strength requirement, there is two percolation points. One is volume fraction of nanofillers in the range of 10% to 20%. In this range, the charge conduction along the percolative pathways can occur which accelerates the breakdown. This bad effect can be reduced through surface modification towards nanofillers. When there is insulator surfactant coating on the surface of nanofillers, the first percolative can

be suppressed effectively. The second critical volume fraction value is 50%. When the volume fraction of nanofiller is larger than 50%, there will be air voids formed in the nanocomposite system, which will reduce the dielectric breakdown voltage apparently. Also, as we hope to use the composite as capacitor materials, we need to think about the right volume fraction from the energy density side. Theoretically calculation predicts that both 10% and 50% volume fraction of nanofillers will give out the highest energy density. Experimentally data shows that 50% volume fraction can give the maximum energy density in BaTiO3-PVDF composite system. Therefore, based on all different fours aspects consideration, 50% by volume of nanofillers in composite should give out the best dielectric performance.[22, 25] In table 6.2, it shows a brief summary of the nanofillers volume fraction range requirements for each individual dielectric parameters and also the combined best designed range.

Table 6.2 Summary of the nanofillers volume fraction range requirements vs dielectric parameters (summarized and reproduced [22])

Dielectric Parameter	Nanofiller Volume fraction range	Reason Analysis
Dielectric constant	50%-60%	When the nanofiller volume fraction is larger than 60%, the air voids formed (when volume fraction larger than 50%) in composite will limit or decrease ε_r.
Dielectric strength	< or =50%	When the nanofiller volume fraction is larger than 50%, the nanofillers cannot relax which lead to air voids to decrease breakdown voltage.
Dielectric loss	Larger, better	Nanofiller has very low dielectric loss. Basically, polymer PVDF has large dielectric loss due to so called resonance effect of PVDF polymer host. Therefore, the lesser of polymer, the better.
Energy density	10% or 50%	This is based on calculation. Experimentally, at 50% of nanofillers, it can have maximum energy density.
Combined	Around 50%	Based on all above four rules, 50% volume fraction of nanofillers in polymer-nanoparticles (PVDF-BaTiO$_3$) composite can give

		high dielectric constant, high breakdown field, low dielectric loss and high energy density dielectric material. In order to have less percolation effect, surfactant can be used to insulate nanoparticles. Also, in order to lower the effect of air voids, thermal treatment (annealing) can be used to relax the composite and prevent air voids. In the case, the volume fraction can be higher to give less dielectric loss.

After reviewing the mechanism of electrocaloric effect based solid state refrigeration and their materials development requirement in previous paragraphs, we would like to report our work on making ferroelectric ceramic-polymer composite, our efforts on direct measurement temperature change of PVDF polymer thin film refrigeration device and our achievements in fabricating integration electrocaloric effect based refrigeration device in the following sections.

6.2 Synthesis and Characterization of Ferroelectric Ceramic Nanoparticles

6.2.1 Synthesis of $BaTiO_3$ and $SrTiO_3$ serials nanoparticles

As a group of important ferroelectric ceramics, the synthesis of nano-size $BaTiO_3$, $SrTiO_3$ and $Ba_{1-x}Sr_xTiO_3$ nanoparticles was the first task here. The hydrothermal synthesis is based on the method from Shiva Adireddy et al.[28] In a typical procedure for the preparation of cube-like nanoparticles, different solutions containing 1 mmol of $Ba(NO_3)_2$ dissolved in 5 mL of deionized water, 10.8 mmol of KOH dissolved in 5 mL of deionized water, 1 mmol of $Ti(Bu)_4$ dissolved in 5 mL butanol (BuOH) and 2.5 mL of oleic acid in 5 mL of BuOH were mixed together and the resulting solution subsequently transferred to a 23 mL Teflon-lined stainless steel autoclave. The autoclave was sealed and was subsequently heated to 135℃ for 16 hours. After the completion of the reaction, the reaction mixture was cooled naturally to room temperature and separated from the

supernatant solution by centrifugation. The precipitate was collected, washed with acetone, water and acetone consequently and eventually dispersed in toluene yielding a stable milky colloidal solution. For the synthesis of $SrTiO_3$ and $Ba_{0.5}Sr_{0.5}TiO_3$, exactly the same procedure was applied with related different staring materials. The summary of different synthesis starting materials was listed in table 6.3.

Table 6.3 Summary of synthesis starting materials for $BaTiO_3$ and $SrTiO_3$ serials nanoparticles.

Nanocrystal	Ba(NO₃)₂	Sr(NO₃)₂	KOH	H₂O	Ti(O-Bu)₄	Oleic Acid	BuOH
$BaTiO_3$	1mmol	None	10.8	10	340μL	2.5mL	10mL
$Ba_{0.75}Sr_{0.25}TiO_3$	0.75mmol	0.25mmol	mmol	mL	340μL	2.5mL	10mL
$Ba_{0.5}Sr_{0.5}TiO_3$	0.5mmol	0.5mmol			340μL	2.5mL	10mL
$SrTiO_3$	None	1mmol			340μL	2.5mL	10mL

All nanoparticles was characterized through X-ray diffraction to make sure the nanoparticle we synthesized are on the demanding crystalline structures and phases. Transmission electron microscope (TEM) was used to determine the size of the synthesized nanoparticles.

In the following Figure 6.7, 6.8 and 6.9, there are XRD figures and TEM images for $BaTiO_3$, $Ba_{0.5}Sr_{0.5}TiO_3$ and $SrTiO_3$.
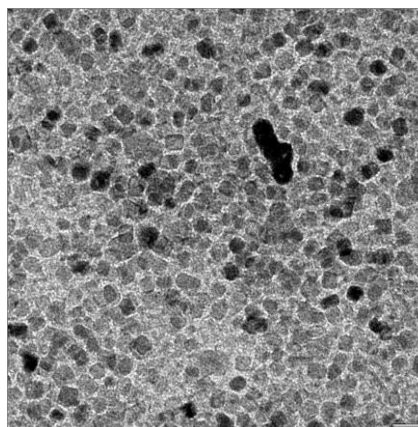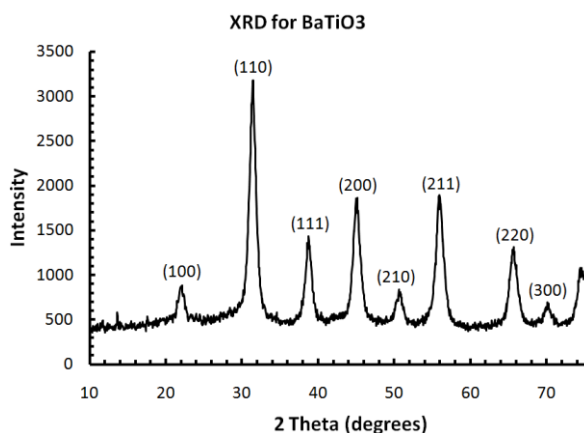
Figure 6.7 XRD figure and TEM image (right) prove the synthesized nanoparticles is $BaTiO_3$ and the crystalline sized is around 8-10nm. The scale bar in the TEM image is 20nm.

XRD for Ba0.5Sr0.5TiO3
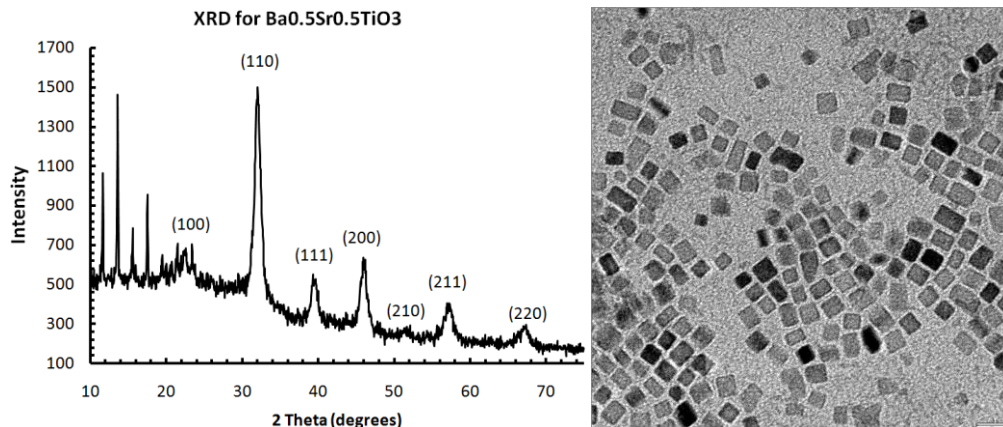
Figure 6.8 XRD figure and TEM image (right) prove the synthesized nanoparticles is $Ba_{0.5}Ti_{0.5}O_3$ and the crystalline sized is around10-12nm. The scale bar in the TEM image is 20nm.

XRD for SrTiO3
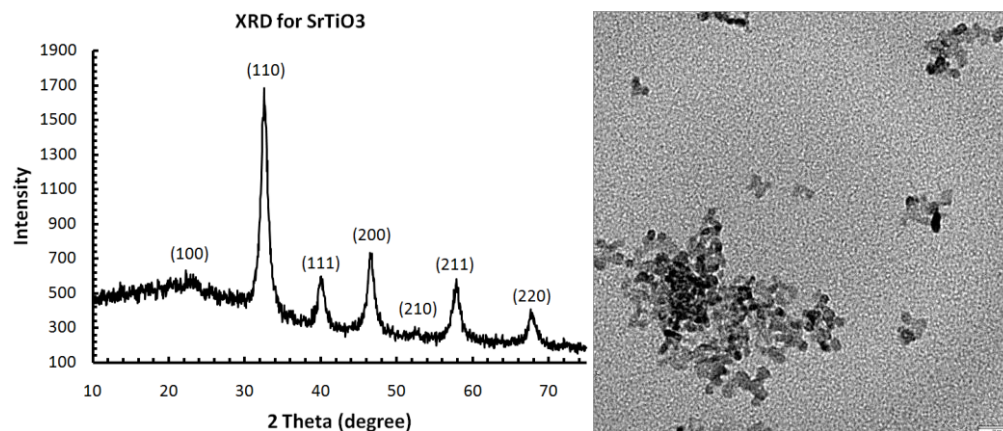
Figure 6.9 XRD figure and TEM image (right) prove the synthesized nanoparticles is Sr TiO_3 and the crystalline sized is around 8nm. The scale bar in the TEM image is 20nm.

As we can see from the above, the XRD shows that all three materials form very good crystals with clear peaks shown. The unlabelled very sharp peaks in $Ba_{0.5}Sr_{0.5}TiO_3$ XRD figure (in 10 to 20 degree of 2θ range) are due to the residual salt. Further washing can

remove that salt and remove those peaks from the XRD figure. From the TEM images we can see for $BaTiO_3$, it form cube crystal at size around 8-10 nm but the shape is not very sharp. For $Ba_{0.5}Sr_{0.5}TiO_3$, although the size is larger at around 10-12nm but it forms very good cube crystal with sharp edges. For SrTiO3, the size is smaller at around 8nm but the shape is not cubic and not very regular.
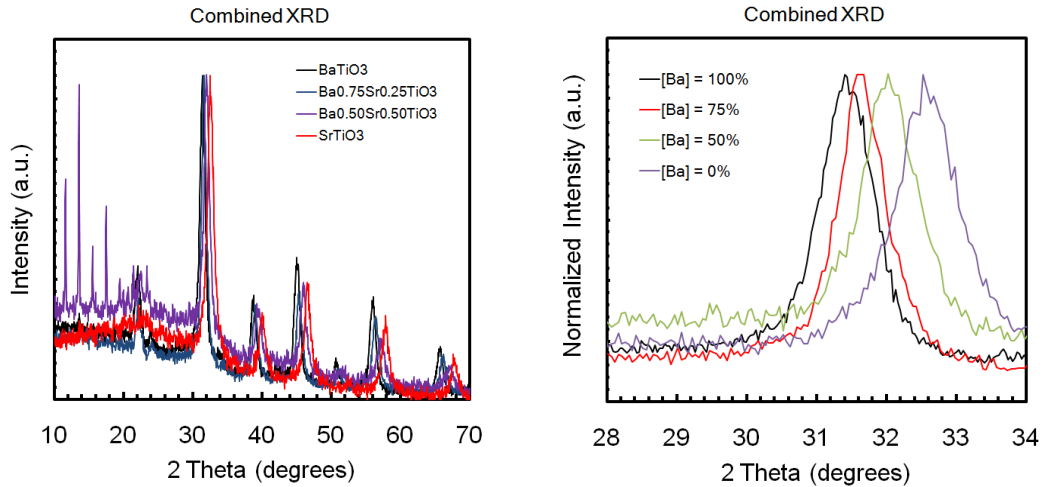
Figure 6.10 Combined XRD peaks show the peak shift due to the changing of [Ba] relative amount

The XRD Peak shift with the changing of amount of [Ba] concentration in $Ba_{1-x}Sr_xTiO_3$ serials nanocrystals has been studied very well by Kai Su et al. It is proved that, with the increasing of amount of [Sr] and decrease amount of [Ba], all the XRD peaks will shift to larger 2θ value. To check the peak shift in our synthesized nanoparticles, we synthesized both $Ba_{0.75}Sr_{0.25}TiO_3$ and $Ba_{0.5}Sr_{0.5}TiO_3$ nanoparticles for comparison. In Figure 6.10, our experimental XRD result show very well peak shift matched with their study. The right side figure show a more clear version of (110) peak shift with the decreasing of [Ba] amount.

6.2.2 Synthesis Smaller Size BaTiO$_3$ nanoparticles

Synthesizing nanoparticles with diameters equal to a single ferroelectric domain is reported to be able to minimum the hysteresis and dielectric losses. Therefore, we tried to tune the synthesis conditions to decrease the size of BaTiO$_3$ nanoparticles. Here in table 6.4, it is a summary of different approaches we tried to achieve our aim together with the description of the results.

Table 6.4 Summary of Different Synthesis Approaches and Results for Synthesizing Smaller Size BaTiO$_3$ Nanoparticles

Methods List	Changed Factors	Results Description
I	Decrease KOH amount (1:11) to KOH (1:8.5) or (1:9.5)	The product checked from XRD only gives out amorphous products.
II	Short reaction time to 8 hrs	From XRD, we can clearly see the peaks from BaTiO3 crystals. But there are also very high intensity sharp peaks from the residual salts. Short reaction time may not be able for the decomposition complete.
III	Add 2.6 ml (another 8mmol oleylamine as co-surfactant	From XRD, we have clear peaks from BaTiO3 crystals. From TEM, it shows great cubic shape nanocrystals with size around 7-8nm. The TEM image and XRD figures will be given below.
IV	Use less amount of Ti(Bu)$_4$ (280 μL) and add co-surfactant as in method III	Check from XRD and TEM, the BaTiO3 nanoparticles have the right crystalline phase with good cubic shape at size around 6-8nm.
Note: Only the changed reaction condition is listed as "changed factor", all other reaction conditions including the amount / ratio of the starting materials, reaction temperature and time are kept the same as previous standard method.		

In the following Figure 6.11, it is show the TEM images for BaTiO$_3$ nanoparticles synthesized through our tuned methods III (co-surfactant) and IV (less Ti precursor). The size decreased to around 6-8nm with regular cube shape as shown in figure 6.11.
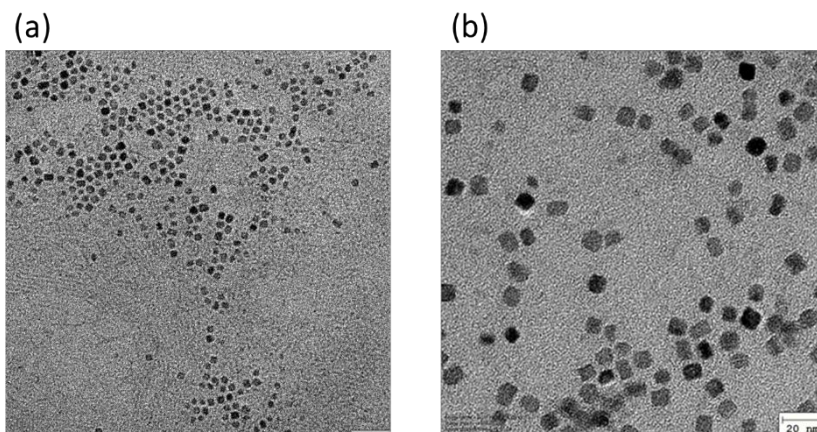
Figure 6.11 TEM image for synthesized nanoparticles BaTiO$_3$ with method III (image a, the scale bar is 40nm) and IV (image b, the scale bar is 20nm) listed in table 6.4.

The effect of co-surfactant of oleylamine on decreasing the particle size can be regarded as effectively coating on and then stopping the ongoing growth of the crystalline. The decreasing of the size due to this mismatch [Ba] to [Ti] precursor is understood based the formation mechanism of the nanoparticles. Generally, the formation of nanoparticles from the solution involves two processes: the nucleation and growth of nuclei. It is known that rapid nucleation relative to the growth results in small and mono-dispersed particle size which is as for our synthesized BaTiO$_3$. A solution is kept at about the minimum concentration of nucleation. If the solute in a solution is consumed by the formation of nuclei, the concentration decreases below the minimum concentration of nucleation and no nucleation can occur. Therefore, the mono-dispersion of the crystalline size is achieved. For less [Ti] precursor to decrease the crystalline size, it can be understood as excess Ba^{2+} can prevent the particles coarsening. Excess Ba^{2+} may limit the dissolution/precipitation of existing BaTiO$_3$ nanoparticles. [29-35]

6.2.3 6-8 nm BaTiO$_3$ Nanoparticles Dielectric Properties Characterization

The dielectric properties of the BaTiO$_3$ 6-8 nm nanoparticle we measured with the Precision RT66B tester from Radiant Technology Inc. This equipment can provide various types of measurement typically for ferroelectric materials. Here for our measurement, we made high pressure compressed BaTiO$_3$ nanoparticles pellet sample with around 3mm in diameter and 0.8mm in thickness for hysteresis test. After pressed the sample, a layer around 100nm gold was sputtered on both sides of the pellet as electrodes to form a parallel plate capacitor. We didn't sinter the nanoparticles pellet as people traditionally in this type of measurement as we want to mimic the real case that the nanoparticles were wrapped with organic ligands and dispersed in the polymer matrix in the composite. The BaTiO$_3$ nanoparticle capacitor was measured with RT66B tester at 750V with 100millisecond hysteresis time. The polarization verse applied electrical filed curves for BaTiO$_3$ is given in Figure 6.12 (a) together with the leakage current record for the same sample as in Figure 6.12(b).
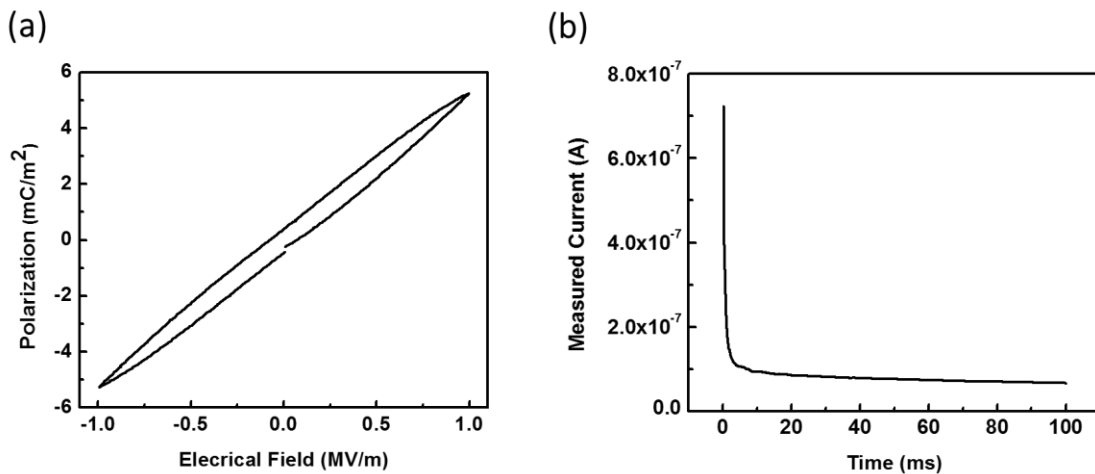
Figure 6.12 (a) Measured polarization vs electrical field relationship for BaTiO$_3$ nanoparticle and (b) the leakage current measured as the same P-E curve testing condition for the same sample.

As we can see from Figure 6.12 (a), the polarization P is almost proportional to the applied external electric field. The hysteresis loop is also very narrow. To estimate the dielectric constant (ε_r) of this BaTiO$_3$ nanoparticles, we can calculated it from the equation 6.8: $P = \varepsilon_0(\varepsilon_r - 1) \bullet E,$ where P is electrical field induced polarization, ε_0 is vacuum permittivity as 8.86×10^{-12}F/m and E is the applied electrical field. Reading from the Figure 6.12 (a), when E is 0.99MV/m, P is 5.26mC/m^2. Therefore, the dielectric constant of BaTiO$_3$ is calculated as 595. If we calculated the cost of charge to reach to the maximum polarization value 5.26mC/cm^2, it is 1.68×10^{-7} C. As we can integrated from the leakage current curve Figure 6.12(b), the charge involved in this process as leakage is 8.15×10^{-9}C. Therefore, the leakage of the capacitor has negligible influence (<5%) on the value of the dielectric constant. To understand the relatively low value of the dielectric constant of BaTiO$_3$, it is reasonable because the BaTiO$_3$ synthesized at size 6-8 nm is on perovskite cubic phase instead of the ferroelectric tetragonal phase. The crystals loss the tetragonal crystalline structure distortion due to the very high surface energy at nano size. Such a theory has been well studied through simulation and be proved experimentally.[29] Therefore, cubic phase BaTiO$_3$ with dielectric constant as 595 is reasonable.

Based on the analysis of BaTiO$_3$ nanoparticles dielectric performance, we are aware that to obtain tetragonal phase ferroelectric nanoparticles for our electrocaloric effect application, we need to focus on Ba$_{1-x}$Sr$_x$TiO$_3$ serials nanoparticles because it was

reported that Sr substitution into BaTiO$_3$ produces a stable tetragonal distortion of the structure, yielding a higher dielectric constant relative to the cubic structure and lowering the Curie Temperature T$_C$ of the oxide system with T$_C$ reaching room temperature at about x = 0.4 for Ba$_{1-x}$Sr$_x$TiO$_3$. Such a type of nanoparticle with high dielectric constant and low Tc should match our composite requirements more. Therefore, in the composite making section, we focus on the using Ba$_{0.65}$Sr$_{0.35}$TiO$_3$ nanoparticles with fluorinated tail to composite with PVDF polymers to make our composite device for direct electrocaloric effect measurement. The dielectric constant temperature dependence relationship for the Ba$_{0.65}$Sr$_{0.35}$TiO$_3$ we used is given as in Figure 6.13.It is clear the Ba$_{0.65}$Sr$_{0.35}$TiO$_3$ nanoparticles with a temperature dependent dielectric constant ensures its ferroelectric materials character. The Curie temperature Tc is about 20°C with dielectric constant near 1000 at Tc temperature.
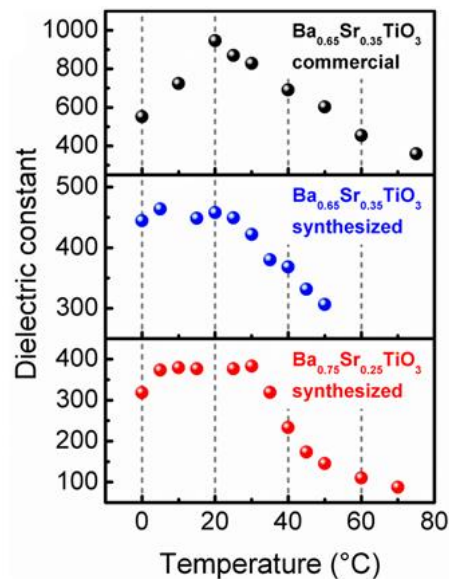
Figure 6.13 Plot of dielectric constant as a function of temperature on commercial Ba$_{0.67}$Sr$_{0.33}$TiO$_3$ NPs and synthesized Ba$_{1-x}$Sr$_x$TiO$_3$.

Overall, we have successfully developed the method to synthesized 6-8 nm BaTiO$_3$ nanoparticles and also a general way to synthesis Ba$_{1-x}$Sr$_x$TiO$_3$ serials of nanoparticles with size around 10-12nm.

6.3 Development and Characterization of Polymers Matrix for Electrocaloric Effect Composite Fabrication

6.3.1 Selection of Polymers Matrix

Various polymer materials have been investigated in order to identify a suitable polymer as the matrix for the synthesis of the nanocomposites.[7, 36-46] The requirements for a suitable polymer are: 1) high polarization and 2) capable of infiltration for our final device fabrication. We focused on two main groups of materials: 1) polymerizable vinyl monomer with high polarization and 2) ferroelectric polymers. Polymerizable monomers are small molecules so that they can diffuse fast and easily infiltrate into 3D interdigitated parallel electrode plates. Ferroelectric polymers have high polarization and energy density. In table 6.5, it summarizes dielectric properties of the polymers we investigated.

Table 6.5: Summary of Dielectric Characterization of Different Potential ECE Polymers

Dielectric Properties	PtBA	PnBA	P(VDF-TrFE) Copolymer	P(VDF-TrFE-CFE) Terpolymer
Polarization Max	21 (μC/m^2)	10 (μC/m^2)	84 (μC/m^2)	78 (μC/m^2)
Dielectric Constant	5.42@300MV/m	6.0	12.99@ 6MV/m 39.56@ 300MV/m	High @ low field 13.37@360MV/m
Breakdown Field (MV/m)	300	222	360	360
Releasing Energy Density	2.16 (J/cm^3)	2.7 (J/cm^3)	2.98 (J/cm^3)	7.89 (J/cm^3)

We formulated PtBA and PnBA polymers based on t-butyl acrylate and n-butyl acrylate monomers, respectively. Although their low polarization implies low electrocaloric effects, they are good matrix candidates for hybrid materials as mentioned above. We also have found two polymers (P(VDF-TrFE) copolymer and P(VDF-TrFE-CFE) terpolymer with a polarization around 80 mC/m^2 at 300 MV/m or above. The two PVDF based polymers with similar dielectric constants and breakdown strengths but their released energy densities are very different. The detailed comparisons of the ferroelectric properties of PVDF based polymers are listed in Table 6.6

Table 6.6 Comparison of the Dielectric Properties of P(VDF-TrFE) Copolymer and P(VDF-TrFE-CFE) Terpolymer

Compared dielectric properties	P(VDF-TrFE) Copolymer	P(VDF-TrFE-CFE) Terpolymer
Hysteresis Loop	Broad Hysteresis Loop	Narrow Hysteresis Loop
Highest Polarization	84 μC/m^2	78 μC/m^2
Releasing Energy Density	2.98 J/cm^3	7.90 J/cm^3
Energy Loss	10.52 J/cm^3	2.24 J/cm^3
Total Energy Input	13.50 J/cm^3	10.13 J/cm^3
Efficiency (releasing/input)	22.1%	77.9%

The dielectric data listed in above tables was measured with the Precision RT66B tester from Radiant Technology Inc. and then calculated from the corresponding polarization-electrical field curves. For the measurement samples, they were thin film parallel plate capacitor with 1.1 cm^2 working area and thickness around 1μm. The polymer films for

PtBA and PnBA were prepared through in-situ polymerization on ITO substrate under UV light. The PVDF copolymer and terpolymer thin films were form through spinning coating on ITO substrate from 10-15wt% polymer in DMF soultion. After getting the polymer film, the top electrodes for all polymer thin film capacitors were vacuum evaporated Al electrode with 200nm Al thickness. Thus capacitor samples for hysteresis properties were ready for testing. All the hysteresis test samples in the following 6.3.2 section were prepared through the same way as above.

In the following Figure 6.14, it shows the measured hysteresis loop of both P(VDF-TrFE) copolymer and P(VDF-TrFE-CFE) terpolymer.
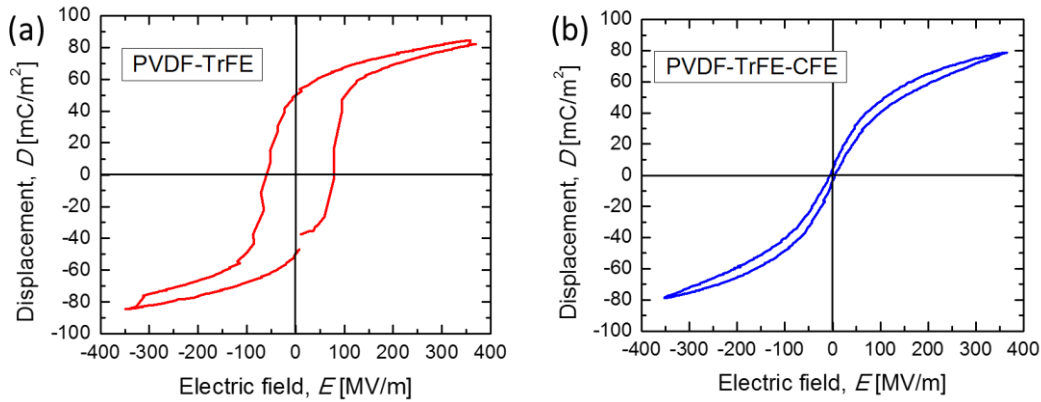
Figure 6.14 Hysteresis loop for P(VDF-TrFE) copolymer and P(VDF-TrFE-CFE) terpolymer

As seen, both P(VDF-TrFE) copolymer and P(VDF-TrFE-CFE) terpolymer have similar polarization values (~80 $\mu C/m^2$) and electric breakdown strength (~360 MV/m), however the shape of the hysteresis loop is different. P(VDF-TrFE) copolymer has a broad hysteresis loop and therefore relatively high remanent polarization (~50 $\mu C/m^2$) leading to high energy loss and efficiency of 22.1%. P(VDF-TrFE-CFE) terpolymer is known as

126

a relaxor ferroelectric due to the narrow hysteresis loop. For this material the dipoles are randomly oriented displaying no polarization at 0 MV/m and can be oriented very fast to achieve high levels of polarization leading to efficiency of 77.9%. The different ferroelectric performance of the two polymers can be understand through their microstructure. As PVDF based polymers are always semi-crystalline, for the crystalline regions, usually it is composed by TTTT all trans molecule configuration domains and connected through TGTG' configuration molecules chains. For P(VDF-TrFE) copolymer, it forms large domain but for terpolymer, due to the existence of CFE molecules, it form small domains. The smaller domains are much more easily to flip under electrical field. Also, the smaller domains are hard to hold their position and easy to relax under reverse electrical field.[7, 8] Therefore, terpolymer shows narrower hysteresis loop and also low "turn off" voltage.

6.3.2 Electrocaloric Effect Study on P(VDF-TrFE) Copolymer and P(VDF-TrFE-CFE) Terpolymer

As proven in previous comparison, P(VDF-TrFE) copolymer and P(VDF-TrFE-CFE) terpolymer with large polarization and large breakdown filed were selected as the candidate to make the composite ECE material. Therefore, in this section, we detailed studied the electrocaloric effect of PVDF based two polymers as followed.

As we reviewed in 6.1.2 section, to harvest the largest electrocaloric effect, temperature measurement should be done around the Curie temperature. Therefore, differential scanning calorimetry (DSC) measurement was used measured the Curie temperature (Tc) for both P(VDF-TrFE) copolymer and P(VDF-TrFE-CFE) terpolymer. In Figure 6.15, the

DSC curves show that P(VDF-TrFE) has Curie temperature at 63⁰C and P(VDF-TrFE-CFE) has low Curie temperature at 47.5⁰C.
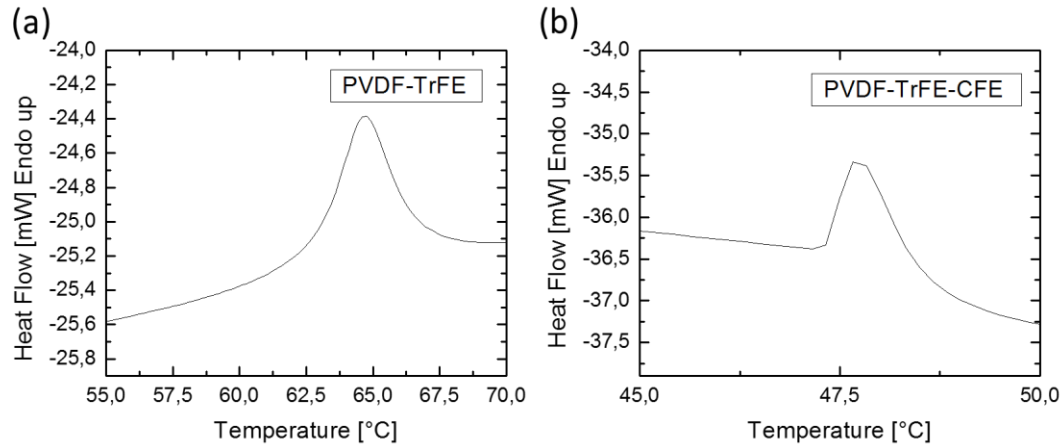
Figure 6.15 DSC figures for P(VDF-TrFE) copolymer (a) and P(VDF-TrFE-CFE) terpolymer (b)

To theoretically analysis the electriccaloric effect of the P(VDF-TrFE) copolymer, we measured the hysteresis loops of P(VDF-TrFE) copolymer under different temperatures at maximum electric field of 300 MV/m at 10 Hz as shown in Figure 6.16. The samples for hysteresis measurement were thin film parallel plate capacitor with 1.1 cm^2 working area and 0.8 µm thickness.
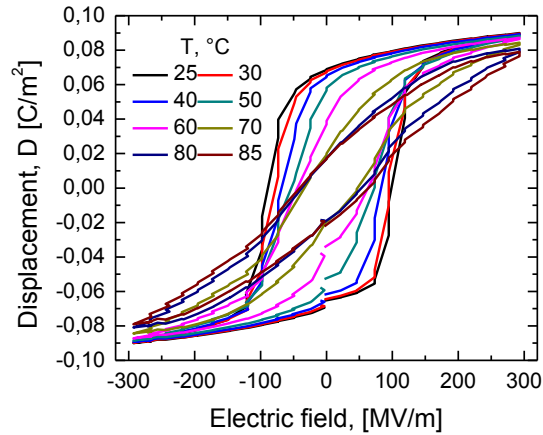
Figure 6.16 Temperature dependent hysteresis loop of P(VDF-TrFE) copolymer from 25°C to 85°C

As shown in Figure 6.16, the hysteresis loop becomes narrower and the polarization levels decreases with temperature. At 65°C, temperature known as Curie transition temperature (Tc), material undergoes ferroelectric to paraelectric transition leading to an abrupt change of the hysteresis loop. To obtain the theoretical entropy and temperature change, we need to use the following two equations to do the calculation.[6]

$$\Delta S = - \int_{E_1}^{E_2} \left(\frac{\partial D}{\partial T}\right)_E dE \qquad \text{Equation 6.1}$$

$$\Delta T = -\frac{T}{\rho} \int_{E_1}^{E_2} \frac{1}{C_E} \left(\frac{\partial D}{\partial T}\right)_E dE \qquad \text{Equation 6.2}$$

According to the above equations, in order to calculate (ΔS) and (ΔT), we plot displacement versus temperature curves taken from E-D loops at different temperatures (Figure 6.17).At around Tc, there is a dramatically drop of displacement which is correlated with the transition from ferroelectric to paraelectric.
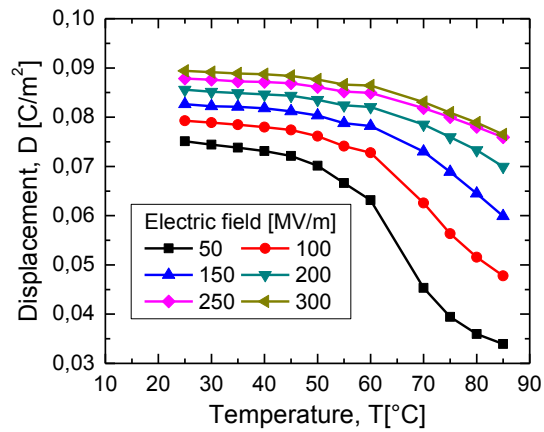
Figure 6.17 Displacement temperature dependence relationship for P(VDF-TrFE) copolymer under different E field.

Next, applying the equations 6.1 and 6.2, we calculated ΔS and ΔT at several electric fields as a function of temperature for P(VDF-TrFE) copolymer. The results are presented in Figure 6.18. Approaching the Currie transition temperature (Tc ~ 65°C) a strong increase of ΔS and ΔT is observed which is due to the ferroelectric to paraelectric transition accompanied by narrowing of the hysteresis loop and thus strong increase of the energy density (inset in Figure 6.18). Through theoretic calculation, the P(VDF-TrFE) copolymer exhibits ΔS=120 J/(kgK) and ΔT=23 °C under an electric field of 300 MV/m at the Tc .
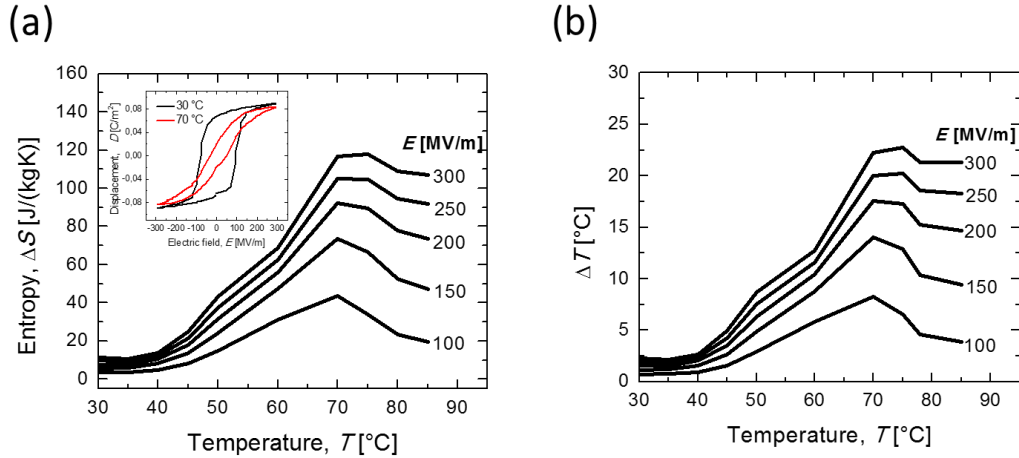
Figure 6.18 Entropy change ΔS and temperature change ΔT of P(VDF-TrFE) copolymer films.

In the above calculation, we use 1.5×10^3 kg/m^3 as the density of P(VDF-TrFE) copolymer and we take specific heat value for our copolymer from the specific heat capacity versus temperature curve for the P(VDF-TrFE) 55/45 mol% copolymer given in literature.[7] It is clear that at around its ferroelectric-paraelectric transition which occurs at Curie temperature (65°C), it gives largest ΔS and ΔT for electrocaloric cooling applications for P(VDF-TrFE) copolymer. On the other hand, in the range from 50°C till 90°C, the adiabatic temperature change is all above 10°C which is very high already.

Similarly, we conducted hysteresis measurements for the terpolymer. We measured the hysteresis loops of P(VDF-TrFE-CFE) terpolymer under different temperature with maximum electric field 200 MV/m at 100 Hz as shown in Figure 6.19. All the hysteresis loops are narrow hysteresis which shows the ferroelectric relaxor property of P(VDF-TrFE-CFE) terpolymer.
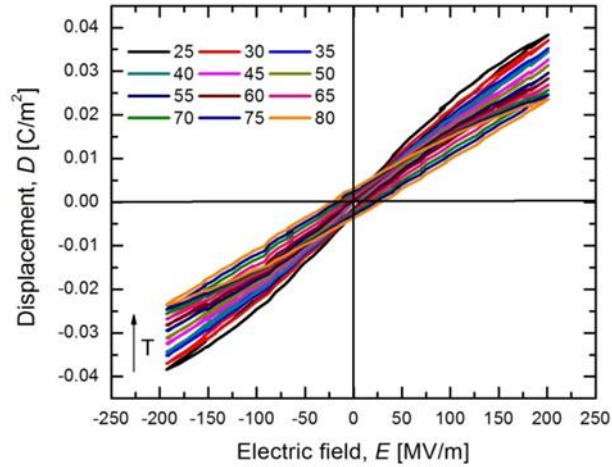
Figure 6.19 Hysteresis loop of P(VDF-TrFE-CFE) terpolymer from 25 °C until 80 °C

We again plot displacement versus temperature curves taken from E-D loops at different temperatures as shown in Figure 6.20. There is obvious drop of the slope for all the D-T curves as shown in Figure 6.20 for P(VDF-TrFE-CFE) terpolymer which is another evidence for the ferroelectric relaxor property of this terpolymer.
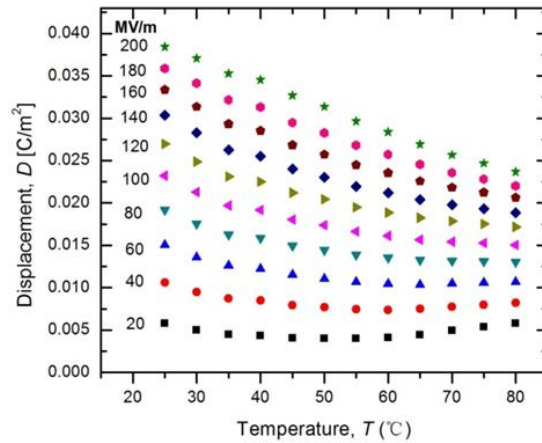
Figure 6.20 Displacement temperature dependence relationship for P(VDF-TrFE-CFE) terpolymer under different E field.

132

We use 1.8×10^3 kg/m^3 as the density of P(VDF-TrFE-CFE) terpolymer (56.2%-36.3%-7.5% by mol %) and we take specific heat value for our terpolymer from the specific heat capacity versus temperature curve for the P(VDF-TrFE-CFE) terpolymer (56.2%-36.3%-7.5% by mol %) given in literature.[7] The temperature dependence of ΔT and ΔS for the terpolymer is quite different from that of the copolymer. From Figure 6.21, we observe that both the entropy change and temperature change decrease monotonically with increasing temperature (rather than peak at Tc). The temperature change at room temperature with an electric field of 200 MV/m is calculated to be approximately 7 °C.
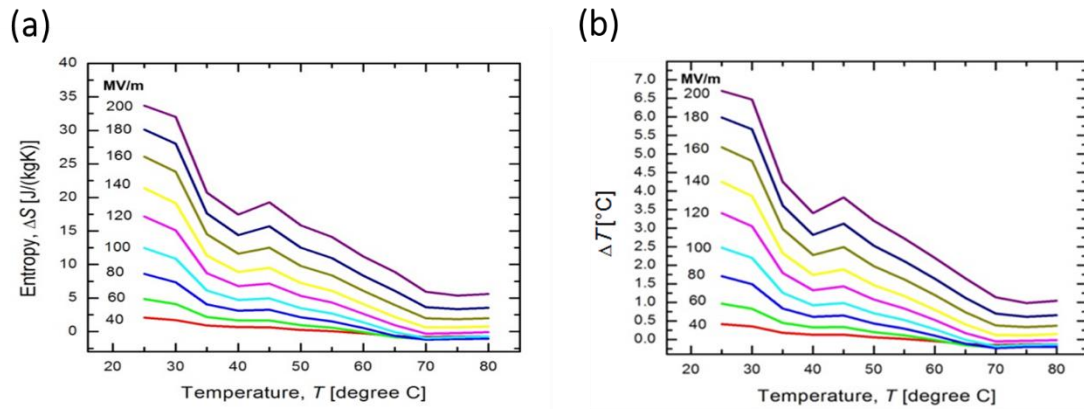
Figure 6.21 Entropy change ΔS and temperature change ΔT of P(VDF-TrFE-CFE) terpolymer.

Although the theoretically calculated change of entropy and temperature for P(VDF-TrFE-CFE) terpolymer is low compared with the copolymer, as reported in the literature stating that the Maxwell relation was derived and applies only for thermodynamic ergodic systems such as ferroelectric materials with clear ferroelectric-paraelectric transition and cannot be used to predict ΔS and ΔT of non-ergodic systems such as

relaxor ferroelectrics, it is reasonable to believe that terpolymer can display similar ECE effect in terms of ΔS and ΔT as copolymer did.[4, 6]

Based on phenomenological theory[4,6] which has been widely used to illustrate the macroscopic phenomena that occur in the ferroelectric materials near their phase transition temperature, ΔS and ΔT is related to the electric displacement D through:

$$\Delta S = -\frac{1}{2}\beta D^2 \implies \Delta T \sim D^2$$

β is assumed as a temperature independent phenomenological coefficient and is only a materials related factor. Based on the above equation the change in entropy from a non-polar state to a polar state is proportional to the electric displacement squared. Therefore material with high displacement D and large β value is expected to have a high entropy change. As shown in Figure 6.22, for the P(VDF-TrFE) copolymer at 65 °C and the P(VDF-TrFE-CFE) terpolymer at 20°C, they have similar hysteresis loop and D value. In additionally, they share similar experimentally derived β value around10^7 (S. G. Lu et al., 2010). Thus is a strong indication that the terpolymer can display similar ECE effect in terms of ΔS and ΔT at room temperature.
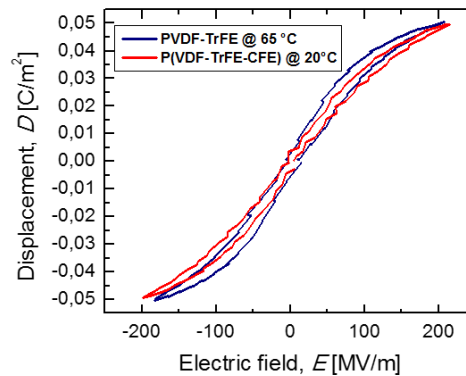
Figure 6.22 Comparison of the D-E loops of the P(VDF-TrFE) copolymer at 65 °C and the P(VDF-TrFE-CFE) terpolymer at 20°C.

6.3.3 Treatment on P(VDF-TrFE) Copolymer for Higher ΔT and ΔS with lower Tc

Although the entropy change and temperature change of P(VDF-TrFE) copolymer are very high, Tc at around 65 °C limits the application of P(VDF-TrFE) copolymer solid stat refrigerator to be used at around room temperature. Therefore lowing Tc with high ΔT and ΔS is a curial problem on the way towards application. Also, if the strong hysteresis effect can be limited, the loss of energy due to hysteresis can be saved. Different approaches were employed in order to shift the Currie transition temperature Tc to lower value and to further increase the adiabatic temperature change (ΔT). To achieve this goal, our research was focused on adding a small amount of chemical moieties, which hope to change the domain size, interrupt the coherent length of the ferroelectric β-phase and facilitate the rotation of the molecular dipoles under electric field. Different ionic liquids and plasticizers have been employed and the most promising results were obtained with propylene carbonate (PC). PC is a high dielectric constant ($\varepsilon=64$) aprotic solvent which effectively can be employed as a plasticizer. A small amount of PC was added to the P(VDF-TrFE) copolymer in the spin coating solution and the temperature dependent polarization response was investigated. Figure 6.23 shows ΔS and ΔT calculated at 250 MV/m for the pure copolymer and treated with 2%wt and 5%wt PC. As seen ΔS and ΔT tend to increase with the amount of the PC reaching a maximum value of ΔT=35°C and ΔS=180 J/(kgK) for the copolymer treated with 5%wt PC.
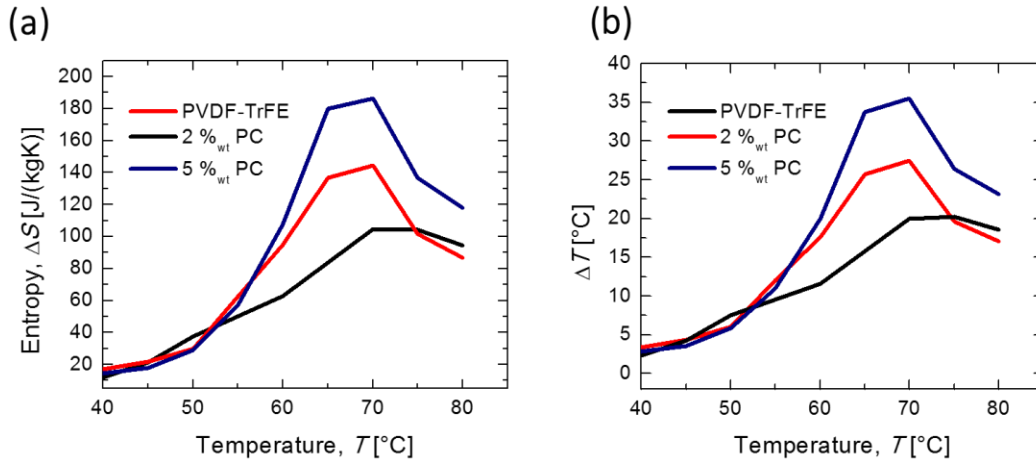
Figure 6.23 Entropy change ΔS and adiabatic temperature change ΔT at 250 MV/m of pure P(VDF-TrFE) copolymer and copolymers treated with small amount of propylene carbonate.

This behavior can be explained by the more pronounced ferroelectric-paraelectric transition and reduction of the remnant polarization at the Tc, which is an indication of the facilitation of the rotation of the molecular dipoles under electric field from plasticizer PC. Polarization hysteresis loops at 30°C (ferroelectric) and 70°C (paraelectric) for the investigated compositions are shown in Figure 6.24.
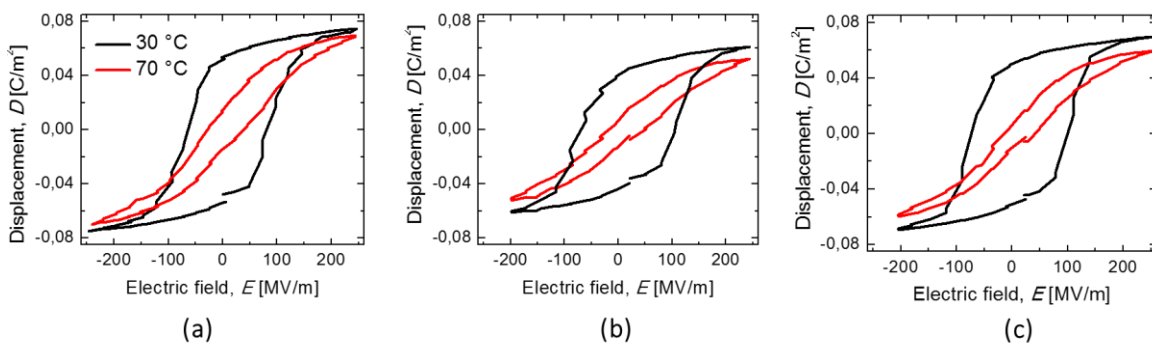
Figure 6.24 The D-E loops measured at 10 Hz for (a) P(VDF-TrFE) copolymer, (b) P(VDF-TrFE) copolymer-2%wt PC, (c) P(VDF-TrFE) copolymer-5%wt PC.

As can be seen the remnant polarization (D at 0 MV/m) at 70°C for the pure P(VDF-TrFE) copolymer is 0.02 C/m^2, while for 2%wt PC it is 0.0052 C/m^2 and for 5%wt it is 0.0041 C/m^2. The data presented here suggest that propylene carbonate can be used to increase the ECE of P(VDF-TrFE) copolymer. However, it should be noted that ΔS and ΔT was derived theoretically from experimentally measured temperature dependent polarization hysteresis loops. Therefore, the restrict requirement to fulfill Maxwell relation as an ergodic systems points out direct adiabatic temperature change measurements are required to verify the above approach.[6]

6.4 Organic-Inorganic Hybrid ECE Materials Development and Electrocaloric Effect Measurement

As we proposed in 6.1.4, a composite ferroelectric system with high dielectric constant, high breakdown field and low dielectric loss is demanded. The main challenge in the development of the nanocomposite ferroelectric system is to obtain a homogeneous dispersion of the inorganic ferroelectric ceramic nanoparticles in the ferroelectric matrix. Due to the incompatibility between surfaces of the ceramic nanoparticles and the ferroelectric polymer matrix, agglomeration occurs and leads to interfacial polarization and thus high current leakage and energy losses. To overcome this problem the surface of the nanoparticles need to be functionalized with proper functional groups to match the matrix polymer. The ceramic nanoparticles we selected for nanocomposite are $Ba_{1-x}Sr_xTiO_3$ nanoparticles as they have room temperature Tc (around 20 °C) with high dielectric constant. Based on the analysis in section 6.3, P(VDF-TrFE-CFE) terpolymer with similar real electrocaloric effect but less hysteresis loss compared to that of P(VDF-TrFE) copolymer was selected as the composite matrix polymer.

For the modification of $Ba_{1-x}Sr_xTiO_3$ nanoparticles, fluoroacids were selected as most promising ligand to match with P(VDF-TrFE-CFE) terpolymers. $Ba_{1-x}Sr_xTiO_3$ nanoparticles with different sizes and Ba/Sr ratios were synthesized as described in section 6.2 and functionalized with 5-Fluoro-2-(trifluoromethyl)benzoic acid. In this surface functionalization, the carboxylic acid strongly binds to the surface of $Ba_{1-x}Sr_xTiO_3$ nanoparticles while the fluorinated tail is compatible with the PVDF-based matrix very well. To make the composite, P(VDF-TrFE-CFE) terpolymer was dissolved in DMF and the $Ba_{1-x}Sr_xTiO_3$ nanodispersion in DMF was added to it. The nanodispersion was treated with high power ultrasonic tip for 10 min, followed by 2h ultrasonic bath to homogenize. The prepared nanocomposite solution is stable showing no significant agglomeration over days. We prepared thin films (2 μm) using drop-casting technique and measured the polarization response. To visualize these microstructures, the cross-sections of nanocomposite film were imaged using scanning electron microscopy (SEM) as shown in Figure 6.25. The loading of nanoparticle in terpolymer is 50% by weight.
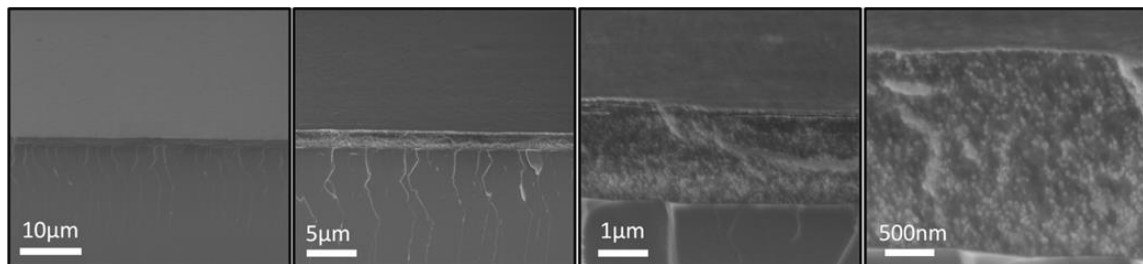
Figure 6.25 Cross-sectional SEM micrographs at different magnifications of a terpolymer film loaded with 40 nm size $Ba_{0.65}Sr_{0.35}TiO_3$ nanoparticles of about in diameter

Clearly from Figure 6.25, the film is homogeneous and the nanoparticles are uniformly distributed inside the polymer matrix. There is no nanoparticle aggregation or sedimentation, nor any residual porosity in the composite. In addition, when using nanoparticles with a size smaller than 10 nm, we obtained completely transparent samples with a loading up to 70 wt%. After successfully making homogeneously mixed nanocomposite, we prepared several samples having different particle composition, size, and weight fractions for electrocaloric effect evaluation. Hysteresis loops for nanocomposite samples were measured to compare the dielectric properties of the different nanocomposites with respect to the terpolymer. Representative results are reported in Figure 6.26.
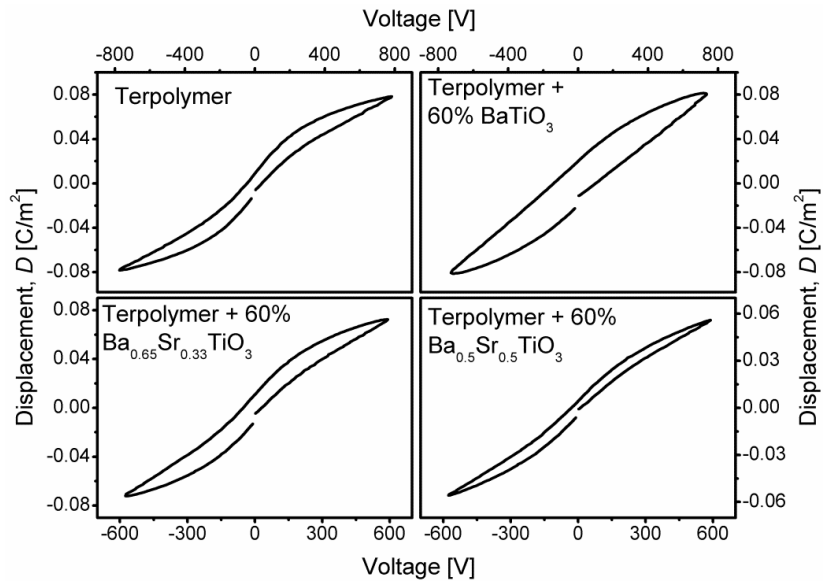
Figure 6.26 D-V loops for the pure terpolymer (top left graph) and different nanocomposites containing 60%wt $Ba_{1-x}Sr_xTiO_3$ nanoparticles measured at 100Hz.

As indicated in Figure 2.26, when the terpolymer is loaded with $BaTiO_3$ nanoparticles, the displacement slightly increases and the hysteresis loops become broader. When

BaTiO$_3$ is replaced with Ba$_{1-x}$Sr$_x$TiO$_3$, the hysteresis loops are as narrow as pure terpolymer but no improvement on polarization. Because a decrease in the maximum polarization level is observed with all hybrid materials, it indicates the best performance is ultimately obtained using the pure terpolymer instead of composite. The reason for the limited dielectric constant improvement from nanoparticles is the loading amount for nanoparticles in the composite system is 60% by weight which equals to around 17% by volume percentage. As we reviewed in section 6.1.4, to harvest both advantages from composite system, the loading by volume should achieve to 50%. For this reason, we decided to directly measure the electrocaloric temperature change with P(VDF-TrFE-CFE) terpolymer and fabricate multilayer ECE device using pure terpolymer as the EC material.

6.5 Electrocaloric effect based refrigerator device fabrication and characterization

As the P(VDF-TrFE-CFE) is a non-ergodic systems as relaxor ferroelectrics, the calculation of ΔT and ΔS from Maxwell relation need to be verify through the direct temperature change measurement. Also, direct measurement is more like the real application and will show the real ability of this type of solid state refrigerator.

6.5.1 Direct ΔT Measurement for P(VDF-TrFE-CFE) Terpolymer Monolayer Device

As free standing ECE device can minimum the influence of the substrate on the electrocaloric effect, here we developed an ECE device configuration as shown in Figure 2.27 (a). It consists of PVDF-TrFE-CFE free-standing monolayer membrane (about 10μm in thickness) coated with Al evaporated circular electrodes (diameter=13mm) on both sides in parallel plate capacitor configuration. Polyimide and polyacrylate stiff

frames were used to support the membrane. For this free standing P(VDF-TrFE-CFE) terpolymer ECE device, the adiabatic temperature change ΔT can be directly measured as a function of the applied electrical field through a temperature sensor. The device performance was evaluated by applying an increasing electrical field up to 100 MV/m which is a safe electrical field far below the electrical breakdown strength of the material. The resulting D-E loop is shown in Figure 2.27(b).
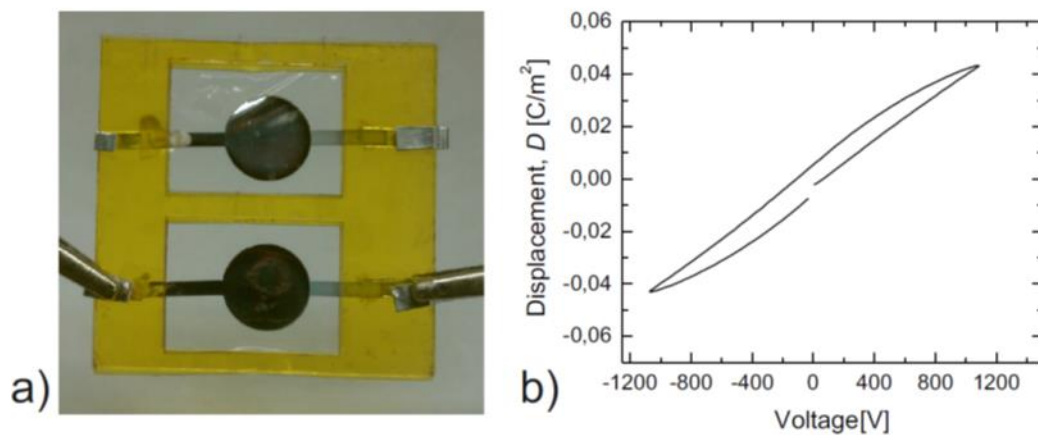
Figure 6.27 Free standing P(VDF-TrFE-CFE) membrane (a) and respective D-E hysteresis loop(b)

To check the temperature change during electrical field change, we used a IR-camera to trace the temperature of the free standing P(VDF-TrFE-CFE) terpolymer ECE device when electrical field applied and withdrawal. As shown in Figure 2.28, the measured value was 3.3 K for the P(VDF-TrFE-CFE) terpolymer at a peak electric field of 75 MV/m. This value included the heat lost to the environment because we don't have a thermal reservoir connected with the free-standing ECE device during the measurement. Therefore, this value is reasonable and also matches the literature value well.[46]
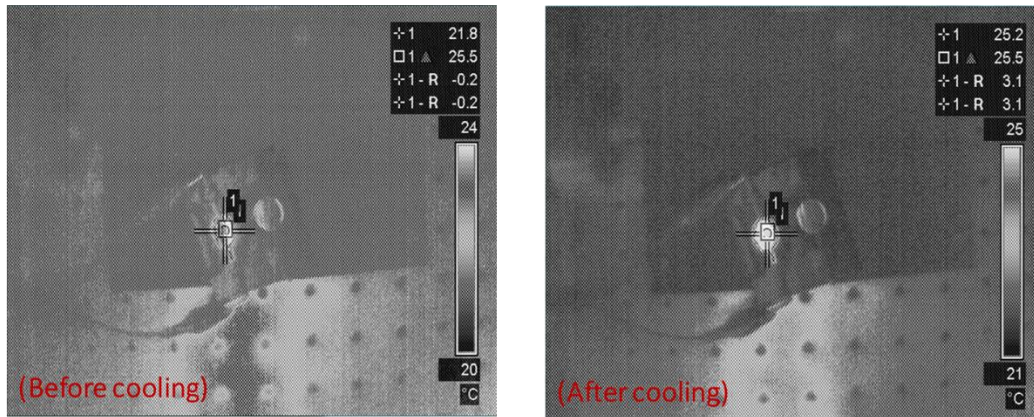
Figure 6.28 IR measurements of the free standing ECE device temperature before and after electrocaloric cooling is induced.

6.5.2 Multilayer ECE Device Fabrication and Temperature Change (ΔT) Measurement

Clearly from previous description, the basic device configuration of the electrocaloric refrigerator is a capacitor made by ferroelectric material. To harvest a large temperature change through electrocaloric effect using a reasonable voltage, the electrocaloric material should be in a thin-film form and the electrode should be thin also. Therefore, if we can make several thin film capacitors connected in parallel as a device unit which equals to enlarge the device working area, hopefully it can increase the electrocaloric effect. However, to make multilayers through traditional lamination process will produces an uneven residual stress and also air voids. Therefore, we design a multilayer electrocaloric device configuration as shown in Figure 6.29. It is in an interdigitated configuration of a silicon wafer, we carve out two arrays of vertically oriented thin electrodes and then infiltrate electrocaloric materials inside of the space in arrays. The electrodes are not only used to bias the electrocaloric material filled in between but also to serve as a structural frame to keep the overall shape of the device.

142
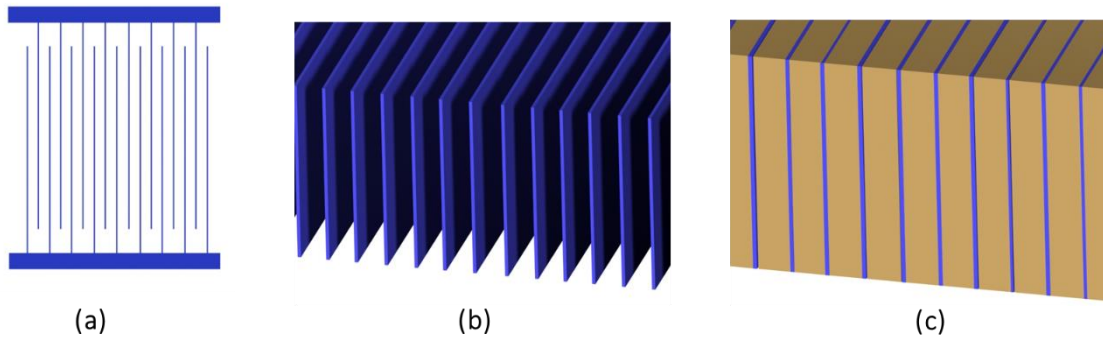
Figure 6.29 Interdigitated electrodes design for ECE device. (a) top view (b) angled view (c) after filling with an electrocaloric material

The interdigitated electrode we used in this application is provided by a collaboration team with the final dimension as follows. For electrodes, each finger is 5μm in width, 50μm in height and 500μm in length. The overlapping length of neighbor fingers is 480μm and the gap in between neighbor finger is 5μm. There are 100 fingers for each electrode and 200 fingers in total for both positive electrode and negative electrode. To make the contact pad from electricity wire connection, the size for contact pad is 3×3mm. In Figure 6.30 (a), it is the illustration of the final electrodes configuration but with different dimension only as an example to show the real device configuration. For Figure 6.30 (b), it is a microscope image for a well etched Si interdigitated electrodes.
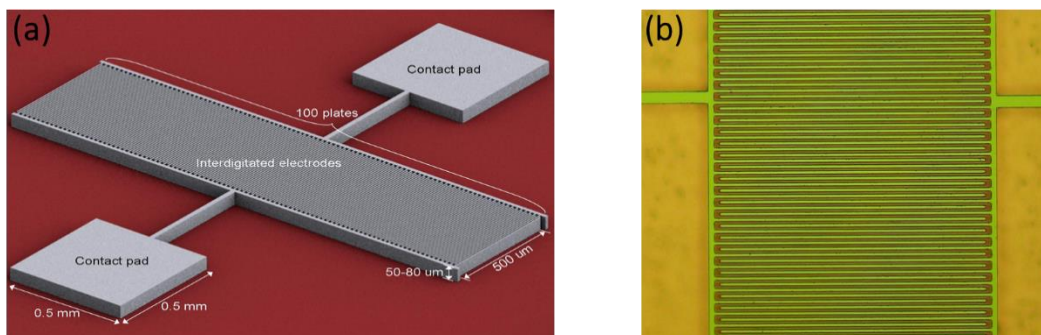
Figure 6.30 Illustrations of (a) Interdigitated electrodes configuration with contact pads and (b) microscope image of well etched interdigitated electrodes.

After getting the interdigitated Si electrodes, we performed P(VDF-TrFE-CFE) infiltration into the interdigitated Si electrodes to form the multilayer ECE device. Before fabricating the final device, to evaluate the feasibility of infiltrating polymers into the narrow spaces in the free-standing interdigitated electrodes, we first carefully studied the infiltration condition. We employed concentrated solutions of the terpolymer in dimethylformamide (DMF), tailored the polymer concentration and optimized temperature and vacuum-drying conditions. SEM images confirm the progress made in obtaining uniform coatings of the silicon plates (Figure 6.31), and homogeneous infiltration along the full height of the plates, with negligible residual porosity or uncoated areas.
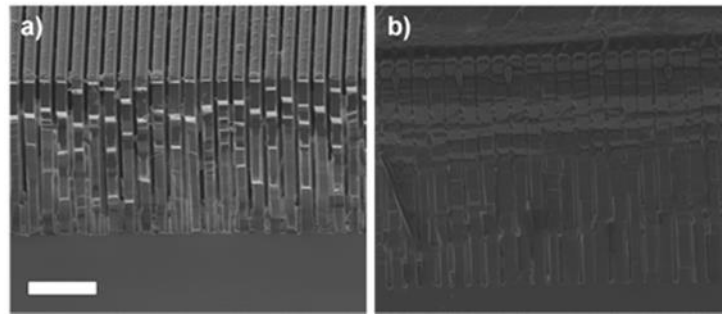
Figure 6.31 SEM images of parallel fingers infiltrated with PVDF-TrFE-CFE terpolymer. a) Sample prepared from a low concentration (25 mg/mL) solution without the heat treatment under vacuum; b) sample prepared from a high concentration terpolymer solution (75 mg/mL) and degassed at 100 ºC under vacuum. The scale bar for is 50 μm for the images.

As we can see from Figure 6.31 (a), for the infiltration device made under low concentration polymer solution, there are uncoated area clearly existed. With the help of heating degas treatment and enhanced concentration, the infiltration is homogeneous besides minor defects.

For the final device infiltration, P(VDF-TrFE-CFE) terpolymer was dissolved in DMF with concentration of 50mg/ml. The solution was filtered through 0.45µm size syringe filter and then poured into a vial with the interdigitated device already in it. For the above steps were done in a clean room. After then, the vials were placed in a vacuum oven and gradually heated to 80 °C in 40 minutes. After most of the solvent evaporated, the temperature was raised to 100 °C for another hour to remove residual solvent. The infiltration was confirmed by SEM shown in Figure 6.32. There are a few gaps unfilled by the polymer, which were likely caused by the pulling force during sample preparation: the polymer was not sufficiently brittle when the sample was broken to create the cross-section.
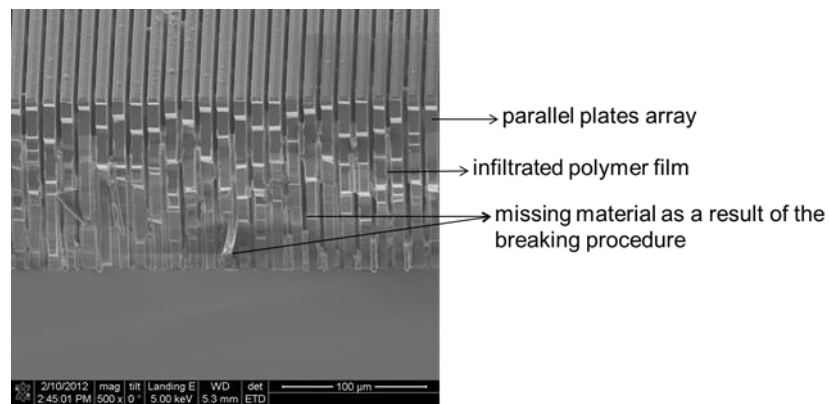
Figure 6.32 Cross-sectional SEM image of interdigitated electrode array infiltrated with P(VDF-TrFE-CFE) terpolymer

The infiltrated multilayer ECE device was subjected to polarization measurement on a probe station. The device had a total active area of 0.048 cm^2 with 5 μm film thickness. The applied voltage was gradually ramped up to 360 V at which the displacement of 0.01 C/m^2 and the electric field was 70 MV/m. The breakdown electric field was around 80 MV/m. The D-E loop shown in Figure 6.33 appears to be comparable with those of P(VDF-TrFE-CFE) terpolymer monolayer thin film capacitors, although the displacement and breakdown field of the thin film capacitors are larger: 0.015 C/m^2 at 60 MV/m and a breakdown field of 360 MV/m. The reduced dielectric strength could be caused by charge concentration at the tip of the interdigitated electrode and trapped air. Further optimization of the interdigitated electrodes and the electrocaloric materials should lead to significantly higher polarization and the attainment of electrocaloric cooling effect.
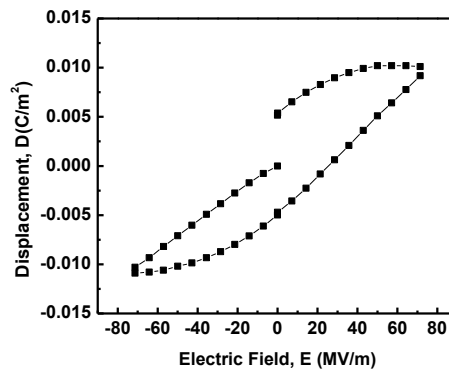
Figure 6.33 Hysteresis loop for a multilayer P(VDF-TrFE-CFE) terpolymer ECE device at 25 °C.

6.6 Conclusion and Future Work

We successfully established a method to synthesis $Ba_{1-x}Sr_xTiO_3$ serials of nanoparticles in the size range from 8-12nm. Also, with the help of tuning the ratio of [Ba] and [Ti] precursors with slightly less amount of [Ti], we made even smaller size of $BaTiO_3$ nanoparticles at size around 6-8 nm. We investigated the dielectric properties of our synthesized 6-8nm $BaTiO_3$ nanoparticles and proved it cubic phase crystalline structure with dielectric constant around 600. To decrease the curie transition temperature of the ferroelectric ceramic nanoparticles, several $Ba_{1-x}Sr_xTiO_3$ nanoparticles with different x value were synthesized and characterized to prove the near room temperature Tc of $Ba_{0.65}Sr_{0.35}TiO_3$ and $Ba_{0.75}Sr_{0.25}TiO_3$ nanoparticles with size around 40nm. More systemically study of $Ba_{1-x}Sr_xTiO_3$ nanoparticles with size smaller then 10nm could be an interesting work to analysis the nanoeffect on the crystalline phase and Curie temperature.

For organic ferroelectric materials, we systemically studied the electrocaloric effect of P(VDF-TrFE) copolymer and P(VDF-TrFE-CFE) terpolymer. The theoretical temperature change are 23°C and 7°C for copolymer and terpolymer, respectively. For room temperature operations, we found P(VDF-TrFE-CFE) terpolymer to be a best suited commercially available material. We found organic nanocomposites containing propylene carbonate (PC) are very interesting, potentially offering a maximum adiabatic temperature change of ΔT=35°C but at temperatures above the room temperature. Further investigation of this and related organic nanocomposites may prove highly fruitful. Fluoroacids treated $Ba_{1-x}Sr_xTiO_3$ nanoparticles and P(VDF-TrFE-CFE) composites have been characterized by dielectric measurement. No obviously change of ferroelectric performance or dielectric constant on the composite compared to the pure terpolymer. Further increasing the amount of nanoparticles loading in the composite could be a work

to improve the dielectric constant of the composite guided by the calculation theory for this type of composite system. The interdigitated electrode samples were successfully infiltrated with this terpolymer. The displacement measured was 0.01 C/m^2 at 70MV/m for this device. Polarization measurement could be carried out with sweeping electric fields up to 80 MV/m. Further improvement for this device could be focus on improving the filtration process with 100% polymer filled into the space between electrodes.

Reference:

[1]   Andrew J. Lovinger, "Ferroelectric Polymers", Science, Vol. 220 no. 4602 pp. 1115-1121,1983

[2]   Karin M. Rabe, Charles H. Ahn, Jean-Marc Triscone, "Physics of Ferroelectrics, A Modern Perspective", Springer, 2007

[3]   Hari S. Nalwa, "Ferroelectric Polymers: Chemistry, Physics, and Applications", Marcel Dekker. Inc, New York, 1995

[4]   J. F. Scott, "Electrocaloric Materials," *Annual Review of Materials Research*, vol. 41, no. 1, pp. 229–240, Aug. 2011.

[5]   A. Khodayari and S. Mohammadi, "Solid-state cooling line based on the electrocaloric effect.," *IEEE transactions on ultrasonics, ferroelectrics, and frequency control*, vol. 58, no. 3, pp. 503–8, Mar. 2011.

[6]   M. Valant, "Electrocaloric materials for future solid-state refrigeration technologies," *Progress in Materials Science*, vol. 57, no. 6, pp. 980–1009, Jul. 2012.

[7]   B. Neese, B. Chu, S.-G. Lu, Y. Wang, E. Furman, and Q. M. Zhang, "Large electrocaloric effect in ferroelectric polymers near room temperature.," *Science*, vol. 321, no. 5890, pp. 821–3, Aug. 2008.

[8]   S.-G. Lu and Q. Zhang, "Electrocaloric Materials for Solid-State Refrigeration," *Advanced Materials*, vol. 21, no. 19, pp. 1983–1987, May 2009.

[9]   https://en.wikipedia.org/wiki/Refrigerator

[10]   Callister, William D. Materials Science and Engineering: An Introduction. New York: John Wiley & Sons, 2007. Print.

[11]   M. W. Barsoum, "Fundamentals of Ceramics". Bristol, UK: Institute of Physics Pub., 2003. Print.

[12]   J. H. Qiu and Q. Jiang, "Effect of misfit strain on the electrocaloric effect in epitaxial SrTiO3 thin films," *The European Physical Journal B*, vol. 71, no. 1, pp. 15–19, Jul. 2009.

[13]   D. Saranya, A. R. Chaudhuri, J. Parui, and S. B. Krupanidhi, "Electrocaloric effect of PMN-PT thin films near morphotropic phase boundary," *Bulletin of Materials Science*, vol. 32, no. 3, pp. 259–262, Aug. 2009.

[14]   J. Zhang, a. a. Heitmann, S. P. Alpay, and G. a. Rossetti, "Electrothermal properties of perovskite ferroelectric films," *Journal of Materials Science*, vol. 44, no. 19, pp. 5263–5273, Jun. 2009.

[15]   T. M. Correia, J. S. Young, R. W. Whatmore, J. F. Scott, N. D. Mathur, and Q. Zhang, "Investigation of the electrocaloric effect in a $PbMg_{2/3}Nb_{1/3}O_3$-$PbTiO_3$ relaxor thin film," *Applied Physics Letters*, vol. 95, no. 18, p. 182904, 2009.

[16]   Y. Bai, G. Zheng, and S. Shi, "Direct measurement of giant electrocaloric effect in $BaTiO_3$ multilayer thick film structure beyond theoretical prediction," *Applied Physics Letters*, vol. 96, no. 19, p. 192902, 2010.

[17]   Y. Bai, G.-P. Zheng, and S.-Q. Shi, "Kinetic electrocaloric effect and giant net cooling of lead-free ferroelectric refrigerants," *Journal of Applied Physics*, vol. 108, no. 10, p. 104102, 2010.

[18]   L. Mañosa, D. González-Alonso, A. Planes, E. Bonnot, M. Barrio, J.-L. Tamarit, S. Aksoy, and M. Acet, "Giant solid-state barocaloric effect in the Ni-Mn-In magnetic shape-memory alloy.," *Nature materials*, vol. 9, no. 6, pp. 478–81, Jun. 2010.

[19]   C.-L. Jia, K. W. Urban, M. Alexe, D. Hesse, and I. Vrejoiu, "Direct observation of continuous electric dipole rotation in flux-closure domains in ferroelectric Pb(Zr,Ti)O$_3$.," *Science*, vol. 331, no. 6023, pp. 1420–3, Mar. 2011.

[20]   A. S. Mischenko, Q. Zhang, R. W. Whatmore, J. F. Scott, and N. D. Mathur, "Giant electrocaloric effect in the thin film relaxor ferroelectric 0.9 PbMg$_{1/3}$Nb$_{23}$O$_3$–0.1 PbTiO$_3$ near room temperature," *Applied Physics Letters*, vol. 89, no. 24, p. 242912, 2006.

[21]   N. C. Surface-functionalized, B. Nanoparticles, J. Li, J. Claude, and L. E. Norena-franco, "Electrical Energy Storage in Ferroelectric Polymer Nanocomposites Containing Surface-Functionalized BaTiO$_3$ Nanoparticles," no. 8, pp. 6304–6306, 2008.

[22]   J. Y. Li, L. Zhang, and S. Ducharme, "Electric energy density of dielectric nanocomposites," *Applied Physics Letters*, vol. 90, no. 13, p. 132901, 2007.

[23]   a. K. Tripathi, T. C. Goel, and P. K. C. Pillai, "Effect of temperature on the charge-field hysteresis phenomena in lanthanum-doped lead zirconate titanate-poly(vinylidine fluoride) composite," *Journal of Materials Science Letters*, vol. 12, no. 24, pp. 1945–1946, 1993.

[24]   R. Popielarz, C. K. Chiang, R. Nozaki, and J. Obrzut, "Dielectric Properties of Polymer/Ferroelectric Ceramic Composites from 100 Hz to 10 GHz," *Macromolecules*, vol. 34, no. 17, pp. 5910–5915, Aug. 2001.

[25]   C. P. Wong and T. Marinis, "A precise numerical prediction of effective dielectric constant for polymer-ceramic composite based on effective-medium theory," *IEEE Transactions on Components and Packaging Technologies*, vol. 23, no. 4, pp. 680–683, 2000.

[26]   N. Levi, R. Czerw, S. Xing, P. Iyer, D. L. Carroll, and N. Carolina, "Properties of Polyvinylidene Difluoride − Carbon Nanotube Blends," 2004.

[27]   Z. Zhang and T. C. M. Chung, "The Structure-Property Relationship of Poly (vinylidene difluoride) -Based Polymers with Energy Storage and Loss under Applied Electric Fields," pp. 9391–9397, 2007.

[28]   S. Adireddy, C. Lin, B. Cao, W. Zhou, and G. Caruntu, "Solution-Based Growth of Monodisperse Cube-Like BaTiO$_3$ Colloidal Nanocrystals," *Chem. Mater.,* vol 22, pp 1946–1948, 2010

[29]   J. Petzelt, "Dielectric Grain-Size Effect in High-Permittivity Ceramics," *Ferroelectrics*, vol. 400, no. 1, pp. 117–134, Sep. 2010.

[30]   M. ULUDOGAN, T. CAGIN, "First Principles Approach to BaTiO₃," vol. 30, pp. 277–285, 2006.

[31]   J. Moon, E. Suvaci, A. Morrone, S. a. Costantino, and J. H. Adair, "Formation mechanisms and morphological changes during the hydrothermal synthesis of BaTiO3 particles from a chemically modified, amorphous titanium (hydrous) oxide precursor," *Journal of the European Ceramic Society*, vol. 23, no. 12, pp. 2153–2161, Nov. 2003.

[32]   Z. Zhao, V. Buscaglia, M. Viviani, M. Buscaglia, L. Mitoseriu, A. Testino, M. Nygren, M. Johnsson, and P. Nanni, "Grain-size effects on the ferroelectric behavior of dense nanocrystalline BaTiO3 ceramics," *Physical Review B*, vol. 70, no. 2, p. 024107, Jul. 2004.

[33]   G. L. Brennecka, J. F. Ihlefeld, J.-P. Maria, B. a. Tuttle, and P. G. Clem, "Processing Technologies for High-Permittivity Thin Films in Capacitor Applications," *Journal of the American Ceramic Society*, vol. 93, no. 12, pp. 3935–3954, Dec. 2010.

[34]   P. Sedykh, D. Michel, E. V. Charnaya, and J. Haase, "Size Effects in Fine Barium Titanate Particles," *Ferroelectrics*, vol. 400, no. 1, pp. 135–143, Sep. 2010.

[35]   A. Meneses-Franco, V. H. Trujillo-Rojo, and E. a. Soto-Bustamante, "Synthesis and characterization of pyroelectric nanocomposite formed of BaTiO₃ nanoparticles and a smectic liquid crystal matrix," *Phase Transitions*, vol. 83, no. 10–11, pp. 1037–1047, Oct. 2010.

[36]   B. Neese, S. G. Lu, B. Chu, and Q. M. Zhang, "Electrocaloric effect of the relaxor ferroelectric poly(vinylidene fluoride-trifluoroethylene-chlorofluoroethylene) terpolymer," *Applied Physics Letters*, vol. 94, no. 4, p. 042910, 2009.

[37]   P. H. de Oliveira Neto, W. F. da Cunha, R. Gargano, and G. Magela e Silva, "Molecular dynamics investigation of charge carrier density influence over mobility in conjugated polymers.," *The journal of physical chemistry. A*, vol. 113, no. 52, pp. 14975–8, Dec. 2009.

[38]   J. H. Qiu and Q. Jiang, "Orientation dependence of the electrocaloric effect of ferroelectric bilayer thin films," *Solid State Communications*, vol. 149, no. 37–38, pp. 1549–1552, Oct. 2009.

[39]   S. Kar-Narayan and N. D. Mathur, "Predicted cooling powers for multilayer capacitors based on various electrocaloric and electrode materials," *Applied Physics Letters*, vol. 95, no. 24, p. 242903, 2009.

[40]   V. V. Kochervinskiĭ, "New electrostriction materials based on organic polymers: A review," *Crystallography Reports*, vol. 54, no. 7, pp. 1146–1171, Dec. 2009.

[41]   S. Kar-Narayan and N. D. Mathur, "Direct and indirect electrocaloric measurements using multilayer capacitors," *Journal of Physics D: Applied Physics*, vol. 43, no. 3, p. 032002, Jan. 2010.

[42]   P. F. Liu, J. L. Wang, X. J. Meng, J. Yang, B. Dkhil, and J. H. Chu, "Huge electrocaloric effect in Langmuir–Blodgett ferroelectric polymer thin films," *New Journal of Physics*, vol. 12, no. 2, p. 023035, Feb. 2010.

[43]   P. H. de Oliveira Neto, W. F. da Cunha, L. F. Roncaratti, R. Gargano, and G. M. e Silva, "Thermal effects on photogeneration of free carriers in organic conductors," *Chemical Physics Letters*, vol. 493, no. 4–6, pp. 283–287, Jun. 2010.

[44]   B. F. Xia, Z. Cheng, H. Xu, H. Li, Q. Zhang, G. J. Kavarnos, R. Y. Ting, G. Abdel-sadek, and K. D. Belfield, "High Electromechanical Responses in a," vol. 32816, no. 21, pp. 1574–1577, 2003.

[45]   R. Su, J.-K. Tseng, M.-S. Lu, M. Lin, Q. Fu, and L. Zhu, "Ferroelectric behavior in the high temperature paraelectric phase in a poly(vinylidene fluoride-co-trifluoroethylene) random copolymer," *Polymer*, vol. 53, no. 3, pp. 728–739, Feb. 2012.

[46]   Y. Jia and Y. Sungtaek Ju, "A solid-state refrigerator based on the electrocaloric effect," *Applied Physics Letters*, vol. 100, no. 24, p. 242901, 2012.

CHAPTER SEVEN

Conclusions and Perspectives

Smart materials, because of their unique properties such as environment response ability and multifunctionality, have been widely investigated to explore new functionalities unavailable in traditional materials or to mimic the biological systems. Synthetic smart polymers are particularly attractive as they can easily be designed with new smart properties and tuned or enhanced their existing properties in smart functions by polymer synthesis or composite formulation. The main focus in this dissertation listed above are in three aspects: (1) healable polymer composites for structural materials application and healable composite conductor for electronic device application; (2) conducting polymer polypyrrole actuator for implantable medical device application; and (3) ferroelectric polymer and ceramic nanoparticles composites for electrocaloric effect based solid state refrigeration application. A summary of results, conclusions and perspective works are given as follows:

(1) Glass fibers were successfully functionalized by 3-aminopropyltriethoxysilane through silanization and by 1,1'-(Methylenedi-4,1-phenylene)bismaleimide (MDPB) through Michael addition. 2MEP4F healable polymer (a furans and maleimides crosslinked polymer) and Epon 862 epoxy polymer composite coupons fabricated with as-received glass fibers and functionalized glass fibers were tested through short beam shear (SBS) test. The SBS data suggest that functionalized glass fibers with MDPB groups on surface has successfully bonded with 2MEP4F polymer matrix as indicated through dramatically increasing of

153

SBS strength. Therefore, further optimization of the functionalized MDPB-GF will continue to improve the mechanical Strength of 2MEP4F panels. Furthermore, the healing properties of the 2MEP4F polymer composite with optimized MDPB-glass fibers need to be carefully studied as an important future work.

(2) To lower the cost of the healable polymer matrix in the structural composite materials system, a new healable polymer composes with polymer of Poly(furfuryl alcohol) (PFA) and 1,1'-(Methylenedi-4,1-phenylene)bismaleimide (MDPB) was developed and characterized. Three types of healable with various PFA to MDPB ratio were detailed studied. The PFA-MDPB healable polymer with 16:1 ratio of PFA:MDPB (named as FM161) showed same healing ability as 2MEP4F while all starting materials are cheaper and commercial available. To further improve the mechanical strength of the PFA-MDPB healable polymer, epoxy as a strengthen part was mixed with PFA-MDPB healable polymer with 1:1 ratio by volume to form composite. The PFA, MDPB and epoxy composite polymers were further reinforced by carbon fiber as done with 2MEP4F matrix previously and the final composites were proved to have higher short beam shear strength and same 2MEP4F healing efficiency. For the future work, the ratio of PFA and MDPB healable polymers to epoxy polymers need to be systemically studied to find out the optima value for higher SBS strength with high healing efficiency. Furthermore, multiple times healing possibility need to be investigated for this composite system to prove its potential in real application.

(3) A healable semi-transparent composite conductor has been demonstrated based on the reversible Diels-Alder cyclo-addition reaction in the MDPB-FGEEDR copolymer and the AgNW percolation network inlaid in the polymer's surface layer. The composite is transparent, flexible, and has a surface conductivity comparable to that of indium tin oxide coating on glass. A crack cut on the conductive surface can self-heal upon heating at 110 °C. As much as 97% of the surface conductivity can be recovered in 5 minutes. The self-healing is repeatable at the same location for multiple cycles of cutting and healing. For the future work, to make this composite conductor suitable as substrate to substitute the ITO in traditional optoelectronic devices, we need to improve the transparency for this composite conductor. Furthermore, the glass transition temperature or the soften temperature for this composite conductor need to be enhanced. After solving this two problems, healable optoelectronic device could be a very interesting work based on the current healable polymer and composite conductor.

(4) Various pyrrole derivatives were studied for the electrochemical co-polymerization with pyrrole monomer. The monomers that passed the screening of solubility and CV testing were tried for polymerization of homopolymer first. Copolymers with pyrrole were successfully synthesized with N-methylpyrrole/pyrrole and 3-methylpyrrole/pyrrole pairs. The N-methylpyrrole/pyrrole copolymer showed improved flexibility over than that of pyrrole homopolymer. Unimorph bending actuators were fabricated based on the N-methylpyrrole/pyrrole copolymer. Large bending angle was observed by switching the potential from -850mV to 850mV. The actuation was reversible.

For the future work, the mechanical properties for those newly developed polypyrrole copolymers need to be carefully characterized. Bimorph bending actuator device based on polypyrrole copolymers could be an interesting direction as it will be suitable for application in implantable medical device area. Thereafter, to establish the database about the blocking force, bending angle, actuation holding time without electrical field and lifetime for the bimorph polypyrrole copolymer actuator will be very necessary work.

(5) We successfully established a method to synthesis $Ba_{1-x}Sr_xTiO_3$ serials of nanoparticles in the size range from 8-12nm. Also, with the help of tuning the ratio of [Ba] and [Ti] precursors with slightly less amount of [Ti], we made even smaller size of $BaTiO_3$ nanoparticles at size around 6-8 nm. We investigated the dielectric properties of our synthesized 6-8nm $BaTiO_3$ nanoparticles and proved it cubic phase crystalline structure with dielectric constant around 600. To decreasing the curie transition temperature of the ferroelectric ceramic nanoparticles, several $Ba_{1-x}Sr_xTiO_3$ nanoparticles with different x value were synthesized and characterized to prove the near room temperature Tc of $Ba_{0.65}Sr_{0.35}TiO_3$ and $Ba_{0.75}Sr_{0.25}TiO_3$ nanoparticles with size around 40nm. More systemically study of $Ba_{1-x}Sr_xTiO_3$ nanoparticles with size smaller then 10nm could be an interesting work to analysis the nanoeffect on the crystalline phase and Curie temperature. For organic ferroelectric materials, we systemically studied the electrocaloric effect of P(VDF-TrFE) copolymer and P(VDF-TrFE-CFE) terpolymer. The theoretical temperature change are 23^0C and 7^0C for copolymer and terpolymer, respectively. For room temperature operations, we

found P(VDF-TrFE-CFE) terpolymer to be a best suited commercially available material. We found organic nanocomposites containing propylene carbonate (PC) are very interesting, potentially offering a maximum adiabatic temperature change of $\Delta T=35°C$ but at temperatures above the room temperature. Further investigation of this and related organic nanocomposites may prove highly fruitful. Fluoroacids treated $Ba_{1-x}Sr_xTiO_3$ nanoparticles and P(VDF-TrFE-CFE) composites have been characterized by dielectric measurement. No obviously change of ferroelectric performance or dielectric constant on the composite compared to the pure terpolymer. Further increasing the amount of nanoparticles loading in the composite could be a work to improve the dielectric constant of the composite guided by the calculation theory for this type of composite system. The interdigitated electrode samples were successfully infiltrated with this terpolymer. The displacement measured was 0.01 C/m^2 at 70MV/m for this device. Polarization measurement could be carried out with sweeping electric fields up to 80 MV/m. Further improvement for this device could be focus on improving the filtration process with 100% polymer filled into the space between electrodes.